Opportunistic radar imaging using a multichannel receiver

Virginie Kubica

A thesis submitted for the degree of

Doctor of Philosophy

of

University College London

Radar Group

Department of Electronic and Electrical Engineering

University College London

2016

I, Virginie Kubica, confirm that the work presented in this thesis is my own. Where information has been derived from other sources, I confirm that this has been indicated in the thesis.

_____

_____

Abstract

Bistatic Synthetic Aperture Radars have a physically separated transmitter and receiver where one or both are moving. Besides the advantages of reduced procurement and maintenance costs, the receiving system can sense passively while remaining covert which offers obvious tactical advantages. In this work, spaceborne monostatic SARs are used as emitters of opportunity with a stationary ground-based receiver.

The imaging mode of SAR systems over land is usually a wide-swath mode such as ScanSAR or TOPSAR in which the antenna scans the area of interest in range to image a larger swath at the expense of degraded cross-range resolution compared to the conventional stripmap mode. In the bistatic geometry considered here, the signals from the sidelobes of the scanning beams illuminating the adjacent sub-swath are exploited to produce images with high cross-range resolution from data obtained from a SAR system operating in wide-swath mode. To achieve this, the SAR inverse problem is rigorously formulated and solved using a Maximum A Posteriori estimation method providing enhanced cross-range resolution compared to that obtained by classical burst-mode SAR processing. This dramatically increases the number of useful images that can be produced using emitters of opportunity. Signals from any radar satellite in the receiving band of the receiver can be used, thus further decreasing the revisit time of the area of interest. As a comparison, a compressive sensing-based method is critically analysed and proves more sensitive to off-grid targets and only suited to sparse scene. The novel SAR imaging method is demonstrated using simulated data and real measurements from C-band satellites such as RADARSAT-2 and ESA's satellites ERS-2, ENVISAT and Sentinel-1A.

In addition, this thesis analyses the main technological issues in bistatic SAR such as the azimuth-variant characteristic of bistatic data and the effect of imperfect synchronisation between the non-cooperative transmitter and the receiver.

Acknowledgements

First, I would like to express my gratitude to my supervisors, Professor Hugh Griffiths and Professor Xavier Neyt for their support and direction during all these years of hard work.

My thanks also go to the CISS Department's technical staff of the Royal Military Academy and the infrastructure section of the Military Hospital for their help in conducting the trials.

People from Radar group of University College London let me be part of their big family and therefore I thank all of you.

Thank you as well to my CISS Department's colleagues for their full cooperation.

Finally, I would like to thank my friends, my family and especially my twin-sister for their constant encouragement and support through this long and arduous journey. However, I give the deepest thanks to my husband, Jean-Edouard for his never-ending encouragement and understanding throughout the course of my research studies.

Publications

The following publications were produced as part of the work in this thesis:

- V. Kubica, X. Neyt, and H. D. Griffiths. Along-track resolution enhancement for bistatic SAR imaging in burst-mode operation. *IEEE Transactions on Aerospace and Electronic Systems*, accepted, 2016.

- V. Kubica, H. D. Griffiths, and X. Neyt. High cross-range resolution bistatic SAR imaging in wide-swath illumination modes. In *URSI 2015 Benelux Forum*, Enschede, NL, 2015.

- V. Kubica, X. Neyt, and H. D. Griffiths. Improved cross-range resolution in TOPSAR imaging using Sentinel-1A in bistatic operation. In *IEEE International Radar Conference*, Arlington, VA, 2015.

- V. Kubica, X. Neyt, and H. D. Griffiths. Opportunistic high cross-range resolution imaging using TOPSAR illuminations of Sentinel-1. In *URSI 2014 Benelux Forum*, Louvain-la-Neuve, BE, 2014.

- V. Kubica and X. Neyt. Feasibility of resolution-enhanced burst-mode interferometry in bistatic SAR. In *IEEE International Radar Conference*, Adelaide, South Australia, September 2013.

- K. Kulpa, P. Samczynski, M. Malanowski, L. Maslikowski, and V. Kubica. The use of CLEAN processing for passive SAR image creation. In *Proceedings of IEEE Radar Conference*, Ottawa, Ontario, Canada, May 2013.

- A. Tailliez, X. Neyt, and V. Kubica. Removal of direct path interference with CLEAN Algorithm in passive SAR imaging. In *URSI 2012 Benelux Forum*, page 43, Brussels, BE, September 2012.

- V. Kubica and X. Neyt. ScanSAR resolution enhancement in bistatic operation. In *IET International Radar Conference*, Glasgow, UK, October 2012.

- V. Kubica and X. Neyt. Cross-range resolution enhancement in burst-mode SAR in bistatic operation. In *URSI 2012 Benelux Forum*, page 32, Brussels, BE, September 2012.

- V. Kubica and X. Neyt. Passive SAR imaging using the ASAR instrument of ENVISAT as transmitter of opportunity. In *Proceedings of the 9th European Conference on Synthetic Aperture Radar*, pages 275–278, Nuremberg, Germany, April 2012.

- D. W. O'Hagan, A. Capria, D. Petri, V. Kubica, M. Greco, F. Berizzi, and A. G. Stove. Passive Bistatic Radar (PBR) for harbour protection applications. In *Proceedings of IEEE Radar Conference*, pages 446–450, Atlanta,GA, May 2012.

- E. Cristofani, V. Kubica, and X. Neyt. A multibeam opportunistic SAR system. In *IEEE SP Symposium on Information Theory and Signal Processing*, Brussels, BE, May 2011.

- V. Kubica, E. Cristofani, and X. Neyt. Strategies for mitigating the strong direct path signal in passive bistatic SAR imaging. In *IEEE SP Symposium on Information Theory and Signal Processing*, Brussels, BE, May 2011.

- E. Cristofani, V. Kubica, and X. Neyt. A multibeam opportunistic SAR system. In *Proceedings of IEEE Radar Conference*, Kansas City, MO, May 2011.

- V. Kubica, R. Hock, E. Cristofani, and X. Neyt. Strategies for the calibration of an array of patch antennas in passive bistatic SAR imaging. In *Proceedings of IEEE Radar Conference*, Kansas City, MO, May 2011.

- V. Kubica, X. Neyt, and C. Barbier. A first approach to opportunistic bistatic SAR using a phased-array. In *URSI 2010 Benelux Forum*, Brussels, BE, September 2010.

- M. Kubica, V. Kubica, X. Neyt, J. Raout, S. Roques, and M. Acheroy. Optimum target detection using illuminators of opportunity. In *Proceedings of IEEE Radar Conference*, pages 417–424, Verona, NY, April 2006.

Contents

List of Figures

List of Tables

Symbols

The quantities are specified with respect to an Earth-fixed reference frame when applicable.

$\widehat{}$(accent)	Estimated quantity
α	Chirp rate
A_{cell}	Clutter cell
A_{eff}	Effective area of the receive antenna
A_{phys}	Physical size of the antenna
β	Bistatic angle
$_{bi}$ (subscript)	A bistatic quantity
B	Bandwidth
B_a	Azimuthal bandwidth
B_f	Footprint bandwidth
B_n	Noise bandwidth of the receiver
c	Speed of light, $3\ 10^5$ km/s
$\mathbb{C}$	Set of complex numbers
$\mathbf{C_w}$	Cross-range compensation matrix
$\mathbf{c_w}$	Cross-range compensation function
d_{off}	Off-grid distance
$diag(\mathbf{w})$	A diagonal matrix with vector $\mathbf{w}$ on the diagonal
Δ	Complex correlation coefficient
Δy	Shift in the azimuth direction
δ	Sample coherence
$\delta\alpha$	Chirp rate error
δ_{az}	Azimuth resolution

δf	Centre frequency difference
Δf_{dop}	Shift in Doppler frequency
δ_{gr}	Ground range resolution
$\delta\phi$	Unknown phase difference
δ_r	Slant range resolution
$E[\cdot]$	Expectation operator
f	Instantaneous frequency
F	Noise factor of the receiver
F_w	Noise amplification factor
f_{dop}	Doppler frequency
f_R	Centre frequency of the receiver's local oscillator
f_T	Centre frequency of the transmitted signal
F_R	Pattern propagation factor for target-to-receiver path
F_T	Pattern propagation factor for transmitter-to-target path
γ	Proportionality constant in $\mathbf{g_{opt}}$
$\mathbf{g_{az}}$	Azimuth matched filter
$\mathbf{g_{opt}}$	Optimal filter
$\mathbf{g_{MF}}$	Matched filter
$G_{processing}$	Processing gain due to SAR processing
G_T	Transmit antenna gain
H	Height of the transmitter
h_R	Height of the receiver
$\mathbf{h^k}$	SAR phase history of the k^{th} patch
$\mathbf{h_w^k}$	Slow-time modulated SAR phase history of the k^{th} patch
$\mathbf{H}$	SAR phase history matrix
$\mathbf{H_r}$	SAR reconstruction matrix
$\mathbf{H_w}$	Slow-time modulated SAR phase history matrix
$\mathbf{I}$	Identity matrix
k_B	Boltzmann's constant, $1.38\ 10^{-23}$ Ws/K
K	Number of ground patches
k_r	Doppler rate
k_a	Doppler centroid rate

$\boldsymbol{\kappa}$	Amplitude of the azimuth matched filter
L	Number of pixels
λ	Wavelength
L_a	Physical antenna length
L_R	Transmit system losses
L_T	Receive system losses
m	Azimuth time instant $[0, M-1]$
M	Number of coherent pulses
μ	Mutual coherence
$\mathbf{n}$	Thermal noise
n	Range time instant $[0, N-1]$
N	Length of the received signal
N_L	Number of looks
N_S	Number of sub-swaths
N_R	Thermal noise power
ω	Signal angular frequency
φ	Phase history
ϕ	Phase along the pulse
ϕ_R	Initial phase of the receiver's local oscillator
ϕ_T	Initial phase of the transmitter's local oscillator
P_d	Power density on the Earth's surface
P_{direct}	Direct-signal received power
$P_{reflected}$	Reflected received power
P_R	Received power at the antenna port
P_T	Transmitted power
$\mathbf{q}$	Interference plus noise signal
$\mathbb{R}$	Set of real numbers
$_R$ (subscript)	A quantity belonging to the receiver
R	Slant-range distance
R_B	Distance transmitter-receiver
R_{bi}	Bistatic slant-range
$\mathbf{R_n}$	Covariance matrix of the noise

R_0	Closest approach slant range
$\mathbf{R_q}$	Interference plus noise covariance matrix
R_R	Distance to the receiver
$R_{R,max}$	Maximum detection range
R_T	Distance to the transmitter
$R_{T,0}$	Closest approach slant range to the transmitter
$\mathbf{R_x}$	Covariance matrix of the scene reflectivity
S	Sparsity of the scene
σ_n^2	Variance of the white noise
σ_x^2	Variance of the scene reflectivity
σ_B	Radar Cross Section of the point target
σ_0	Scattering coefficient
SNR_{point}^{raw}	SNR of a point target before SAR processing
SNR_{point}^{sar}	SNR of a point target after SAR processing
SNR_{dist}	SNR of distributed targets before and after SAR processing
$\mathbf{s_{dir}}$	Direct path signal
$\mathbf{s_e}$	Echo signal
$\mathbf{s_R}$	Received signal
$\mathbf{S_R}$	SAR echo matrix
$\mathbf{s_T}$	Transmitted signal
t	Fast time
$_T$ (subscript)	A quantity belonging to the transmitter
T_0	Effective noise temperature
T_B	Burst duration
T_D	Dwell time
T_F	Antenna footprint time
T_{int}	Coherent integration time
T_p	Pulse length
T_R	Scan repeat time
T_s	Sampling period
τ_{dir}	Propagation delay of the direct signal
τ_{echo}	Propagation delay of the echo signal

ϑ	Signal to Noise Ratio (SNR) of the echo signal
θ_B	Azimuth beamwidth
θ_{el}	Incidence angle of the transmitter / Off-nadir angle
θ_{li}	Local incidence angle
θ_R	Incidence angle of the receiver
θ_{sq}	Squint angle of the transmitter
u	Slow time
V	Velocity of the transmitter
$\mathbf{W}$	Slow-time modulation matrix
$\mathbf{w}$	Slow-time modulation vector
X	Across-track direction
x	Complex reflectivity of one patch
$\mathbf{x}$	Complex reflectivity vector
$\mathbf{x}^T$	Transpose of vector $\mathbf{x}$ (also for matrices)
$\mathbf{x}^*$	Complex conjugate of vector $\mathbf{x}$ (also for matrices)
$\mathbf{x}^\dagger$	Transposed conjugate of vector $\mathbf{x}$ (also for matrices)
$\|\mathbf{x}\|_0$	l_0-norm of vector $\mathbf{x}$
$\|\mathbf{x}\|_1$	l_1-norm of vector $\mathbf{x}$
$\|\mathbf{x}\|_2$	l_2-norm of vector $\mathbf{x}$
Y	Along-track direction
$\mathbf{y}$	Received signal in slow time
$\mathbf{y_c}$	Compensated received signal in slow time
Z	Height direction
z	One SAR image

List of Abbreviations

AAP	Azimuth Antenna Pattern
APES	Amplitude and Phase Estimation of a Sinusoid
AR	Auto-Regressive
ASAR	Advanced Synthetic Aperture Radar
BP	Back-Projection
BPDN	Basis Pursuit DeNoising
BSAR	Bistatic Synthetic Aperture Radar
COTS	Commercial off-the-shelf
CS	Compressive Sensing
DEM	Digital Elevation Model
DInSAR	Differential Interferometric SAR
DVB-T	Digital Video Broadcasting-Terrestrial
EAP	Elevation Antenna Pattern
ESA	European Space Agency
FFT	Fast Fourier Transform
FM	Frequency modulation

GAPES Gapped-Amplitude and Phase Estimation of a Sinusoid
GM Global Monitoring
GNSS Global Navigation Satellite System
GPS Global Positioning System

IF Intermediate Frequency
IIR Infinite Impulse Response
InSAR Interferometric SAR
IRF Impulse Response Function
IW Interferometric Wide Swath

LBF Loffeld Bistatic Formula
LFM Linear Frequency-Modulated
LNA Low Noise Amplifiers
LP Linear Programming

MAP Maximum *a Posteriori*
MF Matched Filter
MMSE Minimum Mean Square Error
MP Matching Pursuit
MSE Mean Square Error
MTI Moving Target Indicator

OMP Orthogonal Matching Pursuit

PBR Passive Bistatic Radar
PDF Probability Density Function
PG Papoulis-Gerchberg
PRF Pulse Repetition Frequency

PSD Power Spectral Density

PSLR Peak-to-Side Lobe Ratio

QPE Quadratic Phase Error

RADAR RAdio Detection And Ranging

RAM Radar Absorbing Material

RAR Real Aperture Radar

RCM Range Cell Migration

RCS Radar Cross Section

RF Radio Frequency

RIP Restricted Isometry Property

RMA Royal Military Academy

RMS Root Mean Square

SAR Synthetic Aperture Radar

SGP4 Simplified General Perturbations version 4

SGPL1 Spectral Projected-Gradient L1

SIR Shuttle Imaging Radar

SLC Single-Look Complex

SNR Signal-to-Noise Ratio

SWB ScanSAR Wide B

TanDEM-X TerraSAR-X add-on for Digital Elevation Measurement

TCXO Temperature Compensated Crystal Oscillator

TI Translational-Invariant

TLE Two-Line Keplerian Element

TOPSAR Terrain Observation by Progressive Scan SAR

TV Translational-Variant

ULA Uniform Linear Array

UTC Coordinated Universal Time

WiFi Wireless Fidelity

WS Wide Swath

Chapter 1

Introduction

1.1 Overview

RAdio Detection And Ranging (RADAR) was used already before World War II in military applications such as detection and tracking of moving target, and has since then played an important role in remote sensing applications. In contrast to optical sensors, a radar imaging system is an active remote sensing system as it provides its own source of energy to produce an image. Radar does not require sunlight like optical systems and can thus acquire data either by day or by night. In addition, due to the specific wavelength of the transmitted signal, cloud cover can be penetrated and radar imaging is thus also an all-weather instrument [1]. The resolution in the azimuth direction of both optical and Real Aperture Radar (RAR) systems is limited by the physical dimension of the antenna aperture. A narrow beamwidth yielding a good azimuth resolution requires an impractical large antenna. Synthetic Aperture Radar (SAR) avoids this requirement by collecting radar returns of a target from different positions. By processing the return signals, very high resolution in azimuth can be achieved. It was in the early 1950s that the SAR processing technique to improve the azimuth resolution of RAR was presented: the concept consists of synthesising a long antenna by virtue of the relative motion of the platform and the illuminated scene, hence the name synthetic aperture. The important difference between RAR and SAR is that SAR is a coherent system that requires the phase of the transmitted pulses to be preserved which really became practical with the advent of frequency-stable microwave signal sources such as klystron in the late 1930s.

The first operational SAR appeared in the mid 1950s and the first Earth-viewing

spaceborne SAR was launched into orbit on the Seasat spacecraft in 1978 [2]. It took thirteen years before the second spaceborne SAR was put into orbit which was a European Space Agency (ESA) satellite, ERS-1. During all those years, research work on SAR continued with airborne SARs and Shuttle Imaging Radar (SIR) series. Through the years, the used optical SAR processors have given way to real-time digital SAR processors which improved image quality, algorithm efficiency and support different data collection mode [2].

Phased-array microwave technology was also a key component in the development of new SAR modes which allows a larger size of the illuminated area such as in the ScanSAR mode or a better azimuth resolution such as in the spotlight mode. Nowadays an azimuth resolution of the order of centimetres can be achieved by SAR systems [3].

One of the big challenge in radar imaging is interpreting and extracting information from the received signals. This is the area where most of the current effort is taking place and new areas of application are constantly emerging in both military and civilian areas. Military SAR applications [4] include battlefield reconnaissance or target recognition and classification. Civilian applications [5] include topographic mapping, geology, oil spill monitoring, sea ice monitoring, oceanography, agricultural classification and assessment, land use monitoring or terrain motion measurement for disaster prevention.

Bistatic radars are radars in which the transmitter and the receiver are at separate locations. They have a longer history than SAR systems as the first demonstration of bistatic radar occurred in the early 1920s [6] when a physical separation between the antennas was one of the solutions to isolate the sensitive receiver from the high power continuous wave transmitter. Bistatic radars can operate with cooperative transmitters which are under control of the user, or non-cooperative transmitters. In the latter case, the radar is passive as it does not transmit any signals on its own and is called Passive Bistatic Radar (PBR). Hence, PBRs are basically passive receiver systems [6, Chapter 1]. The transmitting platform may be ground-based such as a Frequency modulation (FM) radio transmitter [7], a cellphone base station [8], a Digital Video Broadcasting-Terrestrial (DVB-T) transmitter [9], a television transmitter [10] or space-based such as the communication satellite Iridium [11], a Global Navigation Satellite System (GNSS) [12] or a broadcast geostationary satellite [13]. The separation between the transmitter

and the receiver offers very flexible geometries thanks to which the detection of targets that may be stealthy for conventional monostatic radars is now possible. Besides, in a hostile environment, a PBR can remain covert while sensing passively. This flexible geometry also allows to exploit the forward-scatter region where the Radar Cross Section (RCS) of any targets near the baseline joining transmitter and receiver may be substantially increased. This is described by Babinet's principle [1, Chapter 25].

In addition to enjoying the same benefits as bistatic radar, Bistatic Synthetic Aperture Radar (BSAR), where the transmitter or the receiver or both are moving, allows to investigate different scattering mechanisms from monostatic SAR and can then complement monostatic images [14, 15]. BSAR has already been conducted in air-air [16, 17], air-space [18, 19], space-space [20, 21], air-ground [22] or space-ground [23–26] configurations. An example of permanently operational space-space BSAR system is the TerraSAR-X add-on for Digital Elevation Measurement (TanDEM-X) mission: TerraSAR-X, a X-band monostatic radar, is augmented by a second similar system in close orbit for high resolution Digital Elevation Model (DEM) generation [27]. BSAR can also use transmitters designed for other purpose such as GNSS satellite [28] or television broadcasting satellite [29]. In this work, monostatic radars have been chosen as illuminators of opportunity for their high power density at the Earth's surface, and the transmission of a purpose designed radar waveform.

The revisit time, i.e. the time interval between SAR images over the same area, is a paramount parameter in satellite remote sensing. Several techniques have been used to decrease the time interval between SAR images such as changing the radar modes, e.g. using a wide-swath mode, a dual-sided imaging which is adopted by RADARSAT-2, or launching a constellation of several SAR satellites such as the constellation of Cosmo-SkyMed [30] and of SAR-Lupe. Deploying a ground-based stationary receiver [23–26, 31], similar to the bistatic system described in this thesis, appears to be the cost-efficient solution for decreasing the revisit time on the area of interest since signals from any SAR satellite in the receiving band of the receiver can be used to produce an image of the area of interest.

Another driving factor in satellite remote sensing is obtaining high cross-range resolution SAR images which is at the expense of a wide illuminated swath due to ambiguity constraint [32–34]. During this work, it has been noted through the multiple

measurement campaigns led at the Royal Military Academy (RMA) in Brussels that spaceborne SARs usually operate in wide-swath mode which gives priority to a wide-swath coverage over a high cross-range resolution. The exploitation of those burst-mode illuminations in a bistatic configuration is then valuable in terms of revisit time.

In this thesis, we studied the possibility to produce high cross-range resolution images in the case of a wide-swath SAR mode illumination using a ground-based bistatic receiver. This configuration offers several important advantages.

- It allows to reduce the revisit time on the area of interest.
- This bistatic configuration has a reduced latency. The SAR image obtained from the bistatic receiver may be indeed distributed more rapidly to the user than would be the case of the image obtained on-board the monostatic radar.
- It makes the image production system independent of any operators provided the illuminator of opportunity transmits.
- It has reduced procurement and maintenance costs.

The research community in BSAR imaging mostly limit their analysis to the conventional stripmap mode [16, 17, 23–26]. Examining burst-mode illumination in a bistatic configuration for high-resolution imaging purposes appears to be the first study of its kind. Applications of such a system include imaging, interferometry using multiple channels for small-scale area monitoring, like buildings, small urban area or single hillsides (avalanche or landslide prediction), or DEM generation.

1.2 Original contributions

The main original contributions of this thesis are listed below.

- The synchronisation of the receiver with the non-cooperative transmitter is critically analysed. The resulting phase errors are assessed and their impact on SAR imaging evaluated.
- A rigorous SAR focussing formulation based on a Maximum *a Posteriori* (MAP) estimation is provided. This formulation is applicable for any sort of radar geometries (monostatic, bistatic). Then, a justification is provided for the Matched Filter (MF) based SAR focussing usually performed.

- A burst-mode resolution enhancement method is derived to perform SAR focussing in wide-swath modes illumination. The performance of this method are demonstrated using simulated data and real measurements and are shown to be better than classical burst-mode SAR processing.

- A comparison is drawn between the burst-mode resolution enhancement method and a Compressive Sensing (CS)-based method which proves more sensitive to off-grid targets and only suited to sparse scene.

1.3 Thesis outline

The thesis is split into eight chapters. The chapter following this introduction gives an overview of the background theory used in this work including basic SAR theory and its extension to bistatic SAR. Chapter 3 provides the research context relevant to this work which covers the main technological issues in bistatic SAR such as the synchronisation with the transmitter, the azimuth-variant SAR focussing or the direct-signal interference. In Chapter 4, the synchronisation issue between the non-cooperative transmitter and the bistatic receiver is critically analysed. Chapter 5 is dedicated to the novel concept of exploiting the signal transmitted in the elevation sidelobes to increase the cross-range resolution. In Chapter 6, we introduce the signal model in the framework of SAR imaging and develop the novel burst-mode resolution enhancement method used for the generation of the bistatic SAR images. The analysis of the performance and the limitations of the burst-mode resolution enhancement method in different burst-mode illumination such as ScanSAR and TOPSAR is provided. A CS-based method for a comparison of performance is also critically analysed. In Chapter 7, imaging results are shown to confirm the success of the novel SAR imaging algorithm in the case of a burst-mode illumination. Finally, Chapter 8 presents conclusions drawn from the entire research project and future directions and possible improvements of the work are discussed.

Chapter 2

Background theory

2.1 SAR theory

2.1.1 Principle

A Synthetic Aperture Radar (SAR) is an imaging radar mounted on a moving platform that uses signal processing to improve the cross-range resolution beyond the limitation of the physical antenna aperture. SAR is thus a combination of radar and signal processing. In the same way as a conventional radar, electromagnetic waves are sequentially transmitted, the targets in the footprint of the antenna reflect the energy back and the echoes are collected by the receiver. As a result of the pulsed transmission and platform motion, the scene is scanned in two dimensions. Conceptually, data collection proceeds as follows: in each radar position, the radar "stops", transmits a pulse, records the echoes from the imaging area, and then advances to the next position. This is commonly known as the 'stop-and-go' assumption [35, Chapter 4]. In other words, the sensor and the scattering object are assumed to be stationary during the time interval during which the pulse washes over the target.

A coherent combination of the received signals allows the construction of a virtual aperture that is much longer than the physical antenna length, L_a. The SAR image results from processing the raw data and represents a measure of the scene reflectivity.

2.1.2 Geometry

The general geometry of a spaceborne SAR operating in stripmap mode is presented in Fig. 2.1. The X-axis is referred to as the across-track or ground range direction. The Y-axis is referred to as the along-track or azimuth direction and is taken parallel to the

motion of the radar. The XY-plane is locally tangent to the Earth's surface. The Z-axis is chosen perpendicular to the XY-plane and is referred to as the height direction. The transmitter is usually assumed to move along a straight path with a constant velocity, V, which is approximately true for a short observation time. The distance between the sensor position and the point target is defined as the slant range, R, with a minimum value at closest approach defined as R_0. The inclination of the antenna with respect to the nadir is called the off-nadir angle, θ_{el}, which is denoted as the elevation angle.

The SAR instrument moves along its trajectory and sends out pulses at a rate defined by the Pulse Repetition Frequency (PRF). As a result of the pulsed transmission and platform motion, the scene is scanned in two dimensions and the phase and amplitude of the received echoes are recorded in two dimensions. The first one is defined as the fast-time (or range-time) dimension, denoted by t; it is associated with propagation delays between signal transmission and echo reception. The second is defined as the slow-time (or azimuth-time) dimension, denoted by u; this is used to specify the radar's position during array synthesis.

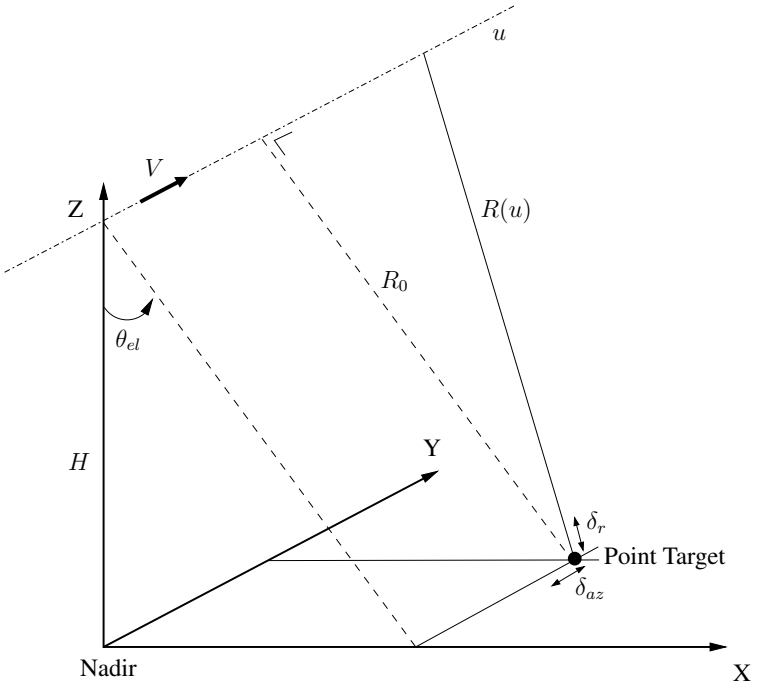

Figure 2.1: Geometry of a monostatic SAR.

Figure 2.2 (a) shows the propagation of a pulse of duration T_p. Also shown is the Elevation Antenna Pattern (EAP) of the transmit antenna. The minimum and maximum range lie within the mainlobe of the elevation beam and delimit the swath-width. It is

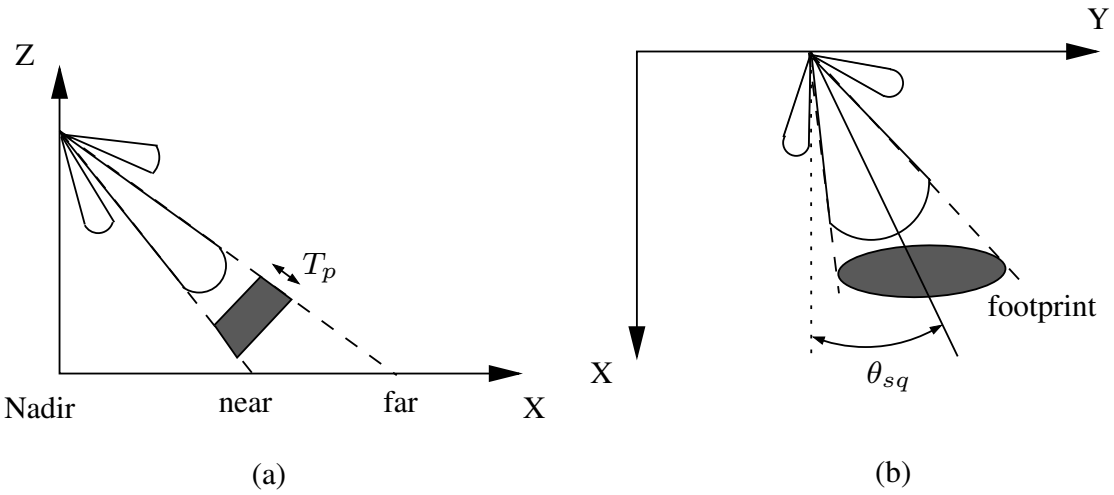

Figure 2.2: (a) Cross-section perpendicular to the flight path (XZ plane) and (b) cross-section parallel to the Earth (XY plane).

interesting to note that pulsed radar systems suffer range ambiguities, that is, echoes from pulses transmitted at different times arrive at the receiver simultaneously. In that case, the range information contained in the echo delay cannot be directly related to a single transmitted pulse and becomes ambiguous. This effect is relevant to spaceborne SAR due to the large swath. This can be controlled by the selection of the PRF. Hence, a constraint on the PRF and a shaping of the EAP can avoid these range ambiguities.

Figure 2.2 (b) shows the illuminated area by the antenna diagram in azimuth. The extent of the drawn footprint corresponds to the 3 dB beamwidth of the antenna diagram. The squint angle θ_{sq} is defined as the angle between the slant range direction and the look direction of the antenna beam.

2.1.3 The Two-Dimensional signal

For subsequent processing of the data, the received signal is organised as a two-dimensional data array (range and azimuth) as the SAR data collection scenario implies. The received signal from a given transmitted pulse represents one row of the SAR echo matrix, $\mathbf{S_R}(n, m)$. Then, as the sensor moves along its trajectory, more pulses are transmitted, and the associated echoes are written into successive rows. The vertical dimension is then the azimuth time instant, m, and the horizontal dimension the range time instant, n as illustrated in Fig 2.3. The shaded region represents the duration of the transmitted pulse.

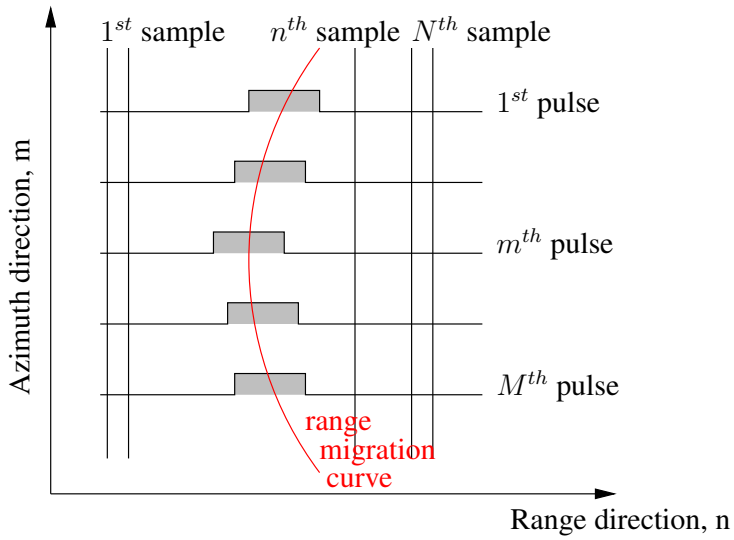

Figure 2.3: Representation of the SAR data in 2D and illustration of the range cell migration issue.

2.1.4 Range dimension

2.1.4.1 Linear Frequency-Modulated signal

The performance in the range dimension are measured by the ability to distinguish two objects separated by some minimum distance which depends on the transmitted pulse. If a square unmodulated pulse is transmitted, the slant-range resolution is obviously equal to

$$\delta_r = \frac{cT_p}{2} \tag{2.1}$$

with c and T_p respectively the speed of light and the pulse length of the transmitted signal. Therefore, to obtain a fine resolution, a short pulse must be transmitted. However, the Signal-to-Noise Ratio (SNR) of the received signal must be high to maximise the probability of target detection. The SNR can be improved by increasing the average transmitted power by either raising the peak power (risking an arcing event in the waveguides of the transmitter) or transmitting a longer pulse and then compressing it to the desired resolution. This is called pulse compression [35, Chapter 3] and is described in the following section. A Linear Frequency-Modulated (LFM) pulsed waveform is commonly utilised for transmission both in RAR and SAR. The transmitted signal in baseband can be written as

$$s_T(t) = \begin{cases} e^{j\pi\alpha t^2} & \frac{-T_p}{2} \leq t \leq \frac{T_p}{2} \\ 0 & otherwise \end{cases} \tag{2.2}$$

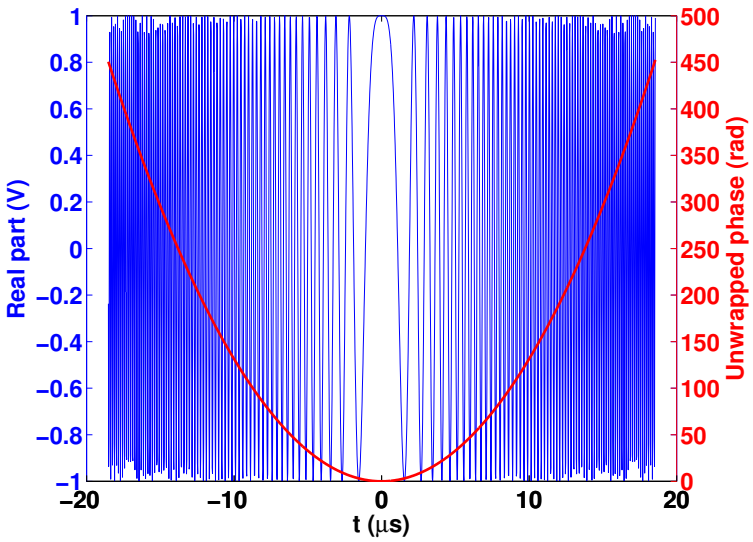

Figure 2.4: Real part of a LFM signal (with ERS-2 parameters) and its phase as a function of the fast-time.

with α being the chirp rate in Hz/s. The instantaneous frequency $f(t)$ is the derivative of the phase with respect to time and is given by

$$f(t) = \frac{1}{2\pi}\frac{d\phi(t)}{dt} = \alpha t \tag{2.3}$$

It varies in a linear manner over time t yielding the bandwidth

$$B = \alpha T_p \tag{2.4}$$

Figure 2.4 shows a baseband transmitted pulse and its quadratic phase evolution.

2.1.4.2 Pulse compression

Let us consider $\mathbf{s_T}$, the transmitted waveform of a radar. The return from a point target is a time delayed and attenuated version of the transmitted signal, and is sampled at the receiver with T_s the sampling period. The sampled echo signal is given by

$$\mathbf{s_e} = [s_e(0), s_e(1), ..., s_e(n), ..., s_e(N-1)]^T \tag{2.5}$$

with $s_e(n) = s_T(nT_s - \tau_{echo})e^{j\omega\tau_{echo}}$, N being the length of the received signal, τ_{echo} the round-trip time to the target and ω the pulsation of the signal. The exponential factor represents the propagation phase of the echo signal.

The received signal can be modelled by

$$\mathbf{s_R} = x\mathbf{s_e} + \mathbf{q} \tag{2.6}$$

with $\mathbf{s_R} = [s_R(0), s_R(1), ..., s_R(n), ..., s_R(N-1)]^T$ and with x the unknown complex reflectivity of the target return. $\mathbf{q}$ is the interference plus noise signal that consists of thermal noise in the receiver front end and of interferences such as reflections of other scatterers.

Assuming the noise is Gaussian, the problem of extracting x optimally out of the background noise $\mathbf{q}$ is solved by applying the well-known optimal filter [36, Chapter 6]

$$\mathbf{g_{opt}} = \gamma {\mathbf{R_q}}^{-1} \mathbf{s_e} \tag{2.7}$$

to the received signal vector, $\mathbf{s_R}$.

$\mathbf{R_q} = E\left[\mathbf{q}\mathbf{q}^\dagger\right]$ is the interference plus noise covariance matrix where $E[.]$ denotes expectation and † means complex conjugate transpose. $\mathbf{g_{opt}}$ maximises the likelihood of x [37, Chapter 1] if the proportionality constant γ is

$$\gamma = (\mathbf{s_e}^\dagger {\mathbf{R_q}}^{-1} \mathbf{s_e})^{-1} \tag{2.8}$$

This optimal filter can only be computed if the covariance matrix $\mathbf{R_q}$ is known and invertible.

If only white Gaussian noise is present, the covariance matrix can be written as

$$\mathbf{R_q} = \sigma_n^2 \mathbf{I} \tag{2.9}$$

with σ_n^2 the variance of the white noise and $\mathbf{I}$ the identity matrix. The optimal filter (2.7) becomes

$$\mathbf{g_{MF}} = \frac{\mathbf{s_e}}{\mathbf{s_e}^\dagger \mathbf{s_e}} \tag{2.10}$$

which is the Matched Filter (MF). The output of the optimal filter is, then, a scalar given by the following inner product

$$\widehat{x} = {\mathbf{g_{MF}}}^\dagger \mathbf{s_R} \tag{2.11}$$

It is important to note that the estimation of the reflectivity (2.11) using the matched filter is optimum for one target in the presence of white noise or for several targets in different resolution cells. In the presence of colored noise, i.e. if interferences or other targets are present, the covariance matrix must be computed or estimated [37, 38].

The time invariance of the matched filter (2.11) offers the important advantage to permit an implementation using a convolution that can be implemented using the Fast Fourier Transform (FFT).

2.1.4.3 Range resolution

To study the range resolution, one must look at the ambiguity function [39, Chapter 10] of the matched filter. Here, the matched filter is a LFM pulse whose ambiguity function at zero-Doppler (in the time direction) is a sinc $(\sin(x)/x)$ function as illustrated in Fig. 2.5. Note that the ambiguity function in the fast-time direction is a sinc function

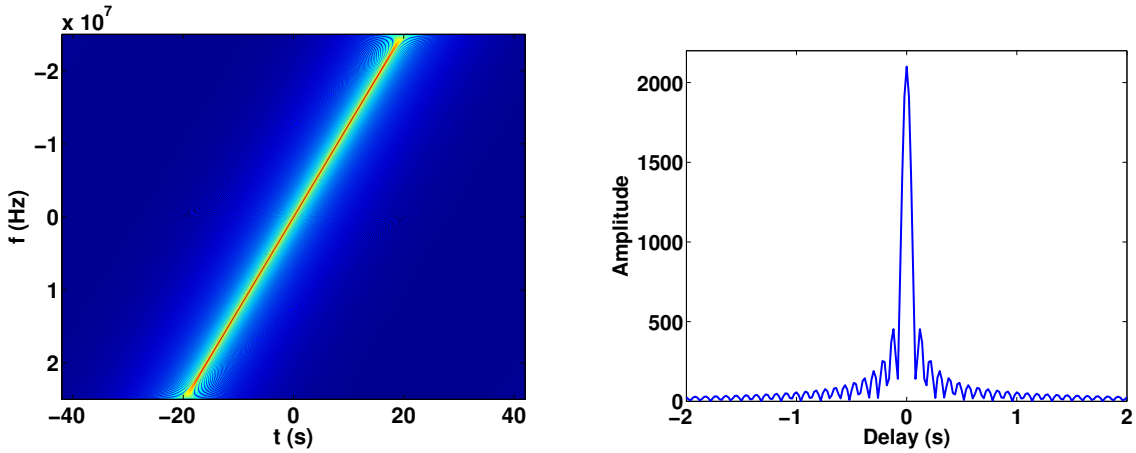

(a) Auto-ambiguity function (b) Ambiguity function at zero-Doppler

Figure 2.5: Ambiguity function of a theoretical RADARSAT-2 pulse.

only if the amplitude of the MF is rectangular which is not the case in reality due to e.g. propagation effect in the range dimension. The slant range resolution is governed by the mainlobe width of the section of the ambiguity function at zero-Doppler and is given [3, Chapter 1] by

$$\delta_r = \frac{c}{2B}. \tag{2.12}$$

This parameter is only limited by the bandwidth of the transmitted waveform, B. The ground range resolution is simply the projection of δ_r on the ground and is written as

$$\delta_{gr} = \frac{c}{2B\sin(\theta_{li})} \tag{2.13}$$

with θ_{li} the local incidence angle which is the angle between the radar beam and the normal to the Earth's surface at the particular point of interest. For the sake of simplicity, we assume here that the Earth is locally flat, and hence, that the incidence angle is equal to the off-nadir angle, θ_{el} as defined in Fig. 2.1.

2.1.5 Azimuth dimension

2.1.5.1 SAR processing

Pulse compression in the range dimension is performed on a pulse to pulse basis and is used in both RAR and SAR. The essence of the SAR technology appears in the azimuth direction: it will combine the target's energy spread in range in the azimuth direction yielding a SAR image.

The most important relationship in SAR processing is the slant range as a function of slow-time of a point target with respect to the sensor. Indeed, it determines the SAR inherent effects such as the modulation of the signal in azimuth direction and the range cell migration [35, Chapter 5]. As the radar beam passes over the point target, as in Fig. 2.1, the slant range to the target varies with azimuth time, u. Using the Pythagorean theorem, the instantaneous slant range can be calculated as

$$R(u) = \sqrt{R_0^2 + V^2 u^2} \tag{2.14}$$

with R_0 being the range of closest approach from the illuminator to the target, the corresponding time being defined as the azimuth time origin. In this work, the antenna beam is assumed to look broadside, i.e. the squint angle is zero, and thus, the Doppler centroid is equal to zero. Presupposing a linear flight path of the transmitter, the range history (2.14) is hyperbolic when plotted against azimuth time as illustrated in Fig 2.3. This hyperbola is known as the range migration curve. Figure 2.6 shows that targets at a given slant range of closest approach, R_0, have the same range history hyperbola, independently of their azimuth position. Note that the shape of the hyperbola changes as a function of R_0: targets at longer ranges are characterised by a hyperbola whose curvature is smaller.

One can expand (2.14) into a Taylor series around the point $u = 0$ (the slant range of closest approach to the target). Keeping the first two terms, (2.14) becomes

$$R(u) \approx R_0 + \frac{V^2 u^2}{2R_0} \tag{2.15}$$

This approximation can only hold if $R_0 \gg Vu$, i.e. if the exposure time is moderate. This is more commonly known as the parabolic approximation [35, Chapter 5]. This slant range variation in slow time causes a phase modulation from pulse to pulse, called

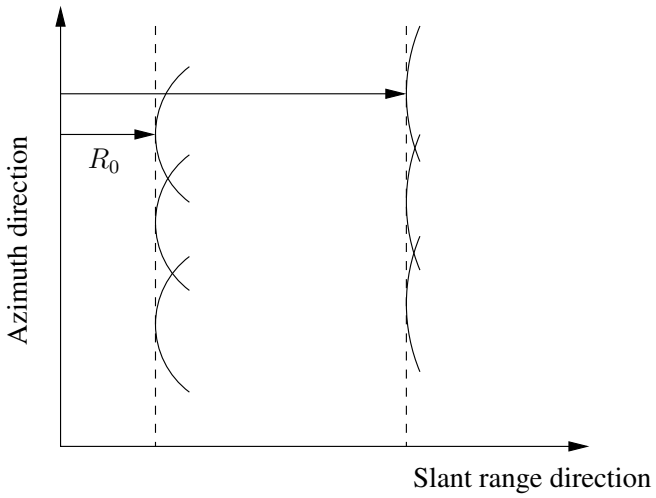

Figure 2.6: Azimuth-slant range plane: Targets having the same slant range of closest approach share the same range history curvature.

the phase history which is given by

$$\varphi(u) = \frac{2\pi}{\lambda} R(u) \approx \frac{2\pi}{\lambda} \left[R_0 + \frac{V^2 u^2}{2R_0} \right] \tag{2.16}$$

where λ is the wavelength[1]. According to the parabolic approximation, the phase history has a quadratic form, implying a LFM signal in the azimuth direction with a bandwidth called Doppler bandwidth. Hence, as in the range direction, a high resolution in azimuth can be obtained by matched filtering over slow time yielding also a sinc function in the azimuth direction. This is called azimuth compression. To estimate the reflectivity at each pixel, the azimuth MF will coherently sum the range-compressed data along the azimuth locus which is the range as a function of the azimuth position of the transmitter of the image pixel. The discrete azimuth MF is given by

$$g_{az}(m) = \kappa(m) e^{-j\varphi(m)} \tag{2.17}$$

with $m \in [0, 1, ..., M-1]$ the number of the transmitted pulse and M the total number of coherent pulses. It is assumed that the geometry, i.e. the range to the target, is accurately known.

The factor $\kappa(m)$ reflects that the amplitude of the theoretical azimuth MF is not rectangular but depends on the combined azimuth antenna diagram of the transmit and

[1]As the bandwidth is small compared to the frequency (this is the case for the satellite systems considered), the system is considered monochromatic.

receive antenna, the gain of the receiving chain and the coherent gain of the pulse compression in fast-time. This factor affects the ambiguity function in terms of resolution and SNR: the width of the mainlobe of the ambiguity function of a windowed pulse is larger [39, Chapter 10] than that of a rectangular pulse.

Following (2.16), this azimuth MF varies for each range of the image. As the phase history does not depend on the azimuth of the target, this configuration is translational invariant in azimuth and can also be implemented via a FFT after correcting the range migration effect [35].

2.1.5.2 Azimuth resolution

As the azimuth MF is also a LFM signal, the section of the ambiguity function at zero-Doppler is a sinc function as well, the width of which governs the azimuth resolution, δ_{az}. It can be shown [35, Chapter 4] that the maximum azimuth resolution depends on the time during which the scatterer is illuminated by the radar beam, called the SAR integration time. In practice, this SAR integration time is reduced to the time during which the phase of the scatterer is well estimated, i.e. the time during which the scatterer remains coherent.

2.1.5.3 Image formation algorithm

The matched filter based SAR processing to estimate the reflectivity, $\hat{x}$, of the considered patch can be divided into two distinct phases. First, matched filtering in range is performed on each row of the SAR data echo matrix, $\mathbf{S_R}(n, m)$. Then, the reflectivity of the patch is estimated by applying the azimuth matched filter which is 'matched' to the expected phase history of the considered patch. The result is a two-dimensional sinc function centred at the point target position in the SAR image, the mainlobe width of which has the size $\delta_r \times \delta_{az}$.

2.1.6 Radar imaging modes

Monostatic SAR systems can operate in several imaging modes, the most important of which are stripmap mode and wide-swath modes such as ScanSAR and Terrain Observation by Progressive Scan SAR (TOPSAR) mode as depicted in Fig. 2.7. The signals presented in this section are real measurements acquired from the stationary ground-based receiving system developed in this thesis.

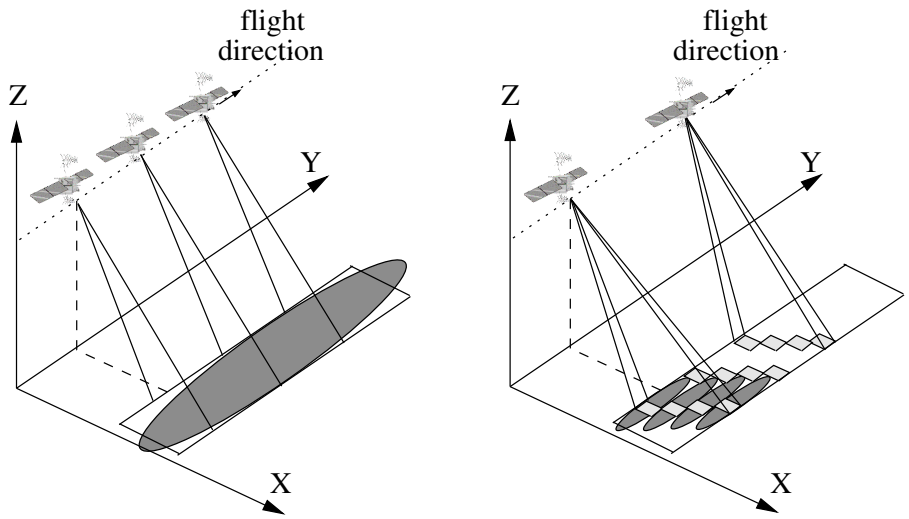

Figure 2.7: Radar imaging modes: (a) Stripmap mode and (b) wide-swath modes such as ScanSAR and TOPSAR mode.

2.1.6.1 Stripmap mode

The classical mode of operation is the stripmap mode in which the transmitting beam continuously illuminates the scene with an antenna beam fixed relative to the moving platform, i.e. at a fixed elevation angle thereby illuminating a strip of terrain as illustrated in Fig. 2.7 (a). This imaging mode leads to a high cross-range resolution but is constrained to a narrow swath due to range ambiguity limitations [40]. The dwell time for all processed ground patches is related to the beamwidth of the antenna. The stripmap mode is the more basic radar mode and is implemented on all radar satellites. However, its limited swath means a low revisit frequency over a specific area which is the reason why this mode is not operated very often on SAR satellites.

Figure 2.8 depicts the Intermediate Frequency (IF) signal of the Advanced Synthetic Aperture Radar (ASAR) instrument of ENVISAT from ESA, operating in stripmap mode, recorded as the satellite illuminates the receiver. The amplitude modulation of the signal corresponds to the Azimuth Antenna Pattern (AAP) of the transmitter as the AAP of the receiver is wider than that of the transmitter. As depicted in Fig. 2.8, the mainlobe illumination time of the ASAR beam is approximately equal to 0.9 s. Note the asymmetry of the signal resulting likely from a saturation of the Radio Frequency (RF) amplifiers.

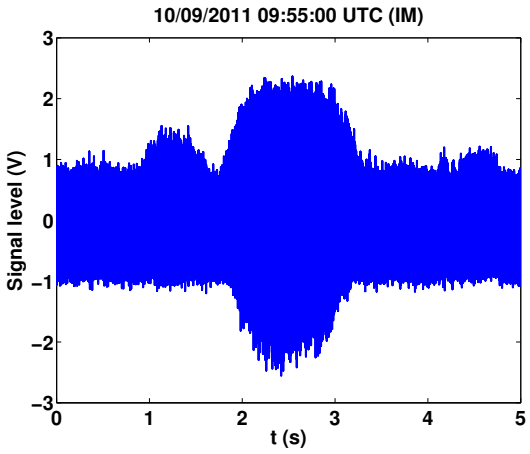

Figure 2.8: Acquired signal in stripmap mode from the ASAR instrument of ENVISAT.

2.1.6.2 ScanSAR mode

To overcome the ambiguity constraint yielding a limited illuminated swath in the stripmap mode, [33] proposed the ScanSAR mode [32, 41, 42] which offers synoptic observations of large-scale phenomena and a higher revisit frequency. In ScanSAR mode, the synthetic aperture is divided in N_S sub-swaths. As an example, Fig. 2.9 represents a four sub-swath scanning cycle. Each sub-swath is illuminated by the antenna beam for a short time interval, called burst duration, T_B, which is very small compared to T_F, the antenna-footprint time. Then, the antenna beam is steered in the range direction to another sub-swath. The scanning cycle continues till the full swath is covered. T_R is the scan repeat time which is the time for the beam to come back to the same range sub-swath. The ScanSAR mode allows imaging of a swath much wider than the stripmap mode but at the cost of a degraded cross-range resolution. The ScanSAR mode is implemented on most of the radar satellites such as ENVISAT, RADARSAT-2 or even Sentinel-1A.

To have a better understanding of the burst-mode illumination of a ScanSAR operating satellite, the evolution of the Doppler frequency as a function of the slow time for a four sub-swath ScanSAR mode such as the ScanSAR Wide B (SWB) mode of RADARSAT-2 is depicted in Fig. 2.10. In Fig. 2.9, three patches, A, B and C, having the same slant range of closest approach to the transmitter but located at different azimuths are represented. In Fig. 2.10, the Doppler histories of the targets are represented by dashed lines with the same negative slopes, equal to the Doppler rate k_r. In

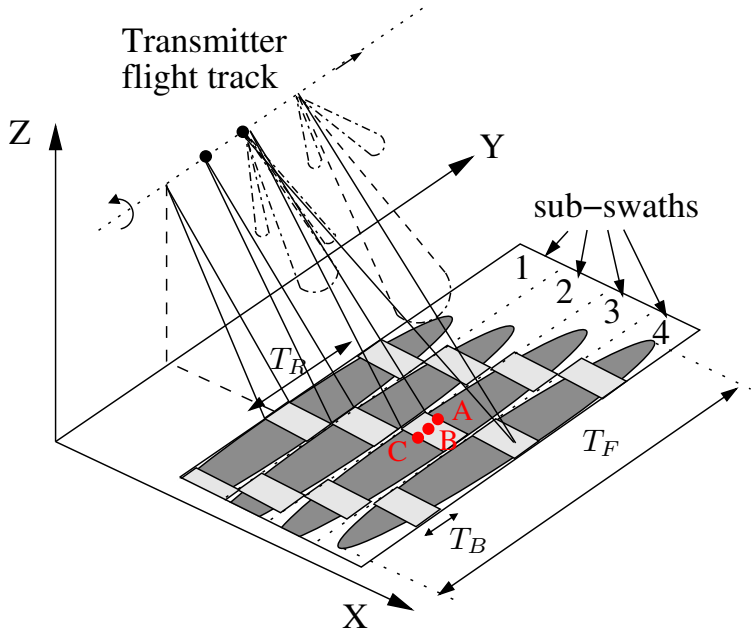

Figure 2.9: Acquisition geometry in ScanSAR imaging mode in the case of four sub-swaths.

ScanSAR and in the monostatic geometry, the dwell time, T_D, i.e. the azimuth integration time for a point target, is identical to the burst duration, T_B. The mainlobe of the AAP, represented on the left in Fig. 2.10, is fixed in azimuth.

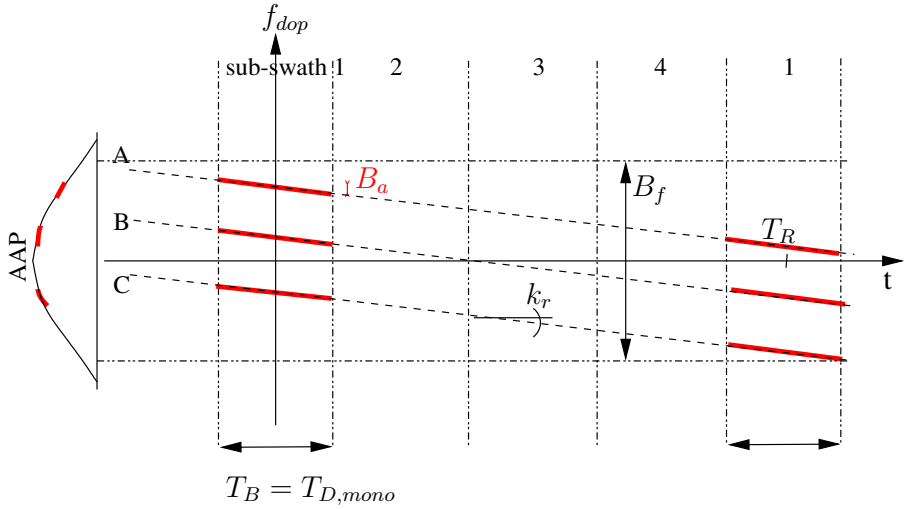

Figure 2.10: ScanSAR mode: Time-frequency diagram of three scatterers in the monostatic geometry where B_f is the footprint bandwidth and $B_a = T_B k_r$ is the bandwidth for each target. The thick red lines represent the focussed phase history.

The signals in Fig. 2.11 result from the ASAR ScanSAR mode transmissions of

the ENVISAT satellite: (a) and (b) the Wide Swath (WS) mode and (c) and (d) the Global Monitoring (GM) mode. For acquisitions (a) and (c), the geometry was such that the receiver only received the pulses coming from the mainlobe of the scanning beam yielding a non-continuous illumination. The number of looks, N_L, of the ASAR instrument of ENVISAT in WS mode that can be processed to reduce the speckle inherent to SAR images [43] can be guessed from Fig. 2.11 (a) and is equal to 3. Note that the bursts are shorter in the GM mode than in the WS mode which yields a coarser cross-range resolution as indicated in [44].

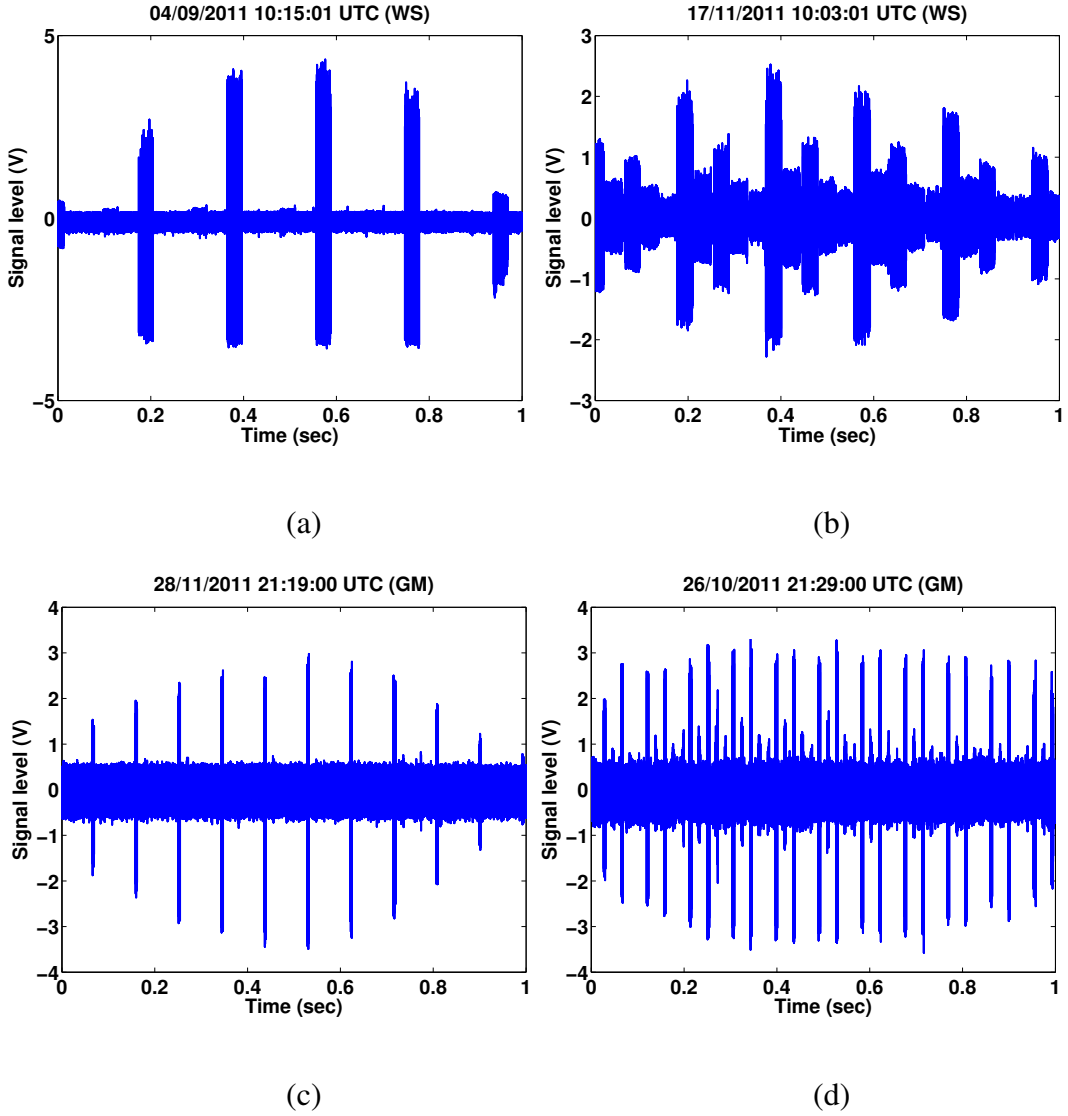

Figure 2.11: Acquired ENVISAT SAR signals: (a) and (b) in WS, (c) and (d) in GM modes.

It is possible, for a receiver at some specific location, to receive signals coming

from the elevation sidelobes of the scanning beams illuminating the adjacent sub-swath. In this case, the illumination becomes continuous: the SNR of the sidelobes emission of the transmit antenna is sufficient as depicted in Fig. 2.11 (b) and (d). This is explained in detail in Chapter 5.

Figure 2.12 represents 3 cycles of a ScanSAR illumination of RADARSAT-2 operating in SWB with a burst duration of 0.05 s. This ScanSAR mode has four elevation beams instead of five as for ENVISAT. The dashed lines demarcate each group of 4 beams. Note the longer illumination time per sub-swath of RADARSAT-2 compared to ENVISAT yielding a better cross-range resolution than that of ENVISAT WS mode.

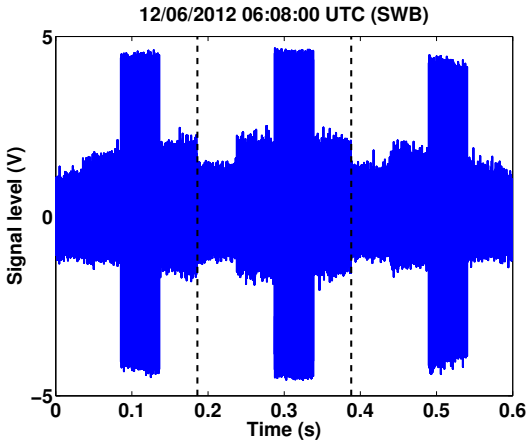

Figure 2.12: Acquired ScanSAR signal in a multi-beam illumination in SWB mode of RADARSAT-2.

2.1.6.3 TOPSAR mode

In ScanSAR mode, the targets are illuminated by different portions of the AAP as depicted in Fig. 2.10. This results in different amplitude weighting of the phase history of the different targets. A scalloping effect, a well-known regular azimuth modulation in the final SAR image follows [45]. To reduce the scalloping effect, a novel scanning technique [45], TOPSAR (Terrain Observation by Progressive ScanSAR), was introduced. This new wide-swath mode is usually used by the SAR instrument on-board the spacecraft Sentinel-1A. While in the ScanSAR mode, the antenna is steered only in the range direction, in TOPSAR the antenna is steered in both range and azimuth. The azimuth rotation is from back to fore at a constant rotation speed, opposite to the spotlight mode. Therefore all targets are illuminated by the mainlobe of the AAP reducing

the scalloping effect. This azimuth scanning, illustrated in Fig. 2.13, results in a virtual shrinking of the AAP [46] as seen by an on-ground target. Opposite to the ScanSAR mode, the burst duration, T_B, in TOPSAR mode is typically longer and is almost equal to the footprint time, T_F, to ensure a sufficient dwell time on target. Note that the

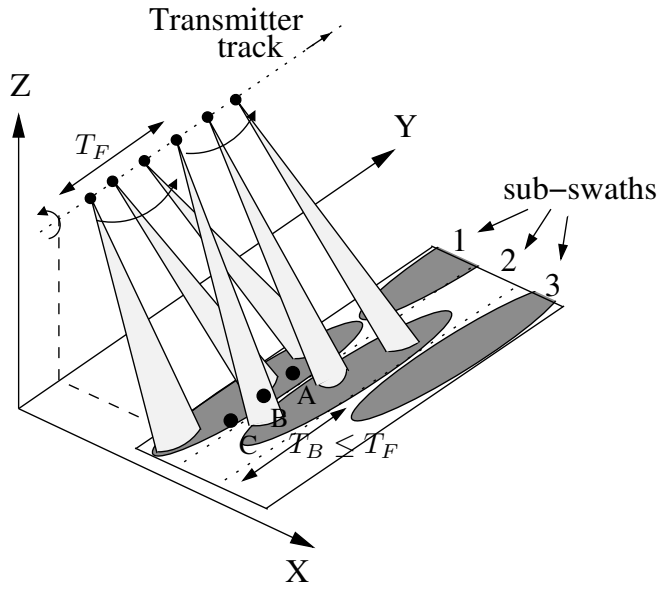

Figure 2.13: Acquisition geometry in TOPSAR imaging mode in the case of three sub-swaths as in IW mode of Sentinel-1A.

TOPSAR mode implemented on Sentinel-1A is a one-look wide-swath, i.e. $N_L = 1$ meaning that the rotating elevation beam does not illuminate twice a scatterer.

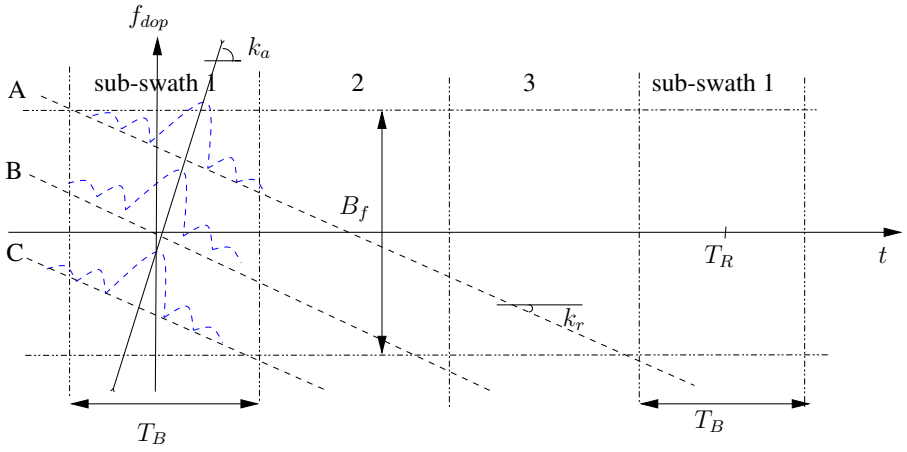

Figure 2.14: TOPSAR mode: Time-frequency diagram of three patches where the azimuth steering introduces a Doppler centroid rate k_a. The blue dashed lines represent the shrunk AAP.

Figure 2.14 illustrates the time-frequency diagram for three patches represented in Fig. 2.13 for a three sub-swath TOPSAR mode such as the Interferometric Wide Swath (IW) mode of Sentinel-1A. In this radar mode, each illuminated target experiences nearly the same AAP (blue dashed-line in Fig. 2.14) during the burst duration T_B. In both wide-swath modes, the poor cross-range resolution compared to stripmap imaging is caused by a shortened patch illumination: ScanSAR illuminates patches with a small portion of its AAP, while in TOPSAR, the shorter patch illumination is due to the along-track sweeping of the antenna beam.

Figure 2.15 depicts the acquired signal during an overpass of Sentinel-1A operating in IW mode over the ground-based receiving system in Brussels. The dashed lines demarcate the time interval spent by the beam on each sub-swath, $T_B = 0.82$ s. The duration of the mainlobe of the shrunk AAP is equal to 0.24 s which corresponds to the azimuth integration time used in monostatic SAR. This is to be compared to 0.05 s for the SWB mode of RADARSAT-2. This multiplication factor of 5 in dwell time results in a better cross-range resolution of Sentinel-1A compared to RADARSAT-2 as listed in Table 2.1.

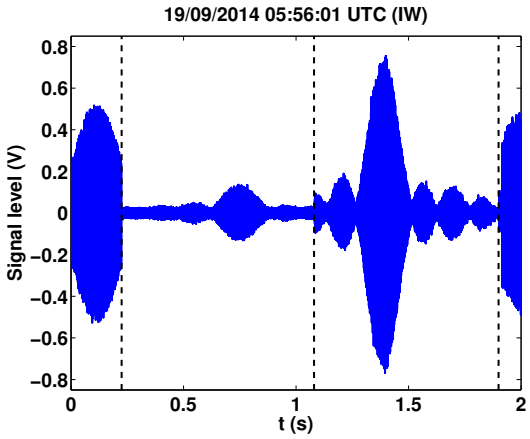

Figure 2.15: Acquired Sentinel-1A signals in TOPSAR.

2.1.7 SAR illuminators of opportunity

During this thesis, we exploited several C-band SAR satellites: ERS-2, ENVISAT, RADARSAT-1/2 and Sentinel-1A. In July 2011, ESA retired the satellite ERS-2. ENVISAT ceased to transmit in April 2012 making the RADARSAT constellation the only C-band SAR satellites till the launch of Sentinel-1A in April 2014. Table 2.1 gives the

main characteristics of the exploited SAR transmitters in this thesis with their mono-static spatial resolution, $\delta_r \times \delta_{az}$. Note that RADARSAT-2 was re-programmed to operate in TOPSAR mode to test this new mode in support of the Sentinel-1 mission [47].

Table 2.1: Characteristics of the C-band radar satellites used in this thesis.

SAR satellites	Centre frequency (GHz)	Mode	PRF (Hz)	Bandwidth (MHz)	Pulse duration (μs)	$\delta_r \times \delta_{az}$ (m)	Cycle (days)	Number of sub-swaths
AMI ERS-2	5.300	Stripmap	$1640 - 1720$	15.55	37.12	30×30	35	1
ASAR	5.331	Stripmap	$1600 - 2100$	16 maximum	21	30×30	35	1
ENVISAT		ScanSAR WS				150×150		5
[48]		ScanSAR GM				1000×1000		5
RADARSAT-2	5.405	Stripmap (standard)	$1000 - 3800$	$11.56 - 17.28$	21-42	9-13.5 $\times$ 7.7	24	1
[49]		ScanSAR narrow		11.56		37.7-79.9 $\times$ 50		$2 - 3$
		ScanSAR wide		11.56		72.1-160 $\times$ 100		4
Sentinel-1A	5.405	Stripmap	$1000 - 3000$	up to 100	$5 - 100$	1.7-3.6 $\times$ 4.3-4.9	12	1
[50]		TOPSAR IW				2.7-3.5 $\times$ 22		3
		TOPSAR EW				7.9-15 $\times$ 43		5

2.2 Bistatic SAR

2.2.1 Bistatic geometry

Although many bistatic configurations can be considered, Fig. 2.16 illustrates the bistatic configuration of the experiments consisting of a space-based radar as transmitter and a stationary ground-based receiver. In that configuration, a stationary receiver on the roof of a building is used for practical experimental reasons (easy to deploy and low cost). The same coordinate system (X,Y,Z) as in the monostatic case (Section 2.1.2) is considered. The bistatic angle β is the angle between the transmitter and the receiver with the vertex at the target [51, Chapter 3]. R_B is the distance between the transmitter and the receiver.

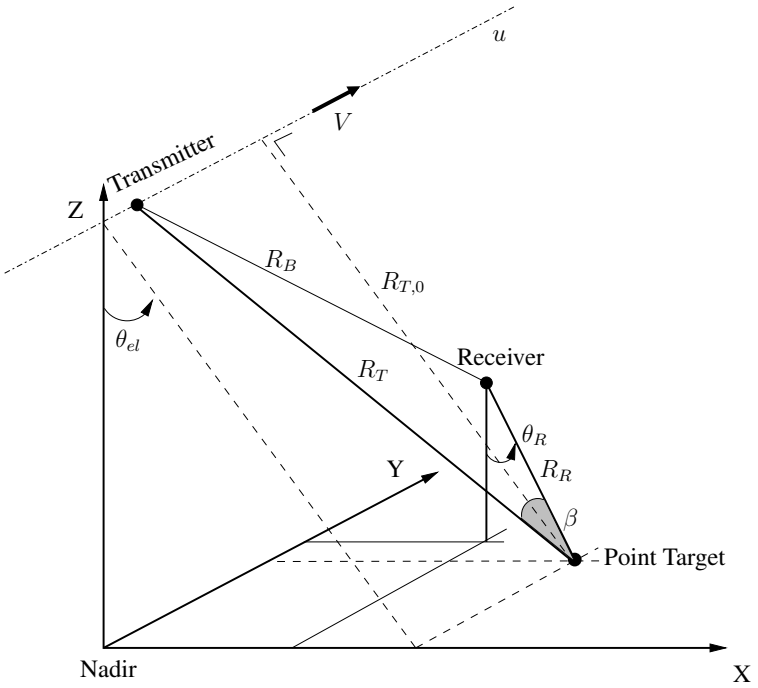

Figure 2.16: Bistatic SAR geometry.

Figures 2.17 show a cross-section perpendicular to the flight path of the SAR instrument. In monostatic SAR, targets at the same range are located on a sphere centred on the position of the SAR satellite. The intersection of this sphere with the Earth's surface is a circle. In a bistatic system, the surfaces of equal range are ellipsoids with the transmitter and receiver at the foci. The isorange contours are the intersection of these ellipsoids with the Earth's surface as illustrated in Fig. 2.17 (b). Assuming a locally flat Earth, ellipses result. Points M and N illustrate the 'left-right' ambiguity of

SAR systems. SAR systems are not able to differentiate return signal from point M and N as the return times from these two points are similar. This ambiguity can be resolved by the directivity of the transmit-receive antenna in the monostatic case and by the directivity of the receive antenna in the bistatic case.

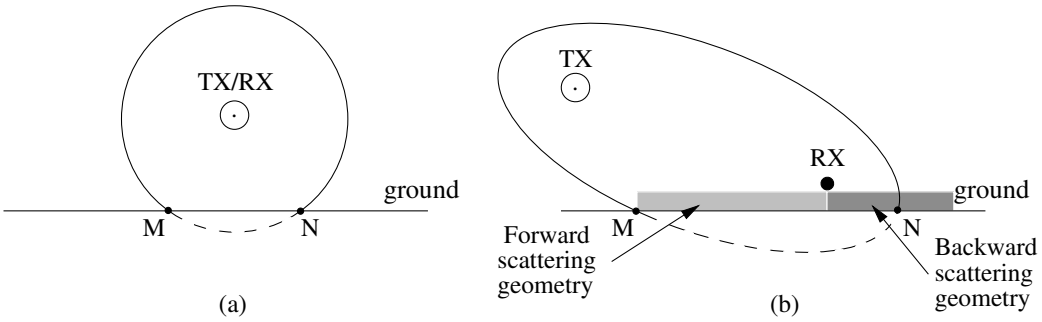

Figure 2.17: Isorange contours: Cross-section perpendicular to the flight path of (a) a monostatic radar and (b) the transmitter of a bistatic radar.

The knowledge of the geometry is a key element in SAR processing. In non-cooperative BSAR, the trajectory of the transmitter is not known and overpass times of the spaceborne transmitter are predicted using the Simplified General Perturbations version 4 (SGP4) orbit propagation algorithm [52]. The SGP4 model is one of the mathematical models for prediction of satellite position and velocity vectors. The Two-Line Keplerian Element (TLE) sets, a set of mean orbital elements, are used as input to the orbit propagator and are made publicly available on the Internet by the US Joint Space Operations Center (JSpOC). They are regularly updated in order to reflect small orbital changes. Taking into account the satellite's antenna footprint, the positions of the receiver and the scene to be imaged, the time of overpass of the satellite can be estimated.

2.2.2 Bistatic imaging

2.2.2.1 Range compression

The only difference with the monostatic range compression is that the direct signal is used as the reference signal for pulse compression. In practice, the parameters of the direct signal are estimated using a synchronisation algorithm as described in detail in Chapter 4. As this reference signal contains the delay and associated phase of the direct transmitter-to-receiver signal, the range-compressed data are now range-aligned

relative to the direct signal. A range-compressed bistatic image of a RADARSAT-2 acquisition is depicted in Fig. 2.18 as a function of the relative bistatic range, $R_T + R_R - R_B$, which is the bistatic range relative to the distance transmitter-receiver. The vertical axis in Fig. 2.18 represents the pulse index number which can be converted in slow-time using the PRF. Large correlation peaks corresponding to the direct signal at zero range can be seen which are modulated by the AAP of the transmitter, the AAP of the receiver being wider. On the left of those high correlation peaks, the range sidelobes of the direct signal are visible and on the right, between 0.1 and 0.25 km, echoes from scatterers. The hyperbolic shape of the range history of possible scatterers is not visible due to the limited extent of the azimuth recording.

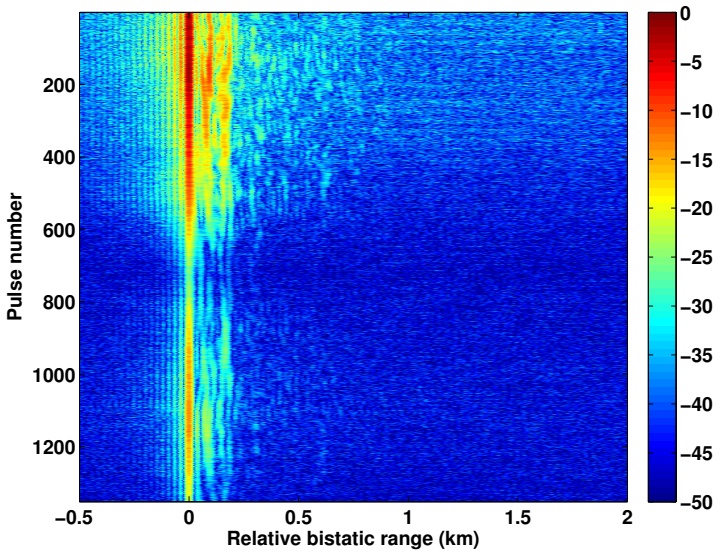

Figure 2.18: Range-compressed image of a RADARSAT-2 acquisition in dB.

2.2.2.2 Azimuth compression

In BSAR, the range history of a target is the sum of the instantaneous slant range to the transmitter, R_T, and the range to the receiver, R_R, and is given by

$$\begin{aligned} R_{bi}(u) &= R_T(u) + R_R \\ &= \sqrt{R_{T,0}^2 + V^2u^2} + R_R \end{aligned} \tag{2.18}$$

The extra subscript 0 in $R_{T,0}$ denotes the slant range of closest approach to the transmitter. Expanding (2.18) about $u = 0$ corresponding to the slant range of closest approach to the transmitter and keeping the first two terms, $R_{bi}(u)$ can be expressed as

$$R_{bi}(u) \approx R_{T,0} + \frac{V^2u^2}{2R_{T,0}} + R_R. \tag{2.19}$$

Using typical values, it can be shown that terms higher than second order are small enough to neglect considering the space-ground bistatic geometry studied in this thesis. In the BSAR configuration we consider, the range from a target to the receiver, R_R, is constant and is only a function of the position of the receiver. Hence, the range history of a target is only due to the motion of the transmitter yielding a quadratic phase history. $R_{T,0}$ will determine the curvature of the hyperbola. That means that two targets at the same bistatic range will present different range history curvature if their slant ranges of closest approach to the transmitter are different. This results in a translational variant azimuth matched filter. This is generally the case of BSAR systems [53]. Following (2.18), the azimuth matched filter must be computed for each image pixel in ground range which results in an increase of the computation load of BSAR imaging compared to monostatic SAR imaging.

The azimuth matched filter provides a correct estimation of the reflectivity of a patch if the phase of the matched filter perfectly matches the phase history of the signal at each pulse. For this assumption to hold, the target must be located at precisely the anticipated position and the antenna phase centres of the transmitter and the receiver must also be known. Inaccurate knowledge of the bistatic geometry manifests itself as slow time-varying phase errors, which may cause image shift or defocus. This is evaluated in Chapter 4. Besides, the range-compressed data are available only at fast times which are integer multiples of the sampling interval. An approximation is done by taking the nearest neighbour range-compressed sample as azimuth locus.

Figure 2.19 (a) depicts an ERS-2 bistatic SAR image in stripmap mode. The range sidelobes of the direct-path signal are clearly visible. Figure 2.19 (b) is a closer view of the position of the receiver around which elliptical isoranges appear due to the range sidelobes resulting from the range matched filter. The range sidelobes pattern are modulated by the azimuth synthesised pattern resulting of the aperture synthesis in azimuth. As can be seen in Fig. 2.19 (a), the patch circled in red is ambiguous in azimuth. Note that the ambiguity has no consequence as the receive antenna is pointing in one direction (Eastwards, i.e., to the right on the picture) and the backlobe of the receive antenna is small.

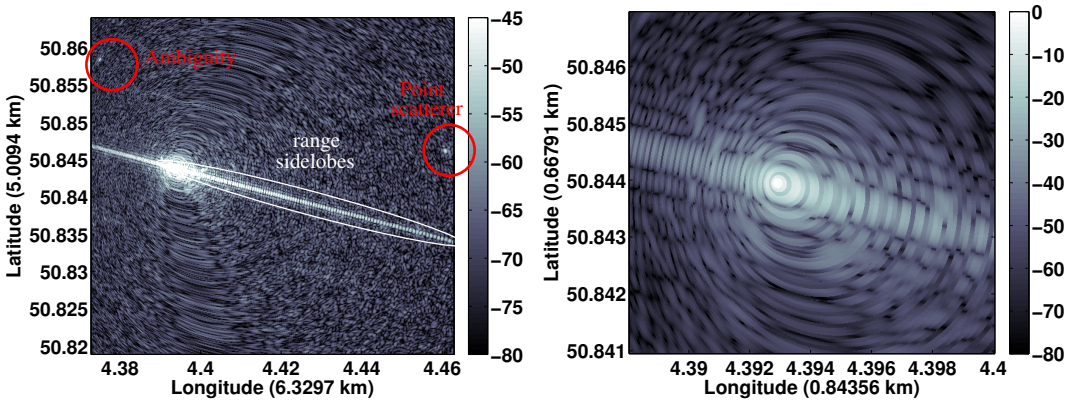

(a) (b)

Figure 2.19: (a) Bistatic SAR image using ERS-2 signal (29/10/2010 10:36:38 UTC) which corresponds to a descending orbit acquisition over Brussels, (b) detail around the position of the receiver (logarithmic scale).

2.2.3 Bistatic resolution

2.2.3.1 Bistatic range resolution

The bistatic range resolution [51, Chapter 4] is dependent upon the geometry of the system, i.e. satellite-receiver-target relative positions and is defined as the distance between two concentric bistatic isorange contours, or ellipses. This distance, however, varies with the relative target position. The bistatic slant range resolution is given by

$$\delta_{r,bi} = \frac{c}{2B\cos(\frac{\beta}{2})} \tag{2.20}$$

In this work, a quasi-monostatic geometry is studied leading to nearly the same slant-range resolution as in monostatic SAR imaging as the bistatic angle is close to zero. The bistatic ground range resolution in a flat reflection area can be approximated by [25]

$$\delta_{gr,bi} = \frac{c}{B|\sin(\theta_{el}) + \sin(\theta_R)|} \tag{2.21}$$

where B is the bandwidth of the transmitted signal and θ_{el} and θ_R are the incident angles with respect to the normal to the ground plane for the transmitter and receiver, respectively as represented in Fig. 2.16 (positive counter-clockwise from nadir). If both incidence angles are the same, (2.21) becomes the well known monostatic ground range resolution (2.13).

In space-ground BSAR, two different geometries can be considered yielding different bistatic ground range resolutions as depicted in Fig. 2.17. The backward scattering geometry occurs if both the transmitter and the receiver are on one side of the observed area. This corresponds to a bistatic angle close to zero, i.e. a quasi-monostatic (small bistatic angle) geometry. In this geometry, a better ground-range resolution than in monostatic SAR imaging is expected thanks to the incident angle θ_R close to 90° in (2.21). The forward scattering geometry is here understood as the geometry in which the observed area is between the transmitter and the receiver. This geometry is not to be confused with the forward scattering region, which corresponds to a bistatic angle close to 180°, in which the scattering coefficient is enhanced due to the Babinet's principle [1, Chapter 25]. According to (2.21), the backward scattering geometry yields the best bistatic slant-range resolution [25]. On the other hand, the scattered signal amplitude is typically higher in the forward scattering geometry [6, Chapter 9] as $\theta_{el} \approx -\theta_R$, i.e. in the specular direction.

2.2.3.2 Bistatic azimuth resolution

Opposite to monostatic SAR, the azimuth resolution direction in BSAR is not necessarily orthogonal to the range resolution direction. In BSAR, the azimuth resolution [54] is defined in the direction which is parallel to the velocity of the transmitter (in the case of a non-moving receiver). The azimuth resolving capability mainly depends on the illumination pattern during the integration time, i.e. how long the combined antenna pattern of the transmitter and the receiver illuminates the patch. In [51, Chapter 7], the cross-range resolution direction is defined and is perpendicular to the range resolution direction, i.e. along the bistatic isorange contour. In a quasi-monostatic geometry, the cross-range direction and the azimuth direction are nearly parallel. If the azimuth and the range directions are not orthogonal, the measured resolution is a combination of both azimuth and range resolution what makes the analysis of the azimuth resolution problematic. For this reason, we consider the cross-range resolution in the remainder of the thesis to compare the performance of the BSAR imaging with that of the monostatic SAR imaging.

2.3 Summary

In this chapter, monostatic and bistatic SAR imaging have been studied in terms of geometry, resolution and SAR processing. Identification of similarities and differences between the range histories of the targets have been discussed. As in the monostatic case, the most straightforward and usual way to produce a BSAR image is by using the matched filter. Then, the difference between azimuth resolution and cross-range resolution in BSAR was examined; this latter will be used in the rest of this thesis.

It was also shown that the wide-swath radar imaging modes prove to be rather complex to exploit compared to the traditional stripmap mode. This is one of the challenge that this thesis has taken up.

Chapter 3

Research context

In this section, the state of the art of space-ground bistatic SAR imaging using monostatic radar as illuminator of opportunity is analysed across the three main difficulties appearing when bistatic configurations are involved:

- Signal synchronisation
- Bistatic SAR focussing
- Direct signal interference

3.1 Signal synchronisation

The first obvious challenge appearing in bistatic configuration is the time and phase synchronisation required between the transmitter and the receiver.

Time synchronisation refers to the process of recovering the time of transmission of each pulse needed to compute the range-to-target in the SAR processing. In the one-stationary configuration considered in this thesis, the precision requirements of range measurement are not stringent and are analysed in Chapter 4.

As SAR is a coherent imaging system, a phase synchronisation step is essential: the receiver and the transmitter must stay coherent during the illumination time of the scene. The receiver requires the knowledge of the transmitted phase to perform SAR imaging. In monostatic SAR, the same local oscillator is used for both the transmit and the receive function. In bistatic SAR, the separation between the transmitter and the receiver leads to the use of independent oscillators for modulation (at the transmitter side) and demodulation (at the receiver side) of the radar pulses [55]. Any deviation between

the two oscillators will result in a phase error in the bistatic data which, depending on magnitude and nature, will differently affect the SAR imaging [56, Chapter 5]. As will be shown in Chapter 4, a distinction is made between low-frequency phase errors and high-frequency phase errors. Low-frequency phase errors, e.g. due to a constant frequency offset between the two oscillators, must not exceed $\frac{\pi}{2}$ for the considered integration time whereas the allowable Root Mean Square (RMS) value of high-frequency phase errors such as the inherent phase noise in each oscillator is typically $4°$.

Let us analyse the evolution of the phase error due to the inaccuracies in carrier frequencies of the two distinct local oscillators, one at the transmitter with carrier frequency f_T and the other at the receiver with carrier frequency f_R. The inherent phase noise of each local oscillator is here not considered as this phase noise only depends on the local oscillator itself and not on the synchronisation algorithm. For illustrative

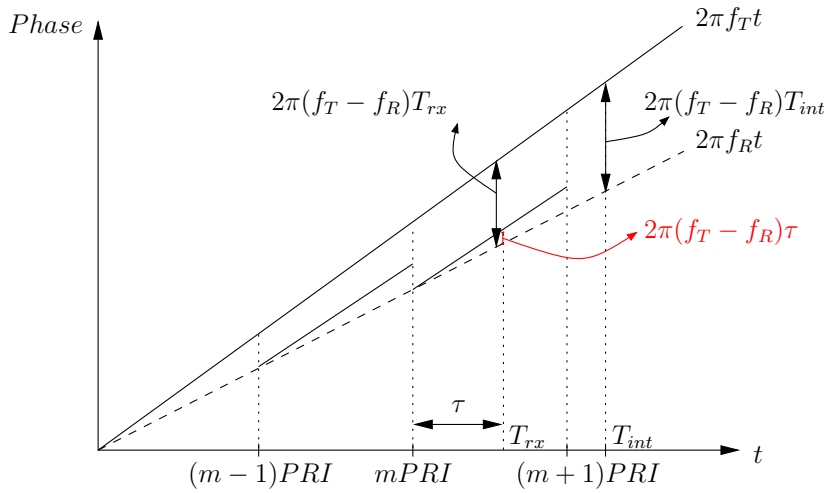

Figure 3.1: Evolution of the phase error due to a constant frequency offset between the local oscillators.

purpose, a constant frequency offset between the two local oscillators is considered and illustrated as a function of the propagation time, t, in Fig. 3.1. A frequency difference between the two oscillators results in a linear increase of the phase which is equal to $2\pi(f_T - f_R)t$. If a phase synchronisation is performed once at the beginning of the acquisition, this phase error will drift toward a maximum value equals to $2\pi(f_T - f_R)T_{int}$ with T_{int} the coherent integration time. This is called indirect phase synchronisation [51]. For one considered patch, the phase error is proportional to the time interval between the time at which the synchronisation between the transmitter and the receiver is

performed ($t = 0$) and the reception of the pulse (T_{rx}). If a direct phase synchronisation on a pulse-to-pulse basis is performed, the phase error will be reinitialised at each receiving pulse. This phase error will be equal to $2\pi(f_T - f_R)\tau$ with $\tau = \tau_{echo} - \tau_{dir}$ the propagation time difference between the reflected and direct signals. Note that the phase error is different for each isorange contour. This phase error is much smaller than in the indirect phase synchronisation. Hence, for the same phase error, a larger difference between the frequencies of the local oscillators can be accepted in the case of a direct phase synchronisation. Therefore, direct synchronisation on a pulse-to-pulse basis is considered in this thesis.

In cooperative bistatic systems, there are different ways to overcome the phase error due to the drift between the local oscillators. One solution is to use Global Positioning System (GPS) timing signals to synchronise the transmitter and the receiver [57] or ultra-high-quality oscillators [58]. Another approach is to record the relative phase offsets between the oscillators, as it is done in the TanDEM-X mission [20], which requires a two-way dedicated link.

However, if the receiver uses a non-cooperative source of opportunity, none of these strategies can be applied directly. In this case, to solve the problem of synchronisation between the transmitter and the receiver, an additional channel, called synchronisation channel, receiving the direct pulses from the transmitter is usually built [12, 23–25, 59]. Then, the direct signal is used to perform time and phase synchronisation during the pulse compression step preceding SAR imaging [60–62]. In this thesis, the antenna oriented towards the scene to image and receiving the reflected pulses can also be used as synchronisation channel as the SNR of the direct signal is sufficient as demonstrated in Section 7.3.

3.2 Bistatic SAR focussing

3.2.1 Introduction

Depending on the bistatic configuration and on the radar imaging modes, different SAR focussing algorithm can be used. Considering the geometry, one may make the distinction between azimuth-invariant and azimuth-variant configurations [53, 63]. The radar imaging mode operated by the transmitter also influences the bistatic SAR focussing. As the main contribution of this work consists in processing ScanSAR data [64], the

classical ScanSAR focussing is explained in Section 3.2.4

3.2.2 Azimuth-invariant configuration

Azimuth-invariant configurations include configurations in which the transmitter and the receiver move in parallel tracks (same or different altitudes) with constant identical velocities and the tandem configuration [65] in which the transmitter and the receiver follow each other with equal velocities on the same track with some fixed offset. Those Translational-Invariant (TI) configurations may benefit from the convolution property of the FFT like monostatic configuration. In [65], the idea is to transform the tandem bistatic raw data into monostatic SAR raw data by a pre-processing step called the Rocca smile operator. After this transform, the mature traditional monostatic SAR algorithms can then be used for bistatic SAR imaging. This concept was demonstrated for the tandem configuration but has been further extended to the general bistatic case in [66].

3.2.3 Azimuth-variant configuration

Azimuth-variant configurations include configurations in which the transmitter and the receiver move with constant but different velocity vectors in magnitude, in direction or both. The bistatic configuration considered in this work in which one platform remains stationary and the other travels with constant velocity vector is part of this category. Those Translational-Variant (TV) configurations for which imaging geometry changes with time cannot be focussed exactly using one of the efficient Fourier-domain focussing algorithms. Therefore, focussing using a time-domain algorithm is preferred to obtain an accurate bistatic image.

Time-domain focussing algorithms [67, Chapter 4] are universally applicable to any geometrical configurations, bistatic as well as monostatic configurations, and are relatively simple to implement. However, these algorithms have high computational loads as they form the image by processing one patch at a time. Therefore, new bistatic algorithms are derived in order to focus these azimuth-variant bistatic configurations in a more efficient way.

Another method to derive the bistatic SAR algorithm is to develop an analytical explicit expression of the point target's reference spectrum. A representative analytical explicit expression of this spectrum is the Loffeld Bistatic Formula (LBF) [68] which

is used to derive a number of bistatic processing algorithms [69]. The accuracy of these algorithms is limited by the accuracy of the derived analytical spectrum. The one-stationary bistatic SAR case studied in this thesis is substantially simpler in concept and operation than the general bistatic case configuration analysed in [68] and the general translational-variant algorithm developed in [68] will not be followed here.

In the space-ground bistatic SAR configuration, several bistatic SAR processors have been described in the open literature. Several authors [24, 61, 70–72] expend effort in modifying the traditional monostatic SAR frequency-domain processors to process one-stationary bistatic data. By making assumptions in the considered bistatic geometry, one can exploit the efficiency of those FFT-based processors at the expense of a loss in image quality for certain imaging configuration.

[28, 31, 73] use the Back-Projection (BP) algorithm [67, 74, 75] which is not as time efficient as FFT-based algorithms but which does not require any assumptions. In this work, the BP algorithm has been also adopted to focus the bistatic SAR image due to its ease of implementation and its accuracy.

3.2.4 Wide-swath mode illumination in BSAR

A classical way to focus ScanSAR data [76] is to process each burst independently. If the area of interest is illuminated by a number of bursts N_L, the focussed burst images can be added incoherently for the purpose of speckle reduction. This single-burst processing results in the well-known poor cross-range resolution of the ScanSAR mode.

One way to improve this cross-range resolution is to process coherently the N_L bursts yielding a single-look image. In this case, azimuthal grating lobes appear in the SAR image [77] due to the non-continuous azimuthal phase history. Those grating lobes can be reduced in a post-processing step [78] leading to the same poor cross-range resolution as the incoherent processing. As a consequence, in ScanSAR mode, bursts are almost always processed independently.

However, in a bistatic configuration with a receiver constantly pointing to the scene of interest, the returns originating from the elevation sidelobes of the transmit antenna may enter the mainlobe of the receiver with a sufficient SNR. In that case, a continuous illumination occurs and the resolution of the conventional stripmap imaging mode can be recovered. Recovering the resolution of the stripmap imaging mode from data

obtained from SAR systems operating in wide-swath mode is novel and is explained in detail in Chapter 5.

3.3 Direct signal interference

SAR imaging in the vicinity of the stationary receiver due to the strong direct-path signal is a particular challenge in BSAR. To perform SAR imaging in the surrounding of the receiver, particular attention must be paid to the direct-path signal. The conventional MF used in SAR processing generates range and azimuth sidelobes that can hide weaker scatterers located in the immediate surrounding of the receiver. Furthermore, the long pulse length of the transmitted signal and the short imaging range in the bistatic geometry studied in this thesis means that the pulsed SAR transmitter behaves like a continuous wave system. The attenuation of the direct signal before entering the acquisition card will thus impact the required dynamic range of the A/D card. The dynamic range is further discussed in Appendix A.3.

Attenuation of the effect of the direct-path signal can be done in different manners. A practical solution for this is to isolate the antenna of the surveillance channel, i.e. the channel oriented to the area of interest, from the transmitter. This can be done by exploiting its antenna pattern or by choosing a measurement environment where the line of sight to the transmitter is obstructed by a building [10]) or by physically shielding the surveillance channel with synthetic material such as Radar Absorbing Material (RAM) [79].

If the receiver consists in an array antenna, spatial nullsteering, as analysed in [8, 80], can be used to steer a null in the direction of the transmitter in order to attenuate or null the direct-path signal itself. This requires a non-obvious calibration step. One of the drawbacks of spatial nullsteering is a shadowed area that can appear on the SAR image due to the suppression of the backscattered signals. The considered spatial filter will steer a null in a cone angle [81] corresponding to the direction of the transmitter and will affect other directions according to its beampattern. The effect of the beampattern of the spatial filter will be reflected on the SAR image. This shadowed area can be bypassed by reorienting the Uniform Linear Array (ULA) such as the cone is not in the desired direction of imaging. Furthermore, the beampattern of the spatial filter is more directive for increasing antenna elements in the antenna array. No antenna element

would then be allocated to point towards the transmitter and the reference signal could be extracted using spatial beamforming as well.

Reducing the range and azimuth sidelobes can also be performed using apodization [82]. This method has the drawback to degrade the resolution.

Finally, another method to suppress the interference in passive SAR imaging consists in using a CLEAN-like algorithm. Fairly preliminary results have been presented in [83, 84]. The central assumption of this algorithm is that the received signal is made up of a sum of target echoes, including the strong direct path signal, multipath and noise. This assumption can lead to a decomposition of the received signal into a basis of non-orthogonal functions, where each basis function or mode is a time-delayed version of the reference signal. This decomposition lets to identify the dominant components (direct signal and closest strong reflections) and remove their contribution from the received signal.

In this work, the method used to mitigate the direct signal power received in the surveillance channel is a simple combination of two above mentioned methods. The antenna of the surveillance channel is pointed away from the transmitter so that the direct signal is received in the backlobe, or, due to satellite motion, in the sidelobe of the antenna. Besides, some anechoic chamber cladding material is also installed at the back of the antenna to provide further attenuation. The combination of both methods will sufficiently attenuate the direct signal according to the power budget analysis in Appendix A.3.

3.4 Interrupted SAR

SAR data is usually recorded continuously along the track of a sensing platform. However, in some situations, the data may be interrupted leading to gaps in the SAR phase history. Examples of such situations are data corruption, alternating polarisations, presence of radio frequency interference, exchange of necessary calibration information in between platforms, e.g., in the case of TanDEM-X [85], mode/function interleave [86] or wide-swath mode operation, e.g. in ScanSAR or TOPSAR, among others. While corruption of the data or the presence of radio frequency interference might be a clear example of random pattern, the others might more often fall into the periodic interruption case. These gaps in the phase history translate into degradation of the resulting

conventionally generated SAR images. These degradations can be more or less accentuated depending on the gap pattern and the amount of missing data. [87] analytically studied the impact of the gap pattern on the SAR imagery. First, the periodic case introduces ghosts in the azimuth direction. Then, in contrast to the periodic pattern, the random pattern introduces leakage throughout cross-range. This leads to a contamination of the shadows from interfering pixels. The influence of the gap pattern on a scene with point targets has also been analysed in [86, 88, 89] which demonstrate that the more random the gap pattern, the better. As a consequence, novel image formation algorithms are required to mitigate artifacts.

Several methods exist to reconstruct SAR data acquired in interrupted operation. To recover the missing data, assumptions have to be made on the data sequence and thus on the SAR image to reconstruct. Intuitively, these assumptions can be seen as attempts to add extra information to the reconstruction problem. The missing data can be recovered by making assumption in the slow-time domain or in the spectral domain.

A traditional way to deal with missing data is to use the MF processing. However, grating lobes appear in the resulting SAR image [77] and make further exploitation impossible. One can use spectral estimation methods [86, 90, 91] to recover the missing data which must then be followed by a SAR focussing algorithm. In the spectral estimation methods, one can distinguish parametric methods from the non-parametric ones [92]. In parametric methods, the SAR phase history is considered to be a realisation of a wide sense stationary process. This process can be described by means of a parametric model, whose coefficients can be estimated using one of the several methods established in the literature. If an Auto-Regressive (AR) model is considered, the Burg Algorithm [86] can be used to estimate the parameters of the process as in [91]. In this method, the reconstruction of the azimuthal signal is carried out locally on a gap to gap basis. The coefficients of the AR-model are estimated using the segment before the gap and again using the one after the gap. The two sets of reconstructed data are then combined to give the final coefficient estimation. The missing data is then recovered feeding the gapped signal into an Infinite Impulse Response (IIR) filter build from the estimated coefficients. The reconstruction is performed considering one range bin at a time. In this method, the missing data are considered to be part of an auto-regressive stationary process which is valid for only small gaps as demonstrated in [86].

The non-parametric spectral estimation methods are not based on any model. One of them is the Gapped-Amplitude and Phase Estimation of a Sinusoid (GAPES) method [93, 94]. The GAPES method consists in a non-parametric adaptive filter-bank approach using minimum least squares criterion to iteratively estimate the spectrum and invert the missing samples. The GAPES method is an iterative process in which the spectral content of the missing data is assumed to be given by the available data. This method is therefore suitable whenever the correlation between the missing data and the available data is high enough to satisfy this assumption. This is mostly the case for point-like scatterer. This method first estimates the spectrum using the Amplitude and Phase Estimation of a Sinusoid (APES) method [94] on the available data and then the missing data are inverted by minimising the error they introduce in the previously estimated spectrum. A second non-parametric spectral estimation method is the Papoulis-Gerchberg (PG) estimation method [95]. The PG method assumes that the signal to be restored is band-limited. It estimates the spectrum of the complete signal and thus interpolates the missing data by iteratively removing the high frequency components present in that spectrum due to the loss of information in time domain. According to [91], this method requires a large number of iterations to converge which makes this reconstruction method less attractive.

Since this is a problem of missing data, sparse recovery methods, better known under the name of Compressive Sensing (CS) [96], can be used to extrapolate the interrupted data. SAR imaging using CS has been already studied in [87, 89, 97–102]. Sparse recovery methods make the assumption that the recovered data is sparse in an appropriate basis and their performance depends on the gap pattern. Sparse recovery methods comprise global optimisation algorithms such as Basis Pursuit DeNoising (BPDN) algorithm [103], Spectral Projected-Gradient L1 (SGPL1) algorithm [104], and greedy algorithms [105] such as Matching Pursuit (MP) or Orthogonal Matching Pursuit (OMP).

[97] compares the MF with a CS method on 1-D simulated sparse data and analyses the reconstruction performance in amplitude and in phase for different SNRs. [97] neglects a fraction of the acquired data randomly. Besides, the simulated targets were on the grid which shows a false impression of super-resolution. The author of [97] compares the performance on rural and urban areas.

[88] relates the mutual coherence of the measurement operator to reconstruction quality for different geometrical configurations. [89] uses SGPL1 algorithm and analyses the sparse part with CS and the non-sparse part using a Power Spectral Density (PSD).

In this thesis, the gap pattern is imposed by the measurement process. ScanSAR illumination can yield periodic gaps in the phase history when the SNR of the signals transmitted in the elevation sidelobes is not sufficient whereas a TOPSAR illumination can yield gaps at places where the azimuth pattern of the transmit antenna exhibits zeroes or when the SNR of the signals transmitted in the azimuth sidelobes is not sufficient. The theory of CS is developed in detail in Section 6.4 where it is shown to have good performance with point-like targets.

Chapter 4

Receiver synchronisation

4.1 Introduction

This chapter presents the synchronisation challenge in bistatic SAR focussing when non-cooperative transmitters are involved. Bistatic systems have to overcome two synchronisation challenges: time and phase synchronisation. Poor synchronisation will introduce phase errors along the processing aperture that, depending on magnitude and nature, will differently affect the SAR imaging. The phase errors can be classified into two classes depending on their variation over the aperture [56, Chapter 5]: low-frequency errors, which have periods larger than the coherent integration time; and high-frequency errors, which vary rapidly over the aperture and have periods less than the coherent integration time. Low-frequency errors encompass constant, linear, quadratic and higher order phase errors. Linear phase errors typically result in the shift of the point target response in azimuth direction but has no impact on SAR imaging focus. Quadratic phase errors cause broadening of the point target response. If it is space invariant, the effect is uniform defocus over the scene. One considers that, when the low-frequency phase errors are smaller than $\frac{\pi}{2}$ [6, Chapter 10], the effect on the focussed SAR point target response can be neglected. Low-frequency phase errors along the aperture can impose constraints concerning the maximal scene size to be imaged and on the maximal integration time.

High-frequency errors include sinusoidal and random phase errors and cause grating lobes to appear in the system impulse response. The inherent phase noise of a local oscillator is part of this category. A typical value for the allowable RMS high-frequency phase error is 4° [51, Chapter 13]. Typically and in particular the local oscillator used

during the experiments meets this requirement.

As there is no synchronisation link between the non-cooperative transmitter and the receiver, the time and phase synchronisation between the transmitter and the receiver is here performed using the direct-path signal which requires a line of sight with the non-cooperative transmitter.

4.2 Time synchronisation

4.2.1 Definition

Time synchronisation consists in recovering the time at which the received pulses have been transmitted by the non-cooperative transmitter. Then, the position of the transmitter with respect to the receiver at the time the pulse was transmitted is computed as described in Section 2.2.1. This is required for range measurement in SAR processing.

4.2.2 Procedure

The reception time of each pulse is obtained by applying a matched filter to the direct-path signal and detecting the peaks of power at its output. The timestamp of each peak is used as the corresponding start time for the reflected signal. Then, the time of transmission of the received pulses is obtained iteratively taking into account the propagation time and the positions of the satellite given by the orbit propagator. The precision of the positions of the satellite depends on the accuracy of the orbital elements and the accuracy of the orbit propagator itself. There are of course uncertainties in the available ephemerides and trajectory errors result in phase errors along the aperture.

Table 4.1: Simulated bistatic scenario based on a Sentinel-1A IW2 signal parameters.

Parameter	Unit	Value
Wavelength, λ	cm	5.55
Pulse duration, T_p	μs	61.9
Chirp rate, α	GHz/s	779
Measured bistatic slant-range resolution, $\delta_{r,bi}$	km	0.01
Coherent integration time, T_{int}	s	1
Satellite speed, V	km/s	7
Scene extent	km	44×43
Height of the receiver, h_R	m	50

4.2.3 Impact of satellite position measurement error

Let us analyse the impact of a position measurement error of the transmitter on the SAR focussing. We compare a true and a range shifted orbit. We consider a range error on the orbit of the spaceborne transmitter of 5 km which is much larger than what is expected. The simulation parameters are listed in Table 4.1 and are based on the Sentinel-1A signal characteristics. Figure 4.1 represents the relative bistatic range for the entire scene to be imaged. The shape of the bistatic isorange contours is elliptical which is more visible close to the receiver represented in Fig. 4.1. The look direction of the satellite is represented by an arrow.

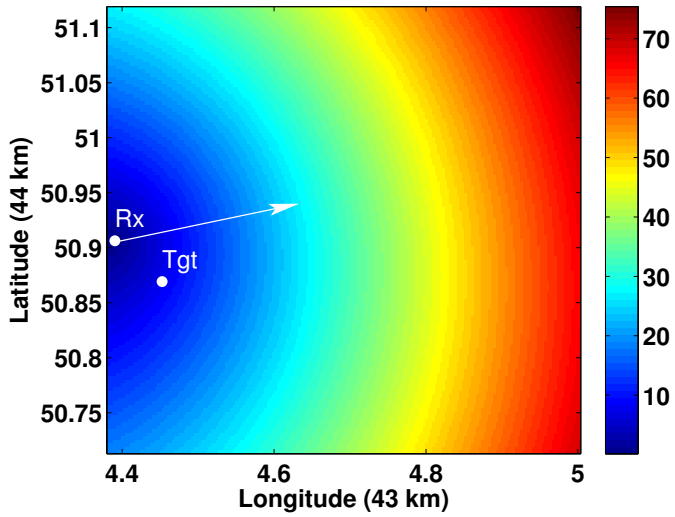

Figure 4.1: Relative bistatic range (km) for patches to be imaged, the receiver and a patch located at 6 km from the receiver are represented by white dots.

Figure 4.2 (a) represents the bistatic range of a patch located at approximately 6 km from the receiver considering a true orbit and a range-shifted orbit. Due to the limited extent of the azimuth recording, the parabolic shape of the phase history is not visible.

Since the direct signal is used to derive the matched filter as described in Section 2.2.2, the relative bistatic range $R_T + R_R - R_B$ is of interest. The error in relative bistatic ranges due to a range shift of the orbit of the transmitter is equal to a few centimetres. The history of that error is illustrated in Fig. 4.2 (b). This positioning error in range is very small compared to the bistatic slant-range resolution (2.20) in this geometry and can be considered as negligible depending on the application. This result is

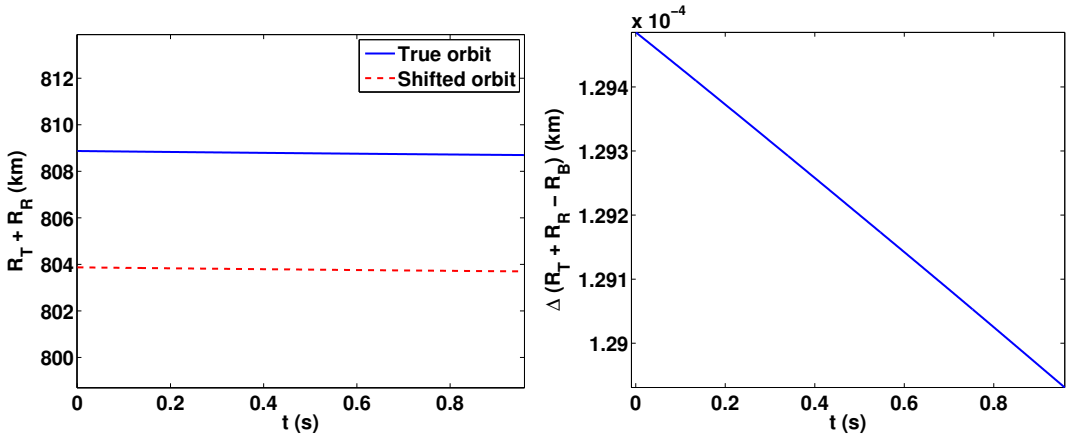

(a) (b)

Figure 4.2: (a) Bistatic range of a patch located at 6 km from the receiver during a Sentinel-1A acquisition using a true and a range shifted orbit of the transmitter (shift of 5 km) and (b) the error in relative bistatic ranges due to a range-shift error.

qualitatively consistent with those reported in [60].

The associated phase error along the aperture can be modelled by a first-order polynomial in order to estimate the linear and the constant phase error which will not affect the SAR focussing. The phase error first-order modelling is performed for the entire scene for an overestimated range shift of the orbit of 5 km. The linear phase component is equivalent to a shift in Doppler frequency, Δf, resulting in a shift in the azimuth direction given by

$$\Delta y = \frac{\Delta f \lambda R_{T,0}}{V} \tag{4.1}$$

as demonstrated in Appendix B.1. Note that the shift in the azimuth direction for one patch depends on the distance $R_{T,0}$ and on the linear phase component Δf. The shift in the azimuth direction for the entire scene extent is illustrated in Fig. 4.3 (a) while the maximal residual phase error over a typical 1-second coherent integration time is illustrated in Fig. 4.3 (b). Note that the position measurement error in azimuth is spatially variant: the patches far from the receiver shift more than the patches close to the receiver. The shift in azimuth is symmetric relative to the extended transmitter-receiver baseline but with opposite sign. The azimuthal shift is zero at patches located along the direction of the extended transmitter-receiver baseline and along a parallel to the transmitter trajectory. Indeed, for those patches, the first-order coefficient of the first-order

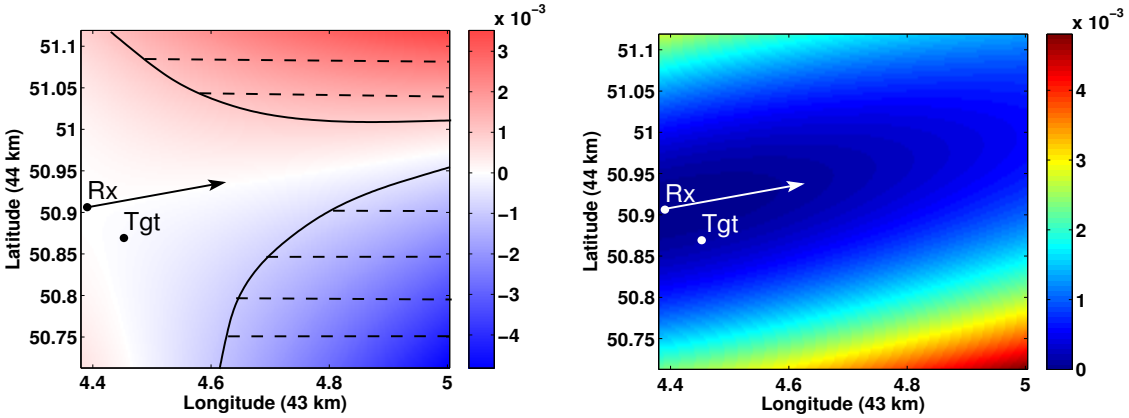

(a) (b)

Figure 4.3: (a) Shift along the azimuth direction (km) encountered by each patch of the imaged scene and (b) the maximal residual phase error (rad) after removing the bias and the linear trend due to an error of 5 km on the orbit of the spaceborne transmitter.

model is equal to zero due to their symmetric phase error. For the considered scene extent, the azimuthal shift does not exceed a few meters and the maximal residual phase error does not exceed $\frac{\pi}{2}$. Imposing a constraint on the maximal shift in azimuth or on the maximal residual phase error may limit the scene size to be imaged. As an example, the regions for which the shift in azimuth exceeds 1 m are shaded in Fig. 4.3 (a).

In practice, the orbit of the satellite is predicted with a better precision than 5 km which results in an even lower positioning error in range and an even lower azimuth shift of the patches.

For practical scene extent, the phase error along the processing aperture due to an inaccuracy in the range transmitter-receiver is small enough not to degrade SAR focussing. The associated azimuth shift is, depending on the application, typically negligible.

4.3 Phase synchronisation

4.3.1 Definition

In SAR, the receiver and the transmitter must stay coherent during the illumination time of the scene. In BSAR, the transmitter and the receiver typically use independent oscillators for modulation (at the transmitter side) and demodulation (at the receiver side) of the radar pulses. Phase synchronisation consists in cancelling out the phase

difference between the transmit and the receive oscillators to perform the SAR coherent processing.

4.3.2 Procedure

When non-cooperative transmitters are involved, the transmitted phase is not known at the receiver side. However, the phase difference between the transmit and the receive oscillators can be assumed in first approximation to be the same for the direct signal pulse and its associated echo signal pulses. Indeed, the same atmospheric effect for both signals can be assumed due to the fact that the imaging area is close to the receiver. And so the phase of the direct signal may be subtracted from that of the reflected signal in order to establish coherency with the transmitter. To do so, each reflected pulse is range compressed with a reference signal consisting in a replica of the transmitted LFM pulse that includes the phase of the corresponding direct signal pulse, i.e. the direct signal acts as a phase reference. In the case, as here, where the reference signal has a known shape (LFM signal), the reference signal can be re-synthesised using the received direct signal to estimate its parameters. The re-synthesis of the reference signal would not be necessary if the SNR of the direct signal was very large [106]. However, in a scenario in which one single channel is used for both synchronisation and imaging, the presence of nearby scatterers can degrade the SNR of the reference signal and the re-synthesis of the reference signal is then necessary.

4.3.3 Reference signal

The m^{th} transmitted chirp[1] can be expressed as

$$s_T(t,m) = e^{j[\phi_T(m)+2\pi f_T t+\pi\alpha t^2]} \tag{4.2}$$

where f_T and $\phi_T(m)$ are the centre frequency and unknown phase of the m^{th} chirp at the transmitter's local oscillator respectively, and α is the chirp rate. The signal is received with a time delay which adds an additional phase term to the received signal and is responsible for the characteristic quadratic phase evolution along the synthetic aperture. After demodulation, i.e. multiplication at the receiver with the local oscillator signal, $e^{-j[\phi_R(m)+2\pi f_R t]}$, where f_R and $\phi_R(m)$ are respectively the centre frequency and

[1]For ease of mathematical manipulation, we adopt complex notation to describe real narrowband signal in subsequent expressions. The physical signal is the real part of this complex notation.

unknown phase of the receiver's local oscillator, one obtains the received direct signal

$$\begin{aligned} s_{dir}(t,m) &= s_T(t-\tau_{dir}(m),m)e^{-j[\phi_R(m)+2\pi f_R t]} \\ &= e^{j[\phi_T(m)-\phi_R(m)]}e^{j[2\pi f_T(t-\tau_{dir}(m))-2\pi f_R t+\pi\alpha(t-\tau_{dir}(m))^2]} \\ &= e^{j[\phi_T(m)-\phi_R(m)]}e^{-j2\pi f_T\tau_{dir}(m)}e^{j2\pi\delta f t}e^{j\pi\alpha(t-\tau_{dir}(m))^2} \end{aligned} \tag{4.3}$$

with τ_{dir} the propagation delay corresponding to the direct signal and $\delta f = f_T - f_R$ is the difference in frequency between the local oscillators. The argument of the first exponential in (4.3) represents the unknown phase difference between the two local oscillators and the argument of the second exponential represents the usual phase history caused by the changing distance between transmitter and receiver over successive pulses. According to Appendix B.2, this can be rewritten as

$$s_{dir}(t,m) = e^{j[\phi_T(m)-\phi_R(m)-2\pi f_T\tau_{dir}(m)]}e^{j[-\pi\frac{\delta f^2}{\alpha}+2\pi\tau_{dir}(m)\delta f]}e^{j[\pi\alpha(t-\tau_{dir}(m))+\frac{\delta f}{\alpha}]} \tag{4.4}$$

The received echo signal can be expressed in a similar way as

$$\begin{aligned} s_e(t,m) &= s_T(t-\tau_{echo}(m),m)e^{-j[\phi_R(m)+2\pi f_R t]} \\ &= e^{j[\phi_T(m)-\phi_R(m)-2\pi f_T\tau_{echo}(m)]}e^{j[-\pi\frac{\delta f^2}{\alpha}+2\pi\tau_{echo}(m)\delta f]}e^{j[\pi\alpha(t-\tau_{echo}(m))+\frac{\delta f}{\alpha}]} \end{aligned} \tag{4.5}$$

with τ_{echo} the propagation delay corresponding to the echo signal.

In non-cooperative BSAR, the reference signal can be re-synthesised. To do so, three parameters must be estimated using the direct signal (4.3) which are the chirp rate, α, the centre frequency difference, $f_T - f_R$, and the unknown phase, $\widehat{\delta\phi(m)} = (\phi_T(m) - \phi_R(m)) - 2\pi f_T\tau_{dir}(m)$. Using this re-synthesised reference signal to derive the MF in the pulse compression step will cancel out the phase difference between the two oscillators and will phase synchronise the receiver with the transmitter. According to (4.4) and (4.5), the result of the pulse compression of one reflected pulse is a sinc function with the phase

$$\begin{aligned} \varphi(m) &= -2\pi f_T(\tau_{echo}(m)-\tau_{dir}(m)) + 2\pi\tau_{echo}(m)\delta f - 2\pi\tau_{dir}(m)\delta f \\ &= -2\pi(\tau_{echo}(m)-\tau_{dir}(m))(f_T-\delta f) \\ &= -2\pi(\tau_{echo}(m)-\tau_{dir}(m))f_R \end{aligned} \tag{4.6}$$

at the time of occurrence of the maximum. After the pulse compression, the residual phase history of a target is thus proportional to the difference in travelled distance between the direct signal and the echo signal and to f_R.

4.3.4 Estimation of the parameters of the reference signal

4.3.4.1 Frequency and chirp rate estimation

Due to the short duration of the acquisition and the high short-term stability of the local oscillator at the receiver and at the transmitter, $f_T - f_R$ is assumed to be constant from pulse to pulse. Therefore, the centre frequency difference, $f_T - f_R$, is estimated once for each signal acquisition. In ScanSAR mode, the chirp rate α can be different from one beam to the other such as in the WS mode of ENVISAT but remains constant inside a beam. Therefore, the chirp rate can be estimated once for each beam for each radar mode.

The frequency $f_T - f_R$ and the chirp rate α are estimated in the least square sense from the measurement data. This procedure is illustrated on real measurement in Fig. 4.4 (a), showing the characteristic quadratic phase of a LFM chirp after unwrapping the phase. Figure 4.4 (b) represents the real part of the measured and the synthesised LFM pulse.

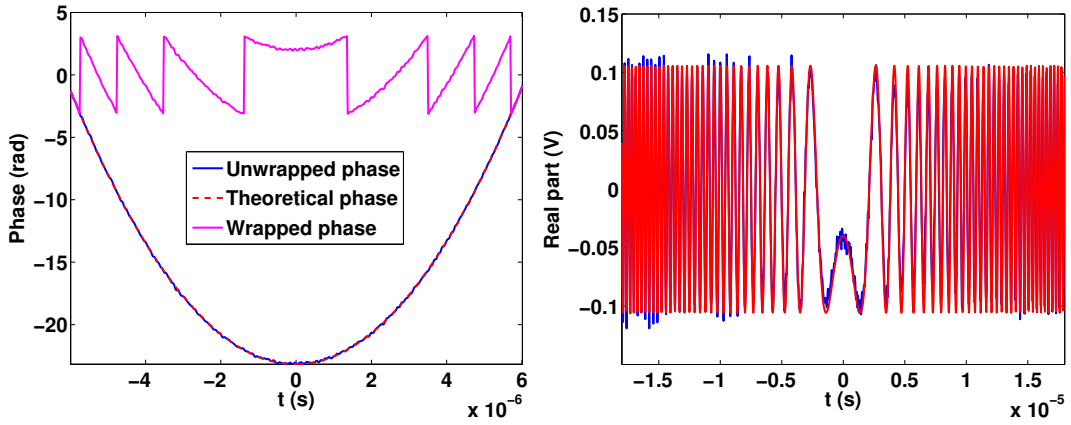

(a) (b)

Figure 4.4: (a) Unwrapped phase history of one of the received Sentinel-1A chirps and (b) a comparison between the actual chirp (blue) and the synthesised chirp based on the estimated parameters.

To evaluate the precision at which the chirp rate and the frequency are estimated, we computed the variance of the estimated chirp rate and the estimated frequency based on 1000 pulses which is the typical number of processed pulses for one acquisition. The impact of a chirp rate error can be evaluated using the Quadratic Phase Error (QPE)

which causes the broadening of the impulse response width at the output of the matched filter [35, Chapter 3]. The QPE is defined as

$$QPE = \pi \delta\alpha \left(\frac{T_p}{2}\right)^2 \tag{4.7}$$

with $\delta\alpha$ being the chirp rate error and T_p being the pulse length. It can be shown that a QPE of $\frac{\pi}{2}$ gives an impulse response width broadening of 10% or less [35, Chapter 3]. In that case, the maximal allowed error in α becomes

$$\delta\alpha_{max} = \frac{1}{2}\left(\frac{2}{T_p}\right)^2 \tag{4.8}$$

which is equal to 0.7016 GHz/s in the case of Sentinel-1A (IW2 mode). Assuming a complex Gaussian noise yielding a typical SNR for the direct-signal pulses of 20 dB, the probability that the error on the estimated chirp rate is larger than the threshold $\delta\alpha_{max}$ given the variance of the estimated chirp rate using the least square estimator is equal to 4.10^{-3}. The variance of the estimated frequency $f_T - f_R$ is estimated in a similar way. A maximal allowed error in the estimation of the frequency is set to $\delta f_{max} = 5$ kHz considering a local oscillator with a stability of 1 ppm such as a Temperature Compensated Crystal Oscillator (TCXO). The probability that the error on the estimated frequency is larger than the threshold δf_{max} given the variance of the estimated frequency using the least square estimator is found to be equal to 2.10^{-10}. Thanks to the high SNR of the direct-signal pulses, the chirp rate and the centre frequency difference are fairly well estimated.

4.3.4.2 Phase-term estimation

The unknown phase $\widehat{\delta\phi(m)}$, which varies from pulse to pulse, must be estimated at each received direct pulse. The estimation of the unknown phase of the first exponential in (4.3) is done based on the direct-path chirps which are easily located thanks to their high SNR. The estimation is performed by matched filtering the direct-path chirps with a generic chirp with a zero initial phase and with a centre frequency and a chirp rate extracted as described in Section 4.3.4.1. The phase of the output of the matched filter is the unknown phase. This process is repeated for each received direct-path chirp.

4.3.5 Impact of a frequency error

In practice, f_R in (4.6) is not known exactly and depends on the stability of the local oscillator of the receiver. Therefore, the phase of the azimuth MF (2.17) will not per-

fectly match the phase of the signal at each pulse. According to (4.6), the resulting phase error along the aperture can be expressed as

$$2\pi\delta f(\tau_{echo}(m) - \tau_{dir}(m)). \tag{4.9}$$

with δf the uncertainty of the frequency of the local oscillator of the receiver which is actually equal to the difference $f_T - f_R$. According to (4.5), the effect in the range direction of δf is a shift of the signal equal to $\frac{\delta f}{\alpha}$ which is identical for the direct signal pulses as well for the reflected signal pulses. Therefore, this shift in the range direction has no effect in the SAR image.

Let us evaluate the impact of the frequency uncertainty in the azimuth direction. A worst case uncertainty of the receiver's local oscillator of $\delta f = 25$ kHz is considered since it is the stability of the local oscillator of the receiver of the experimental system developed in this thesis. Figure 4.5 shows the evolution of the phase error along the aperture for $\delta f = 25$ kHz considering a typical 1-second coherent integration time. This phase error can be modelled by a first-order polynomial in order to estimate the linear and the constant phase error which will not affect the SAR focussing. As in

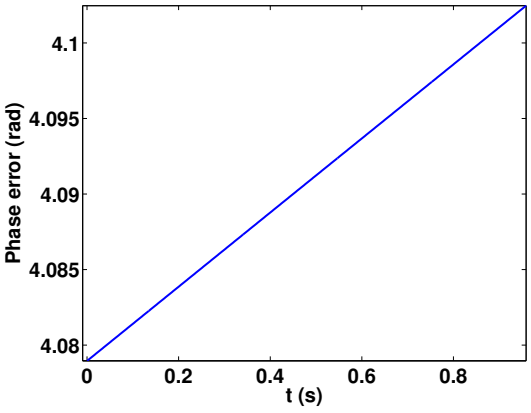

Figure 4.5: Phase error along the aperture for $\delta f = 25$ kHz modelled by a first-order polynomial encountered by a patch located at 6 km from the receiver.

Section 4.2.3, the phase error is spatially variant and is thus analysed in a similar way. The shift in the azimuth direction and the magnitude of the residual phase error after removal of the bias and the linear trend are represented respectively in Fig. 4.6 (a) and (b) for $\delta f = 25$ kHz. The shift in azimuth, which is proportional to the first-order

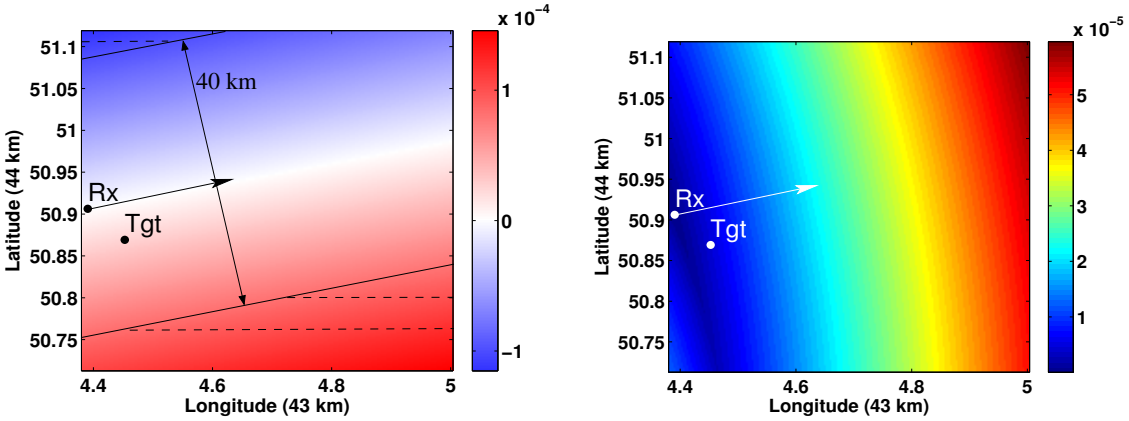

(a) (b)

Figure 4.6: (a) Shift along the azimuth direction (km) encountered by each patch of the imaged scene and (b) the maximal residual phase error (rad) after removing the bias and the linear trend for $\delta f = 25$ kHz.

coefficient of the first-order model, is symmetric relative to the extended transmitter-receiver baseline and with opposite sign. The azimuthal shift is

- zero for the patch corresponding to the location of the receiving system according to (4.9)
- zero at patches located along the direction of the extended transmitter-receiver baseline. Indeed, those patches are characterised by a symmetric phase error resulting in a first-order coefficient equal to zero.

For practical scene extent, the phase error along the processing aperture due to an uncertainty of the frequency of the local oscillator of the receiver is smaller than the limit of $\frac{\pi}{2}$ and thus will not degrade SAR focussing. The associated azimuth shift is, depending on the application, typically negligible. Imposing a constraint on the maximal shift in azimuth and a maximal residual phase error will limit the scene size that can be imaged. For example, a 10 cm maximum shift in azimuth requires to limit the scene to 20 km on both sides of the extended transmitter-receiver baseline (shaded in Fig. 4.6 (a)).

It must be noted that, in the bistatic configuration studied in this thesis, the requirement on the difference in the oscillator frequencies of the transmitter and receiver is less stringent than in [107] since the direct signal is used to derive the MF.

4.3.6 Validation of the estimated reference signal

The phase synchronisation procedure is validated by verifying that the phase history in azimuth of a patch is only proportional[2] to the path length distances between the direct signal and the echo signal. The phase error can then be estimated by comparing the phase history of the patch with a theoretical quadratic phase history.

The measured phase history of a patch in a RADARSAT-2 bistatic SAR image is depicted in Fig. 4.7 (a). Although not actually visible from Fig. 4.7 (a) due to the limited extent of the azimuth recording, the phase history is quadratic as expected. The quadratic evolution of the phase history is illustrated in Fig. 4.8 that depicts the evolution of the distance between RADARSAT-2 and the receiver during the considered acquisition. The red curve, corresponding to the recorded acquisition, is indeed seen as linear due to the short duration of this acquisition (0.5 s).

Figure 4.7 (b) illustrates the distribution of the phase history error between the measured and the calculated phase history with a small standard deviation of 0.4 rad. Several factors may explain this standard deviation, such as the influence of nearby scatterers and obviously the noise.

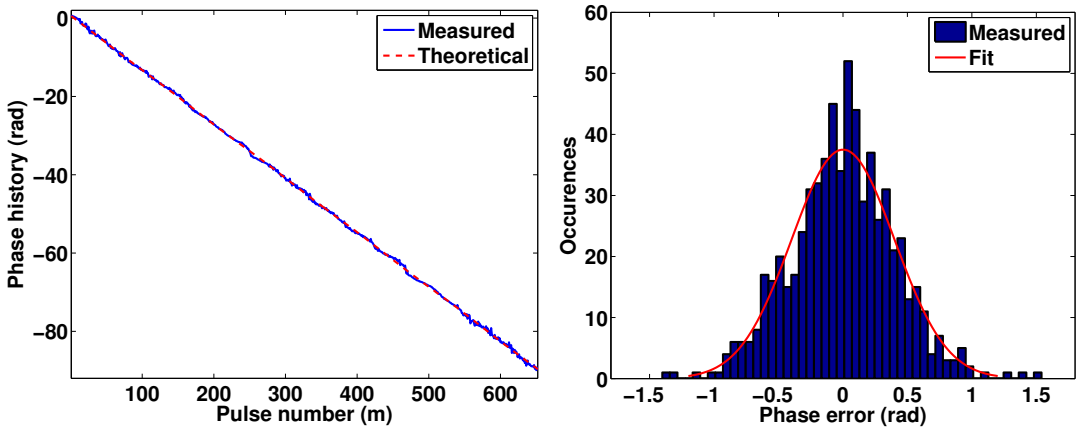

(a) (b)

Figure 4.7: (a) Measured (solid line) and calculated (dashed line) phase history of a patch and (b) the histogram of the phase history error.

[2]The unknown phase $\widehat{\delta\phi(m)}$ is assumed to be the same for the direct signal and the echo signal assuming the same atmospheric effect for both signals.

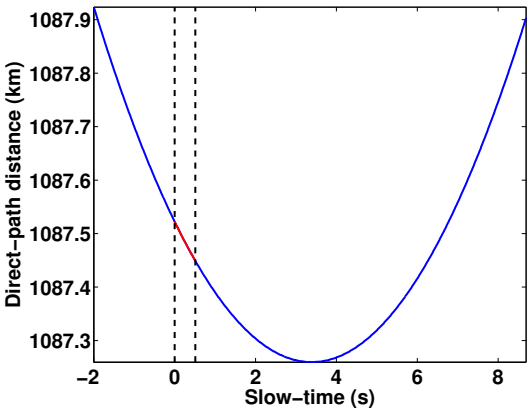

Figure 4.8: Direct-signal travelled distance during a RADARSAT-2 ascending acquisition. The dashed black lines delimit the feasible coherent integration time.

4.4 Conclusion

In this chapter, the time and phase synchronisation of the receiver with the non-cooperative transmitter in a space-ground bistatic geometry has been studied by analysing the possible sources of phase errors that can geometrically distort or even defocus the BSAR image.

It was demonstrated that the phase errors along the aperture due to a range measurement error or due to an uncertainty of the local oscillator's frequency of the receiver are low-frequency phase errors: the linear component is related to a shift in the azimuth direction which was quantified and the higher order components can yield a defocus of the SAR image. In space-ground bistatic geometry, the phase errors are typically spatially variant and setting limits to the allowable shift in the azimuth direction or to the allowable residual phase error will impose constraints on the maximal scene size to be imaged. Those limits will obviously depend on the application.

We also demonstrated that the requirement on the difference between the oscillator frequencies of the transmitter and receiver in the space-ground bistatic geometry is less stringent than in other bistatic SAR systems [107] thanks to the phase estimation of the direct signal that is used to correct the phase of the reflected signal that is performed at each pulse.

Finally, the measured phase history of a patch validated our synchronisation approach using the direct-path signal.

Chapter 5

Bistatic imaging during a wide-swath mode illumination

5.1 Concept

In monostatic SAR, the elevation antenna pattern is shaped to substantially attenuate echoes at angles that correspond to ambiguous ranges when the main beam is directed towards the scene of interest. This two-way attenuation of signals originating from sidelobe illumination yields a non-continuous illumination of the ground in the case of a burst-mode illumination. Figures 2.11 (a) and (c) represent signal acquired by a stationary ground-based receiving system. The one-way attenuation is clearly illustrated which yields gaps in the measurement during a ScanSAR illumination.

However, in a bistatic configuration with a receiver constantly pointing to the scene of interest, the returns originating from the elevation sidelobes of the transmit antenna may enter the mainlobe of the receiver with a sufficient SNR. The reason for this is twofold: on the one hand the transmit signal is only attenuated by the one-way transmit antenna gain pattern, and on the other hand, for a receiver close to the observed area, the patch-receiver distance is much smaller than the patch-transmitter distance of the monostatic case yielding a smaller free-space loss in the bistatic case. Note that, in contrast to monostatic SAR images, BSAR images are not only affected by the shadowing due to the look angle of the transmitter but also due to the look angle of the receiver. For a receiver close to the observed area, the obtained bistatic SAR image will be more affected by shadowing from the receiver than the monostatic image obtained from the same satellite due to the small grazing look angle of the receiver. This is evaluated for

different local terrain slopes in [108].

In a wide-swath mode, a ground patch in a specific sub-swath may be first illuminated by the mainlobe of the elevation beam of the transmit antenna corresponding to this sub-swath, then the antenna switches beam and this ground patch is then illuminated by the elevation sidelobe of the adjacent beam as illustrated in Fig. 5.1. If the SNR of the reflected signal received at the receiver is sufficient, this may result in a continuous illumination of the scene under the main beam of the receiver as illustrated in Fig. 2.11 (b) and (d) in the case of a ScanSAR mode.

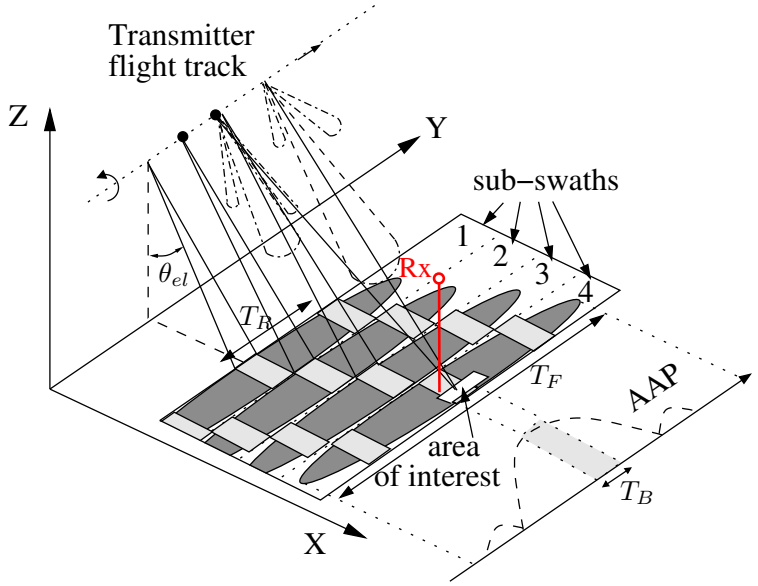

Figure 5.1: Acquisition geometry in ScanSAR imaging mode in the case of four sub-swaths. The receiver and the imaged area are located at the edge of the global swath (small rectangular area) and are illuminated by the sidelobes of the beam illuminating sub-swath 3 and afterwards, by the mainlobe of the beam illuminating sub-swath 4.

This continuous illumination of the scene of interest may be used to increase the integration time and thus improve the cross-range resolution compared to the traditional single-burst processing of ScanSAR data [77]. Although many bistatic configurations can be considered, the concept of improving the resolution of low-resolution mode makes sense when spaceborne emitters of opportunity are considered. Indeed, the imaging mode of spaceborne SAR instruments is most often a wide-swath mode [109]. Of course cooperative operation could be considered, such that the SAR system would operate in stripmap mode and thus would make high cross-range resolution possible.

That would however likely conflict with the needs of other users. The one-stationary configuration, where a spaceborne transmitter and a stationary receiver located on a hill or a high building are considered, is, in the author's opinion, one of the most practical configurations.

The following questions are now answered to support our motivation to exploit wide-swath illumination modes.

- Will the SAR image acquired in the space-ground bistatic geometry suffer from range ambiguities?
- How often is a continuous illumination achieved?

5.2 Range ambiguities

One question that arises is whether range ambiguities can occur in the considered bistatic geometry. As an example, the PRF of RADARSAT-2 in ScanSAR mode is of the order of 1300 Hz which corresponds to an ambiguous bistatic slant-range distance of 230 km. Considering the bistatic configuration of Fig. 5.1, the ambiguous bistatic slant-range distance corresponds as a first approximation to a slant-range distance of 115 km from the receiver. In order to receive the reflections from a patch located at this ambiguous distance, the receiver would need to be at an altitude of 990 m above sea level taking into account the curvature of the Earth. Either the receiver is at a lower altitude and no range ambiguities occur, or the receiver is at an altitude larger than 990 m and its elevation antenna pattern must be shaped such as to attenuate echoes from patches located at ambiguous ranges. Our bistatic receiver is located at an altitude of 100 m above sea level. Therefore, the SAR image will not be affected by range ambiguities.

5.3 Prediction of the resolution enhancement

5.3.1 Key parameter

The slow-time amplitude modulation of the measurements due to the elevation scanning of the transmit beam depends on the position of the imaged area in the global swath. This can be parametrised using the elevation angle denoted θ_{el} in Fig. 5.1. The slow-time amplitude modulation encountered by each patch can be deduced from the

elevation antenna diagram of the transmitter based on θ_{el}. Therefore, this key parameter can predict whether or not the potential wide-swath pass is suitable for cross-range resolution-enhanced SAR imaging.

5.3.2 Procedure

Based on the geometry of the satellite and the receiver, one can compute θ_{el} for each predicted overpass of the satellite. Then, based on the EAP of the non-cooperative transmitter, we can predict if there is sufficient SNR in the elevation sidelobes to be able to increase the integration time and thus increase the cross-range resolution. To that end, knowledge of the amplitude of the sidelobes of the elevation diagram of the transmit antenna is of utmost importance. As the satellite operator usually provides the two-way elevation diagram for 5° around the beam centre for each beam [44], we need to complement these diagrams at other angles with data acquired by the stationary ground-based receiver. We made the exercise for the ASAR instrument of ENVISAT as source [110], but the procedure can easily be extended to other transmitters.

The goal is to estimate the amplitude of each beam relative to the adjacent beams in order to extrapolate the EAP of the transmitter. In this exercise, the EAP of the receiver is known and constant during the signal acquisition and its AAP is known and assumed constant during the illumination time. As a non-cooperative transmitter is exploited, the AAP of the transmitter is unknown and is thus modelled in this work with a sinc function. A stripmap signal acquisition is used to extract the shape of the AAP of the transmitter. Once the parameters of the sinc model are known, the estimation of the beam-to-beam amplitude differences at different θ_{el} is performed by estimating the amplitude of the sinc model in the least square sense from the measurement data. For illustrative purpose, a ScanSAR mode signal acquisition in which the receiver and the imaged area are illuminated by all five beams is analysed. The elevation angle of the centre of the scene to be imaged is equal to 29.33°. The squared signal amplitude of the measurement is depicted in Fig. 5.2 (a). First, the different bursts of each beam are separated as depicted in Fig. 5.2 (b-f). The noise energy has been subtracted. The differences in energy inside a burst are possibly due to the fluctuation of the transmitted power [111]. Therefore, the mean energy inside a burst is computed and is represented by red dots in Fig. 5.2 (b-f). The amplitude of the AAP for each beam is then estimated

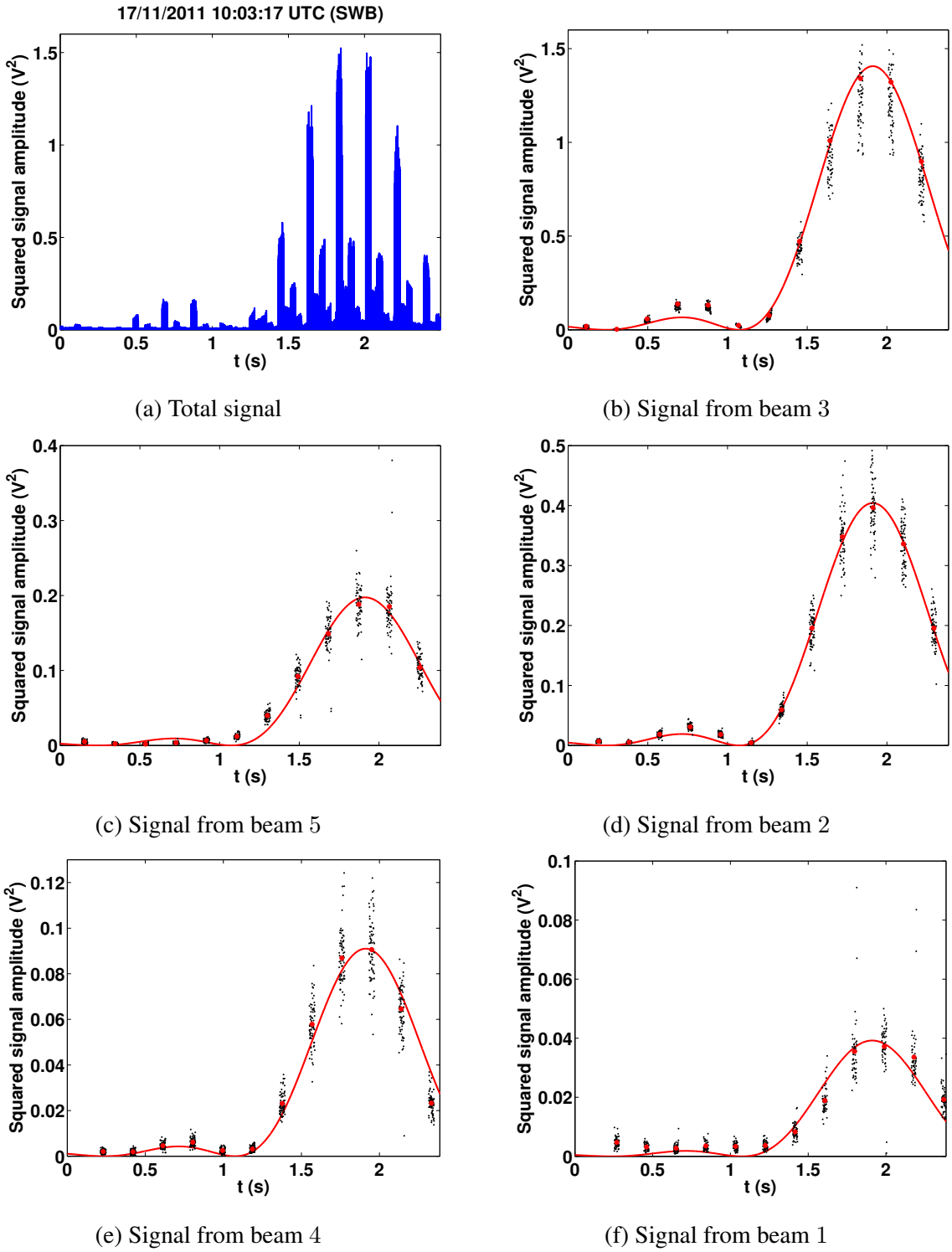

(a) Total signal

(b) Signal from beam 3

(c) Signal from beam 5

(d) Signal from beam 2

(e) Signal from beam 4

(f) Signal from beam 1

Figure 5.2: Squared signal amplitude of a RADARSAT-2 signal acquisition separated in beams.

in the least square sense from the measured mean energy of each burst. The result is illustrated in Fig. 5.3 and the estimated beam-to-beam amplitude differences correspond

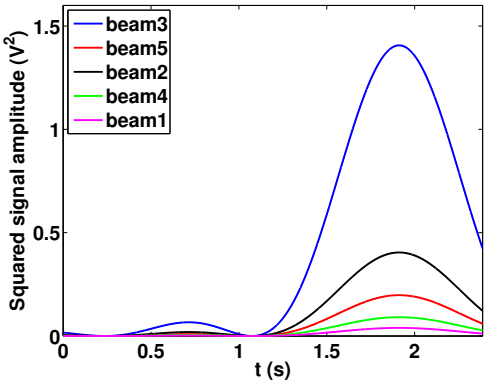

Figure 5.3: Fitted squared sinc model.

to one measurement used to extrapolate the elevation antenna pattern of the transmit antenna. The same procedure is followed for several acquisitions.

5.3.3 Result

Figure 5.4 depicts the ESA calibrated amplitude elevation diagrams of the five beams of ASAR used in ScanSAR mode (solid lines) and the extrapolation (dashed lines) based on our measurements (dots). Once the EAP have been extrapolated, the beam-to-

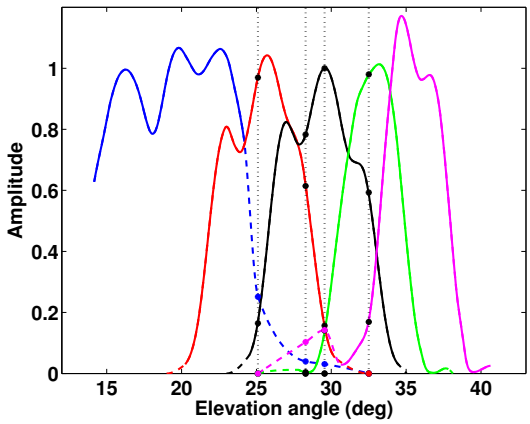

Figure 5.4: Extrapolated antenna elevation diagrams of the 5 beams of the ASAR antenna. The dots on the dashed line denote our measurements and the dots on the solid line denote the values obtained from sampling antenna patterns provided by ESA.

beam amplitude differences of each predicted overpass of the satellite can be extracted to predict whether or not the considered wide-swath pass is suitable for cross-range resolution-enhanced SAR imaging. During a period of six months (June-Dec 2011), about 25 ENVISAT passes were recorded over Brussels. The pie chart in Fig. 5.5 gives

the proportion of the different radar modes. It may be concluded that exploiting the multi-beam illumination passes increases of a factor 7 the number of passes suitable to produce high cross-range resolution images over the area of interest.

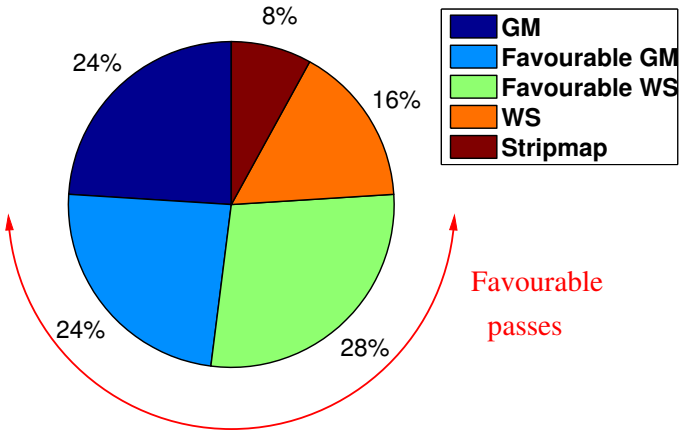

Figure 5.5: Six months measurement campaign result: half of the ScanSAR mode passes results in a continuous illumination.

For acquisitions in Fig. 2.11 (a) and (c), the geometry was such that the receiver was in the footprint of only one elevation beam of the ScanSAR mode. This case corresponds to $\theta_{el} = 15°$ in Fig. 5.4 and results in illumination gaps between two consecutive beam scans. When the imaged area of interest is ideally situated, i.e. at the centre of the global swath, reception of signals from all elevation beams is possible but each with a different amplitude according to the elevation antenna diagram of the considered beam. In this case, a continuous illumination occurs as depicted in Fig. 2.11 (b) and (d).

5.4 Conclusion

In the bistatic configuration studied in this thesis, range ambiguities will not degrade BSAR images thanks to the limited altitude of the receiver. It is also shown that thanks to the measurement of the EAP of the transmit antenna, it is possible to predict whether a future wide-swath pass of the satellite will present sufficient SNR in the elevation sidelobes to improve the cross-range resolution. As demonstrated for the ASAR instrument of ENVISAT, producing images with high cross-range resolution from data obtained from a SAR system operating in wide-swath mode substantially

increases the number of useful images that can be produced using emitters of opportunity since monostatic SAR systems usually transmit over land in wide-swath imaging mode. Since emitters of opportunity are considered, signals from any radar satellite in the receiving band of the receiver can be used, thus further decreasing the revisit time of the area of interest.

Chapter 6

SAR inverse problem

6.1 Introduction

SAR raw data may be considered as the result of the convolution of the observed scene reflectivity with the radar system response function. This is called the forward problem [43] and is described in Section 6.2. The image formation process can be regarded as an inverse problem which consists in inferring the observed scene reflectivity given the observed data and the forward model. The inverse problem of SAR imaging is ill-posed according to the classical definition of well-posedness [112] since a solution exists but is not unique; also, with the presence of noise, the solution is not stable. Therefore, a regularisation is necessary to turn the problem into a well-posed one and prevent the amplification of measurement noise during the reconstruction process. Although many regularisation methods exist [113], we will compare two methods. The first approach is the Maximum *a Posteriori* (MAP) estimate assuming a Gaussian model for the scene and the noise which is described in Section 6.3. Since the computational complexity of this method is high in the considered case of wide-swath illumination, we derive a novel method to focus SAR data in Section 6.3.2. The commonly used Matched Filter (MF) is also shown to be a particular case of the MAP SAR focussing. A second method to estimate the reflectivities is a sparse recovery method, better known as Compressive Sensing (CS) method which is proposed in Section 6.4. CS methods use the prior knowledge that the scene is sparse. The OMP greedy algorithm is chosen to illustrate the limitations of CS. Although many bistatic configurations can be considered, the bistatic space-ground configuration of the experiments can be kept in mind but the method and the developments that follow are generic.

6.2 SAR signal model

We consider here the unidimensional case for simplicity and K ground patches along a bistatic isorange contour. If Range Cell Migration (RCM) is neglected, the measured range-compressed data corresponding to the considered range bin can be written as a column vector, $\mathbf{y^k} \in \mathbb{C}^{\mathbf{M\times 1}}$, with M being the number of transmitted pulses. The received data due to the k^{th} ground patch can be modelled as

$$\mathbf{y^k} = \mathbf{W h^k} x^k + \mathbf{n} \tag{6.1}$$

where x^k is the complex reflectivity of the k^{th} ground patch and $\mathbf{n} \in \mathbb{C}^{M\times 1}$ denotes the thermal noise. The column vector $\mathbf{h^k} \in \mathbb{C}^{M\times 1}$ represents a received signal if a scatterer at patch k has a reflectivity of 1 and includes the AAP weighting of the transmit and the receive antennas. This AAP weighting depends on the location of the target in the observed area. In addition to the AAP weighting embedded in $\mathbf{h^k}$, the received signals undergo a slow-time amplitude modulation represented by $\mathbf{W} = diag(\mathbf{w})$ with $\mathbf{w} \in \mathbb{R}^{M\times 1}$. This modulation function is determined, for each beam, by the corresponding elevation antenna gain at the elevation angle at which the scatterer is located. The model (6.1) assumes an invariant $\mathbf{W}$ along the considered bistatic isorange contour. The validity of this assumption will limit the size of the area that can be imaged according to its position with respect to the transmitter and the receiver. $\mathbf{W}$ depends on the elevation angle under which the patches are illuminated by the transmitter. Thus, if the transmitter flies along a straight path, the patches located along a line parallel to the transmitter flight path will be subject to the same $\mathbf{W}$. In the case of the ASAR antenna of ENVISAT, and if a difference of 0.25 dB in $\mathbf{W}$, which corresponds to the specified one-way antenna calibration error [114], is accepted, the bistatic isorange contour may deviate from the above-mentioned straight line by up to 20 km. Thus, the imaging area must be such that the bistatic isorange contour deviates by less than 20 km from a straight line parallel to the flight path.

The total received signal seen by the radar is then the sum of the responses from all ground patches along one isorange contour and can be modelled as

$$\mathbf{y} = \mathbf{WHx} + \mathbf{n} = \mathbf{H_w x} + \mathbf{n} \tag{6.2}$$

with $\mathbf{x} = [x^0, x^1, ..., x^k, ..., x^{K-1}]^T$, $\mathbf{H} = [\mathbf{h^0}, \mathbf{h^1}, ..., \mathbf{h^k}, ..., \mathbf{h^{K-1}}]$ and K the number of ground patches along the considered bistatic isorange contour.

The slow-time modulation $\mathbf{W}$ depends on the radar mode in which the transmitter is operating. For the stripmap mode, $\mathbf{W}$ is obviously constant. However, wide-swath mode illuminations (TOPSAR, ScanSAR) of the scene of interest are responsible for an amplitude modulation of the SAR phase history.

The SAR inverse problem consists in the reconstruction of the target reflectivity function $\mathbf{x}$ from the measurements $\mathbf{y}$, i.e. finding the operator $\mathbf{F}$ such that

$$\hat{\mathbf{x}} = \mathbf{F}(\mathbf{y}) \tag{6.3}$$

with $\hat{\mathbf{x}}$ the estimated scene reflectivity.

6.3 Maximum *a posteriori* image formation

6.3.1 Optimum SAR focussing

The unknown reflectivity vector $\mathbf{x}$ can be estimated by maximising its *a posteriori* Probability Density Function (PDF) or

$$\hat{\mathbf{x}} = \arg\max_{\mathbf{x}} p(\mathbf{x}|\mathbf{y}). \tag{6.4}$$

which can be reformulated with the Bayes identity

$$\hat{\mathbf{x}} = \arg\max_{\mathbf{x}} \frac{p(\mathbf{y}|\mathbf{x})p(\mathbf{x})}{p(\mathbf{y})}. \tag{6.5}$$

The *a priori* probability, $p(\mathbf{y})$, does not depend on $\mathbf{x}$ and thus, does not influence the position of the maximum. In this work, *a priori* knowledge about $\mathbf{x}$ is introduced making (6.4) the MAP estimate of $\mathbf{x}$.

Let us assume that the reflectivity $\mathbf{x}$ is complex Gaussian distributed which is the statistical model of fully developed speckle [43]. This means that the *a priori* PDF of the scene reflectivity $\mathbf{x}$ is completely specified in terms of its covariance matrix $\mathbf{R_x} = E[\mathbf{x}\mathbf{x}^\dagger]$, i.e.

$$p(\mathbf{x}) \propto e^{-\mathbf{x}^\dagger {\mathbf{R_x}}^{-1}\mathbf{x}} \tag{6.6}$$

As $\mathbf{n} = \mathbf{y} - \mathbf{H_w}\mathbf{x}$ from (6.2) and assuming a Gaussian noise, the likelihood function can be written

$$p(\mathbf{y}|\mathbf{x}) = p(\mathbf{n}) \propto e^{-(\mathbf{y}-\mathbf{H_w}\mathbf{x})^\dagger {\mathbf{R_n}}^{-1}(\mathbf{y}-\mathbf{H_w}\mathbf{x})}. \tag{6.7}$$

Then, the *a posteriori* PDF of $\mathbf{x}$ becomes

$$p(\mathbf{x}|\mathbf{y}) \propto e^{-(\mathbf{y}-\mathbf{H_w}\mathbf{x})^\dagger {\mathbf{R_n}}^{-1}(\mathbf{y}-\mathbf{H_w}\mathbf{x})} e^{-\mathbf{x}^\dagger {\mathbf{R_x}}^{-1}\mathbf{x}} \tag{6.8}$$

the maximum of which is reached [115] for

$$\hat{\mathbf{x}} = \mathbf{H}_{\mathbf{r}}^{\dagger}\mathbf{y} \tag{6.9}$$

with

$$\mathbf{H}_{\mathbf{r}}^{\dagger} = \mathbf{R}_{\mathbf{x}}\mathbf{H}_{\mathbf{w}}^{\dagger}(\mathbf{H}_{\mathbf{w}}\mathbf{R}_{\mathbf{x}}\mathbf{H}_{\mathbf{w}}^{\dagger} + \mathbf{R}_{\mathbf{n}})^{-1} \tag{6.10}$$

where $\mathbf{R}_{\mathbf{n}} = E[\mathbf{n}\mathbf{n}^{\dagger}]$ is the covariance matrix of the noise $\mathbf{n}$. The solution (6.9) provides the best estimate in a MAP sense to the scene reflectivity $\mathbf{x}$ given the measurements $\mathbf{y}$ assuming a Gaussian prior PDF and Gaussian noise. The optimal SAR focussing thus consists of the multiplication of the reconstruction matrix $\mathbf{H}_{\mathbf{r}}^{\dagger}$ with the measurements $\mathbf{y}$. The matrix $\mathbf{H}_{\mathbf{r}}^{\dagger}$ is the well-known Wiener filter [36, 113]. Note that the MAP estimator (6.10) is identical to the Minimum Mean Square Error (MMSE) estimator [36, 116] in the Gaussian signal model.

The computation of (6.10) is feasible in the classical single-burst processing [76], in which a few dozen pulses are processed. In a continuous illumination, more than one thousand pulses must be processed. Therefore, in a continuous illumination case, (6.10) is computationally demanding and possibly unfeasible. Another implementation is now discussed making additional assumptions.

6.3.2 Burst-mode resolution enhancement method

If $\mathbf{x}$ and $\mathbf{n}$ are samples of Gaussian stationary processes and the elements of the vectors $\mathbf{x}$ and $\mathbf{n}$ are assumed uncorrelated, then the covariance matrices become $\mathbf{R}_{\mathbf{x}} = \sigma_x^2\mathbf{I}$ and $\mathbf{R}_{\mathbf{n}} = \sigma_n^2\mathbf{I}$ with σ_x^2 and σ_n^2 respectively the variance of the scene reflectivity and of the noise and $\mathbf{I}$ the identity matrix. The optimum focussing (6.10) simplifies thus as

$$\begin{aligned} \mathbf{H}_{\mathbf{r}}^{\dagger} &= \mathbf{H}_{\mathbf{w}}^{\dagger}(\mathbf{H}_{\mathbf{w}}\mathbf{H}_{\mathbf{w}}^{\dagger} + \vartheta\mathbf{I})^{-1} \\ &= \mathbf{H}^{\dagger}[\mathbf{W}^{\dagger}(\mathbf{W}\mathbf{H}\mathbf{H}^{\dagger}\mathbf{W}^{\dagger} + \vartheta\mathbf{I})^{-1}] \end{aligned} \tag{6.11}$$

where $\vartheta = \frac{\sigma_n^2}{\sigma_x^2}$ is the inverse of the SNR.

If the conditions to have $\mathbf{H}\mathbf{H}^{\dagger}$ diagonal are met, the matrix operation in brackets in (6.11) is simply a multiplication between diagonal matrices which leads to

$$\mathbf{H}_{\mathbf{r}}^{\dagger} = \mathbf{H}^{\dagger}\mathbf{C}_{\mathbf{w}} \tag{6.12}$$

where the matrix $\mathbf{C}_{\mathbf{w}}$ is a diagonal matrix with the diagonal elements equal to

$$c_{w,i}(\vartheta) = \frac{w_i}{w_i^2 K + \vartheta} \tag{6.13}$$

with w_i the i^{th} element of $\mathbf{w}$. This matrix acts as a compensation of the slow-time modulation embodied by $\mathbf{w}$, or in another words, restore the performance degraded by the multiplication by $\mathbf{W}$ in (6.2). This equation holds if the Gram matrix $\mathbf{H}\mathbf{H}^\dagger$ is diagonal which is achieved if the ground patches are resolved.

Finally, the optimum SAR focussing (6.9) simplifies in

$$\hat{\mathbf{x}} = \mathbf{H}^\dagger \mathbf{C}_\mathbf{w} \mathbf{y} \tag{6.14}$$

This result implies that the burst-mode resolution enhancement method consists in

- compensating in the measurement domain, the slow-time modulation of the measurements induced by the beam scanning in elevation

$$\mathbf{y_c} = \mathbf{C_w} \mathbf{y} \tag{6.15}$$

- focussing using the conventional Matched Filter (MF)

$$\hat{\mathbf{x}} = \mathbf{H}^\dagger \mathbf{y_c}. \tag{6.16}$$

Note that in the case of a uniform illumination, i.e. $\mathbf{W} = \mathbf{I}$, and if the SNR is very large, (6.12) boils down to the conventional MF,

$$\mathbf{H}_\mathbf{r}^\dagger \propto \mathbf{H}^\dagger \tag{6.17}$$

In this work, the Back-Projection (BP) algorithm [67, 74, 75] to implement the MF (6.16) after the cross-range compensation step (6.15) is used.

6.3.3 Achievable performance

6.3.3.1 ScanSAR illumination

To illustrate the expected performance of the method in the case of a ScanSAR illumination, the measurement resulting from a stripmap acquisition have been modulated by the slow-time modulation of a ScanSAR acquisition. A point scatterer in the presence of noise with a SNR of -10 dB before any coherent processing is simulated and two extreme situations are envisaged. First, a single-beam ScanSAR illumination, as would be obtained for a scatterer at the very edge of the wide swath is considered. This geometry would result in a pulse-train window modulation $\mathbf{w}$ as illustrated in Fig. 6.1 (a).

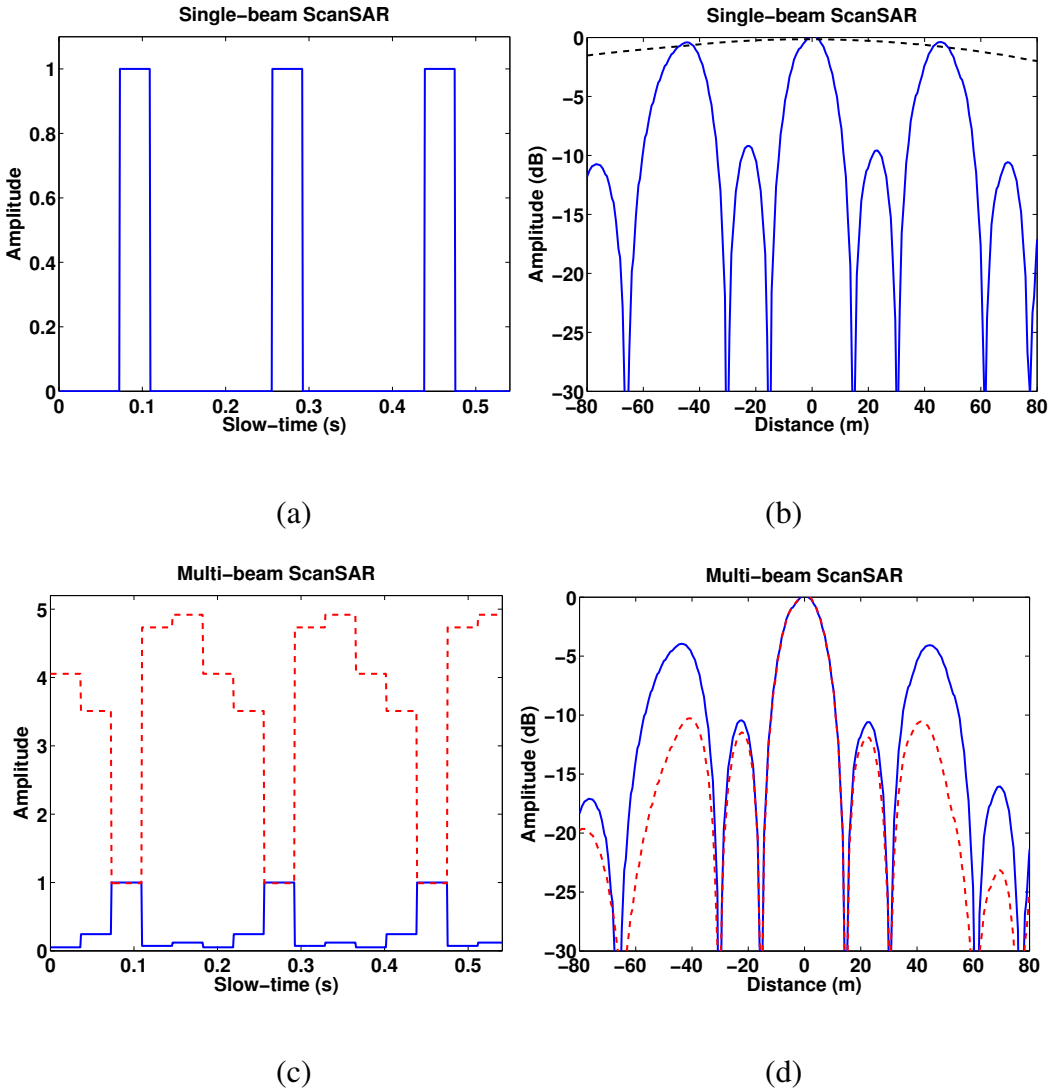

Figure 6.1: On the left, the normalised slow-time amplitude modulation w of (a) a single-beam and (c) a multi-beam ScanSAR illumination, and on the right, cuts of the IRF along the scatterer's isorange for (b) a single-beam and (d) a multi-beam ScanSAR illumination.

Figure 6.1 (b) represents the intensity of the azimuthal Impulse Response Function (IRF) obtained if one single burst is focussed (dashed line) [77] and if all bursts are coherently processed (solid line) using a conventional MF. The latter drastically improves the poor resolution of the single-burst processing but grating lobes along the azimuth direction appear.

When the scatterer is ideally situated, i.e. at the centre of the global swath, reception of signals from all five elevation beams is possible but each with a different amplitude according to the elevation antenna diagram of the considered beam as illus-

trated in Fig. 6.1 (c) (solid line). In this case, the area of interest is illuminated by the elevation sidelobes of the transmit antenna leading to a reduction of the amplitude of the azimuth grating lobes in the IRF as illustrated in Fig. 6.1 (d) (solid line). The Peak-to-Side Lobe Ratio (PSLR) improved from 0.5 dB for a single-beam illumination to 4 dB for a multi-beam illumination. That demonstrates that exploiting the signals originating from the elevation sidelobes of the transmit antenna is a step in the right direction to approach the stripmap performance.

By applying the burst-mode resolution enhancement method (6.14), the residual grating lobes due to the ScanSAR data are attenuated by about 8 dB which puts it at the same level as the other sidelobes as illustrated in Fig. 6.1 (d) (dashed line). That will be the case if the SNR of the backscattered signals coming from the patches illuminated by the elevation sidelobes of the transmit antenna is sufficient. The applied cross-range compensation function $\mathbf{c_w}$ is depicted in Fig. 6.1 (c) (dashed line). It is obvious that the product $c_{w,i}w_i$ for $i = 0 \dots M-1$ must converge to 1 to approach the PSLR of the stripmap mode. As is evident from (6.13), this will happen for very small ϑ, i.e. very large SNR.

It is important to stress that the grating lobes pattern in the azimuthal IRF depends on the number of sub-swaths, N_S, and on the number of looks, N_L, of the ScanSAR mode. ScanSAR modes designed with $N_L > 1$ as is the case for the wide-swath modes of ENVISAT or RADARSAT-2 [117] can give rise to grating lobes in the azimuthal IRF if more than one burst are coherently focussed. The distance between the mainlobe of the IRF and the first grating lobe is inversely proportional to $N_S B_a$ with B_a the azimuthal burst bandwidth [78].

6.3.3.2 TOPSAR illumination

The TOPSAR mode implemented on Sentinel-1A [109] is a one-look wide-swath mode. In this wide-swath mode, the azimuthal IRF is not corrupted by grating lobes but has a higher sidelobe level [118] when focussed without using the burst-mode resolution enhancement method.

To give a quantitative insight of the performance of the method in a TOPSAR illumination, a scenario with a point scatterer in presence of noise is simulated. A SNR of 20 dB after focussing is chosen. The simulated slow-time modulation is based on

the measured Sentinel-1A signal envelope of Fig. 6.2.

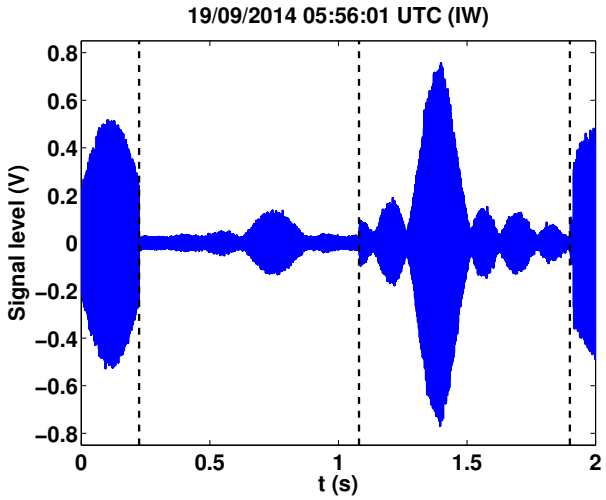

Figure 6.2: Acquired Sentinel-1A signal in TOPSAR.

Two extreme cases have been considered. First, a single-beam illumination with a typical burst duration T_B of 0.8 s (IW mode), as would be obtained for a receiver/scatterer at the very edge of the global swath, would result in a sinc-shaped azimuth modulation like the portion of the envelope of the signal between 1.08 s and 1.9 s in Fig. 6.2. Figure 6.3 (a) shows cuts of the IRF along the bistatic isorange contour computed using the MF (dashed line) and the burst-mode resolution enhancement method (solid line). The slow-time modulation results in a high level of sidelobe in the case of the MF. However, the burst-mode resolution enhancement method considerably decreases the level of azimuth sidelobes in the IRF.

Secondly, if the receiver/scatterer are located in the centre of the global swath, a multi-beam illumination occurs with a slow-time modulation equals to the entire slow-time envelope of Fig. 6.2. The corresponding cuts of the IRF along the bistatic isorange contour are illustrated in Fig. 6.3 (b) and as expected [3], an improved cross-range resolution results in the case of a multi-beam illumination. If the cross-range compensation function (6.15) is applied, the cross-range resolution is kept while the sidelobe levels considerably decrease as illustrated in Fig. 6.3 (b) (solid line).

6.3.4 Evaluation of the noise amplification

One drawback of the burst-mode resolution enhancement method is the increase of the noise content in the SAR image. In this section, the impact of the noise amplification

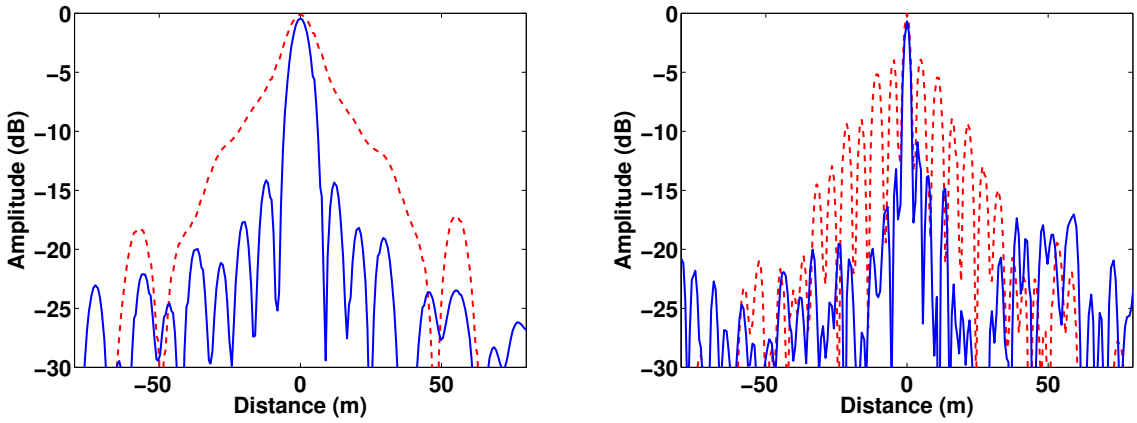

(a) Single-beam illumination

(b) Multi-beam illumination

Figure 6.3: IRF cuts along the scatterer's isorange using the conventional MF (dashed line) and the burst-mode resolution enhancement method (solid line) ($SNR = 20$ dB after focussing).

of the novel burst-mode resolution enhancement method is evaluated using simulated data.

6.3.4.1 Noise amplification factor

To evaluate the noise amplification for different bistatic geometries, we use the extrapolated EAP of ENVISAT (Fig. 5.4) and simulate the respective slow-time amplitude modulation that the measured data would encounter. This is performed for satellite passes over $15° \leq \theta_{el} \leq 40°$. Figure 6.4 (a) shows the computed PSLRs of the IRF for each geometry obtained with the conventional MF (dashed line) and with the conventional MF preceded by the cross-range compensation (6.14) (solid line). For $27° \leq \theta_{el} \leq 32°$, the PSLR of the MF output with the cross-range compensation step (6.14) is by far better than without. For those geometries with small ϑ, $c_{w,i}$ tends to the inverse of w_i, compensating appropriately the slow-time modulation, i.e. leading to a reduction of the grating lobes, but, at the same time, will amplify the noise included in the measured data. Outside that angular range, one or several beams are barely present leading to a poor signal amplitude over part of the aperture (large ϑ). In those cases, $c_{w,i}$ will neither amplify the signal nor the noise: the poor SNR will not degrade but the grating lobes will remain. The noise amplification induced by the method can be

quantified using

$$F_w = 10\, log_{10}\left(\frac{1}{M}\sum_{i=0}^{M-1}|c_{w,i}|^2\right). \tag{6.18}$$

This parameter, depicted in Fig. 6.4 (b), represents the factor by which the noise variance is amplified relative to the constant $\mathbf{W}$ case. The reduction of the grating lobes is accompanied by a noise amplification by up to 15 dB.

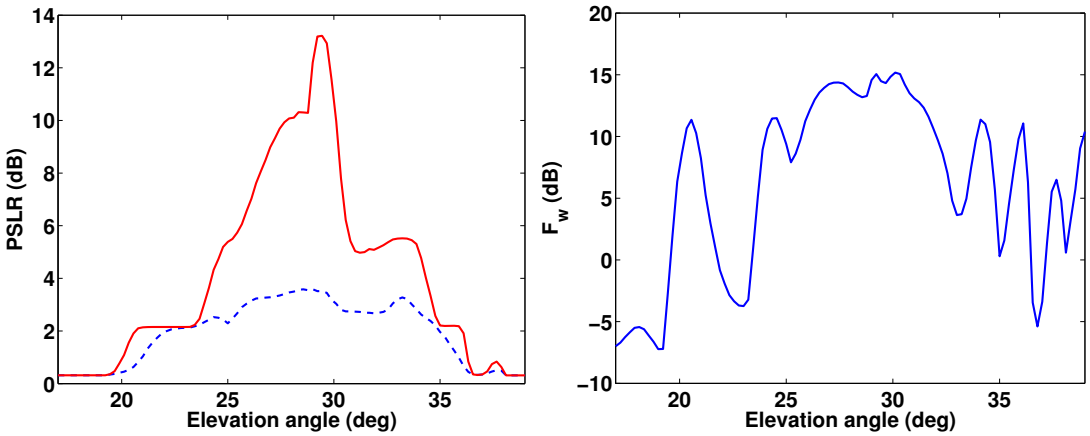

(a) (b)

Figure 6.4: (a) Calculated PSLR for different antenna elevation angles without (dashed line) and with the cross-range compensation function (solid line) and (b) calculated relative noise energy (w.r.t. stripmap mode) amplification F_w due to the compensation step.

6.3.4.2 Mean Square Error

Another way to measure the noise amplification induced by the method is by computing the Mean Square Error (MSE) between the true one-dimensional IRF profile (along the azimuth direction) and its reconstructed version. This is illustrated considering a multi-beam TOPSAR illumination with a slow-time modulation equals to the entire slow-time envelope of Fig. 6.2. The MSE is computed for increasing SNRs and considering a Monte Carlo method (100 realisations). Figure 6.5 depicts the mean MSE with error bars representing one standard deviation on either side of the mean. For the conventional MF focussing (dashed line), the mean MSE is approximately constant for large SNRs while it decreases for increasing SNRs if the cross-range compensation is applied. The mean MSE of the IRF of Fig. 6.3 (b) (SNR$=20$ dB) is equal to 0.088 for

the conventional MF and to 0.037 for the burst-mode resolution enhancement method. One can see that the burst-mode resolution enhancement method based on MMSE estimator outperforms the conventional MF as expected.

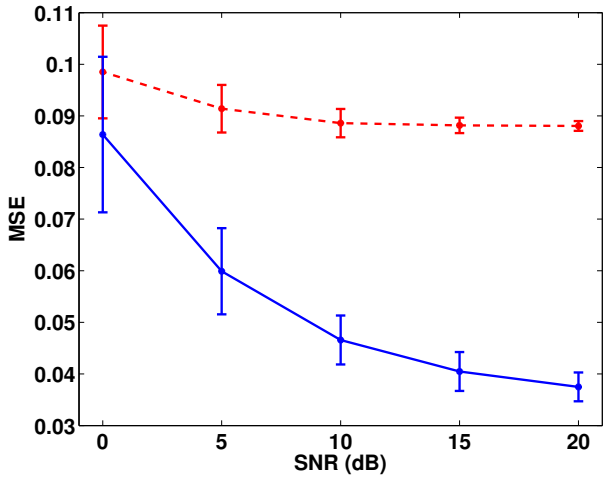

Figure 6.5: Mean value of the MSE as a function of the SNR (after focussing) using the MF (dashed line) and the burst-mode resolution enhancement method (solid line).

6.3.4.3 Coherence

Taking interferometry as a possible application, the noise amplification induced by the burst-mode resolution enhancement method can lead to a partial decorrelation of the two images which introduces noise in the interferogram and corrupts the estimation of the interferometric phase. This raises the question of how far the phase noise level can increase before a significant loss of coherence. To answer the question, single-pass interferometry using two different channels of the ground-based receiver is considered. This choice allows us to concentrate on the study of the phase noise generated by the method as the phase noise due to temporal change of the scene vanishes while the small spatial baseline minimises baseline decorrelation. Note that the actual baseline of the receiving system is half a wavelength. Such short baseline is required for short stand-off range in order to have an acceptable sensitivity to topography (across-track interferometry) or to movement (along-track interferometry).

The coherence parameter refers to the amplitude of the complex correlation coefficient between two SAR images. Given the SAR images z_1 and z_2, the complex

correlation coefficient is defined as [119]

$$\Delta = \frac{E[z_1 z_2^*]}{\sqrt{E[|z_1|^2]}\sqrt{E[|z_2|^2]}} \tag{6.19}$$

where * refers to the complex conjugation. In practice, Δ can be estimated from (6.20) by substituting the ensemble averages with spatial sample averages (i.e. by assuming process ergodicity in a small estimation area of L pixels). Thus, the sample coherence δ is

$$\delta = \frac{\Sigma_{i=1}^{L} z_{1i} z_{2i}^*}{\sqrt{\Sigma_{i=1}^{L}|z_{1i}|^2}\sqrt{\Sigma_{i=1}^{L}|z_{2i}|^2}} \tag{6.20}$$

with L the number of pixels used to estimate the coherence. A high coherence level (close to 1) indicates a very good phase correlation between the two images.

To illustrate what is expected from the measurements, a point scatterer with a SNR of -10 dB (before coherent processing) is simulated. A favourable geometry is considered which means that the amplitude of the signals transmitted in the elevation sidelobes is sufficient. The right hand images of Fig. 6.6 depict the sample coherence image between the SAR images obtained from two channels with a horizontal baseline of half a wavelength, one of whom is represented on the left side. Figure 6.6 (a) shows the simulated Single-Look Complex (SLC) SAR image centred on the point scatterer obtained with the conventional MF. The expected grating lobes in azimuth along the isorange can be observed. A high coherence between two channels (Fig. 6.6 (b)) results as the interferometric baseline between the channels is quite small.

If the burst-mode resolution enhancement method is applied with the correctly-estimated value of ϑ, there is a trade-off between the amplification of the noise and the reduction of the grating lobes. The latter are reduced but still present in Fig. 6.6 (c). Here, the coherence depicted in Fig. 6.6 (d) remains high while the noise amplification due to the burst-mode resolution enhancement method is small. For an overestimated SNR (too small ϑ), the cross-range compensation function $\mathbf{c_w}$ becomes the inverse of $\mathbf{w}$: the amplitude modulation in azimuth is compensated at the expense of an increase of the noise content in the SAR image (Fig. 6.6 (e)). This amplification of the noise leads to a coherence loss between the two SAR images as depicted on the coherence image in Fig. 6.6 (f).

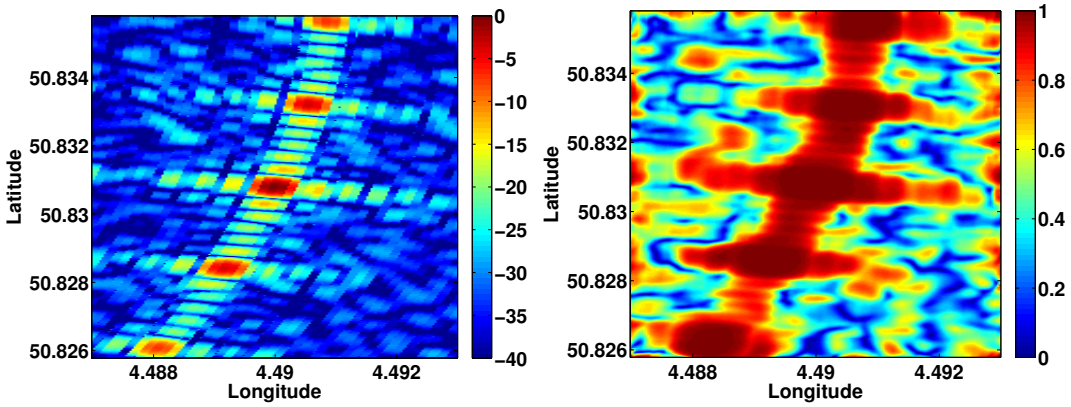

(a) (b)

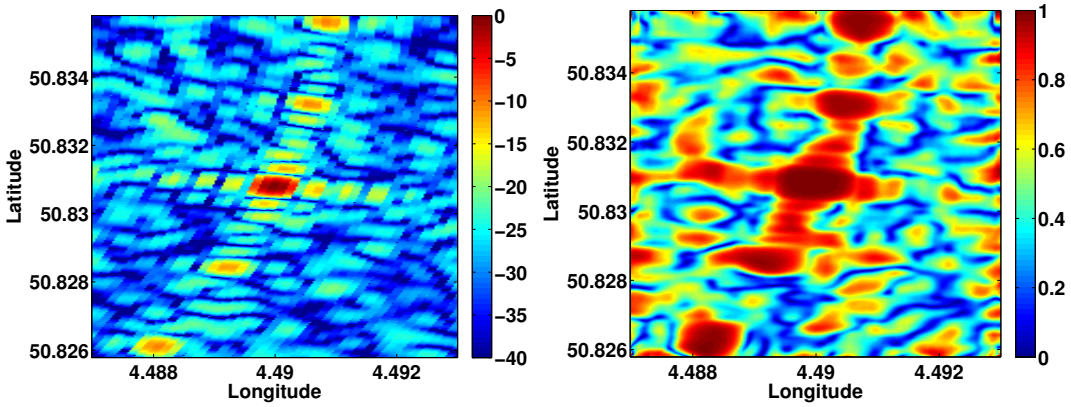

(c) (d)

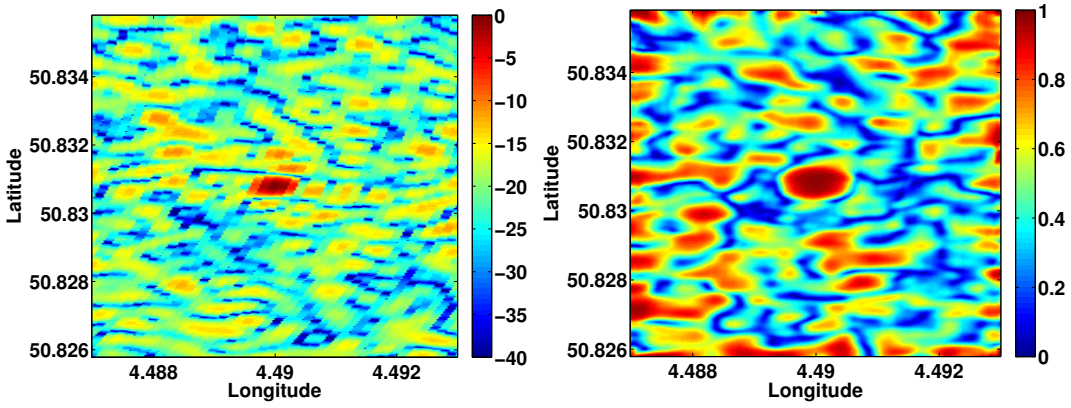

(e) (f)

Figure 6.6: On the right side, sample coherence image between the simulated SAR images obtained from two horizontally-spaced channels, one of whom is represented on the left side. The first rows obtained with the conventional MF (a, b), the second row with the optimum cross-range compensation function (c, d) and the third row with a sub-optimal cross-range compensation function (inverse filter) (e, f).

6.4 Sparsity-driven image formation

6.4.1 SAR focussing using sparse recovery methods

The aforementioned SAR model (6.2) can be regarded as a linear combination of basis functions embedded in the matrix $\mathbf{H_w}$. We shall refer to $\mathbf{H_w}$ as a dictionary and its columns as atoms [120]. Each column of the matrix $\mathbf{H_w}$ represents the phase history for a given point in the discretised scene.

In sparse recovery methods or Compressive Sensing (CS) [121], the ill-posed inverse problem is regularised assuming that the unknown signal $\mathbf{x}$ is S-sparse (i.e. has at most S non-zero entries). The objective of sparse recovery is to find the sparsest vector $\mathbf{x}$, represented as:

$$\min_{\mathbf{x}} \quad \|\mathbf{x}\|_0 \quad \text{subject to} \quad \mathbf{y} = \mathbf{H_w}\mathbf{x} \tag{6.21}$$

where $\|\cdot\|_0$ denotes the l_0-norm and represents the number of non-zero elements. Unfortunately, the l_0-norm is a non-convex function making (6.21) computationally difficult to solve due to the required combinatorial exploration of all subsets of $\mathbf{H_w}$.

It is possible to recover exactly the sparse signal $\mathbf{x}$ via a sparse recovery method when the matrix $\mathbf{H_w}$ has the Restricted Isometry Property (RIP) of order S. The RIP requires [122] that

$$(1 - \delta_k) \|\mathbf{x}\|_2^2 \leq \|\mathbf{H_w}\mathbf{x}\|_2^2 \leq (1 + \delta_k) \|\mathbf{x}\|_2^2 \tag{6.22}$$

where $\|\cdot\|_2$ is the Frobenius norm or the l_2-norm, $\mathbf{x}$ is any vector having S non-zero coefficients, and $\delta_k \in (0, 1)$. The smaller the value δ_k is, the better the sparse signal can be reconstructed.

If the RIP holds, replacing the l_0-norm by the l_1-norm has been shown [123–125] to lead to the same solution with overwhelming probability. The relaxed version of the problem then takes the form

$$\min_{\mathbf{x}} \quad \|\mathbf{x}\|_1 \quad \text{subject to} \quad \mathbf{y} = \mathbf{H_w}\mathbf{x} \tag{6.23}$$

which is essentially a linear program and thus can be resolved by any algorithm from the Linear Programming (LP) literature [126]. This problem is known in the literature as basis pursuit [125].

l_1-norm minimisation is not the only way to approximate sparse solutions. Heuristic greedy algorithms [127] have been developed to approximate (6.23), which are also

significantly faster than using LP. In this work, we focus on Orthogonal Matching Pursuit (OMP) which selects one atom at a time, iteratively.

6.4.2 Applicability of sparse recovery methods in BSAR

This section analyses the two fundamental premises underlying sparse recovery methods which are the sparsity of the signal to be recovered and the incoherence of the dictionary.

6.4.2.1 Sparsity

CS assumes that the signal to be recovered, i.e. the SAR image $\mathbf{x}$, is sparse in a specific dictionary which is $\mathbf{H_w}$ in this work. Radar scenes with highly reflective objects can be considered as sparse in the dictionary $\mathbf{H_w}$. The man-made structures have bright reflectivity and this dictionary is then adequate for urban areas. The sparsity of monostatic radar data has been already justified in the literature [128]. In bistatic radar, one can also find point scatterers but probably at other positions than in the monostatic case due to differences in scattering mechanisms between bistatic and monostatic SAR [14, 15].

6.4.2.2 Incoherent dictionary

In addition to the sparsity, another essential condition of CS is the incoherence of the dictionary. The incoherence of a dictionary can be verified using the RIP or by computing the mutual coherence. RIP requires that all possible combinations of S non-zero entries of vector $\mathbf{x}$ have to satisfy (6.22), which is a NP-complete problem and thus difficult to verify. However, it can be shown [129] that the mutual coherence is also a good parameter to measure the incoherence of a dictionary. Dictionaries which are maximally incoherent will satisfy this restricted isometry property. The mutual coherence of the sensing matrix $\mathbf{H_w}$ is the largest absolute and normalised inner product between its atoms

$$\mu(\mathbf{H_w}) = \max_{i \neq j} \frac{|\mathbf{h_w}_i^{\dagger} \mathbf{h_w}_j|}{\|\mathbf{h_w}_i\|_2 \left\|\mathbf{h_w}_j\right\|_2} \tag{6.24}$$

where $\mathbf{h_w}_i$ is the i^{th} column of the matrix $\mathbf{H_w}$. In other words, the mutual coherence is the largest off-diagonal entry of the column normalised matrix product $\mathbf{H_w}^{\dagger}\mathbf{H_w}$. Large mutual coherence indicates a presence of two very similar columns that may confuse the reconstruction algorithm. The incoherence of $\mathbf{H_w}$ strongly depends on the modulation pattern $\mathbf{W}$. In the extreme case where there are gaps in the phase

history, i.e. $\mathbf{W}$ has diagonal elements equal to zero, it has been demonstrated that the more random the gap pattern [123], the more incoherent the matrix $\mathbf{H_w}$. The mutual coherence can take value between 0 and 1. In the case where $\mu(\mathbf{H_w}) = 1$, it is obvious that there is no unique sparsest solution to (6.2).

While in most applications of CS, measurements are dropped in a way to satisfy the incoherence property, all our available measurements are used. In the case of ScanSAR illumination, the gap pattern can be periodic as illustrated in the upper part of Fig. 6.7 (b). The mutual coherence of the corresponding dictionary is illustrated in the lower part of Fig. 6.7 (b). As shown, off-diagonal elements are present but are smaller than 1, it is then verified that $\mathbf{H_w}$ satisfies RIP. Note that the finer the grid of the scene, the stronger is the correlation between atoms which then reduces the performance of CS algorithms.

6.4.3 Greedy approach

6.4.3.1 Orthogonal Matching Pursuit

One of the simplest greedy algorithms is Matching Pursuit (MP), which Mallat and Zhang introduced to the signal processing community [120]. MP decomposes the unknown signal to be recovered into the contributions of several atoms selected from a dictionary. The first iteration consists of the projection of the measurement data on the dictionary which is equivalent to compute the matched filter output. Then MP detects the predominant value of the matched-filter output and rejects its contribution with its associated sidelobes. This most correlated atom is added to the set of selected atoms. The residual signal is then projected on the dictionary and the MP continues to update the set of selected atoms with the most correlated projection until a stop criteria is met.

Note that the vector selected at each step by MP is not necessarily orthogonal to the previously selected vector. The subtraction of the projection reintroduces new components, which slow down the convergence of the algorithm and introduce false targets. This can be avoided by projecting the residual signal on an orthogonal family as in the Orthogonal Matching Pursuit (OMP) method. OMP, which was first proposed in the signal processing literature in [130], adds a least-squares minimisation at each step to obtain the best approximation of the signal over the atoms which have already been chosen. Therefore, the residuals after each step in the OMP algorithm are orthogonal

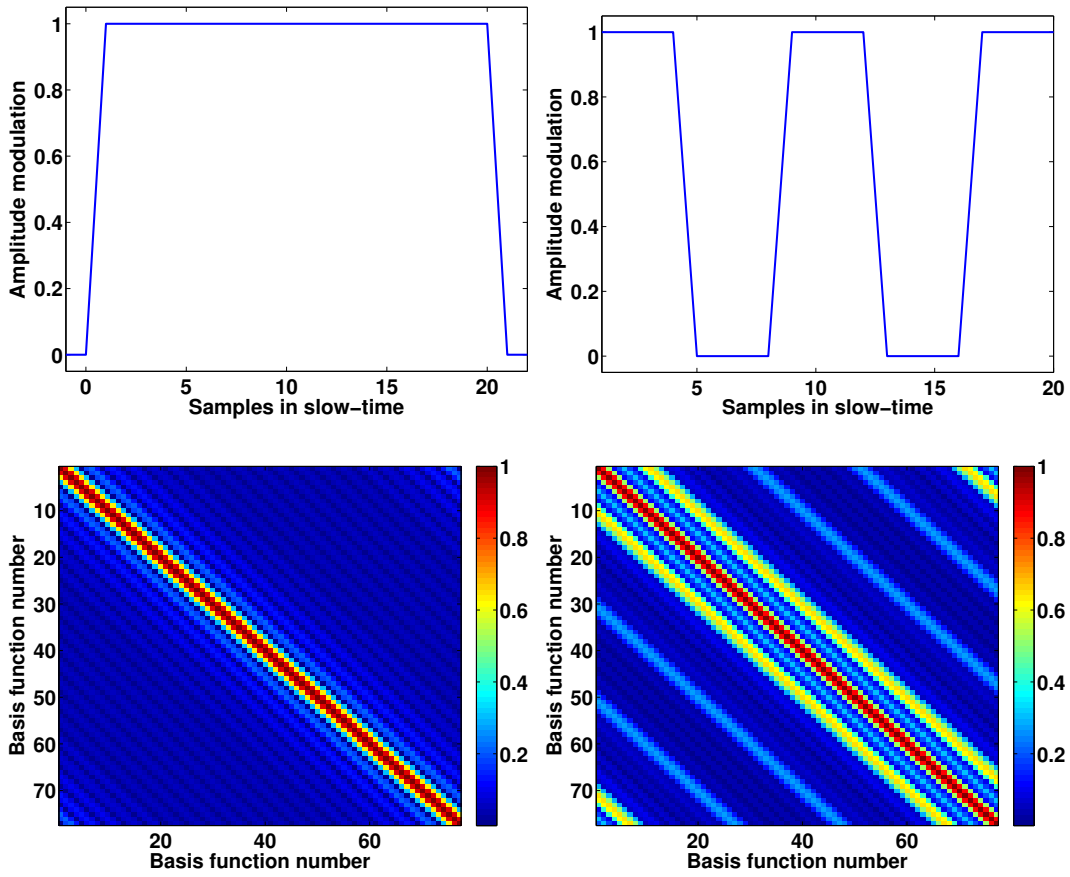

(a) (b)

Figure 6.7: Illustration of the mutual coherence of the dictionary $\mathbf{H}_{\mathrm{w}}$ in the case of (a) uniform illumination such as stripmap and (b) non-uniform illumination such as ScanSAR.

to all the selected columns of $\mathbf{H}_{\mathrm{w}}$, so no column is selected twice. This revision of MP significantly improves the rate of convergence. Several implementations of OMP exist [131]. Our OMP implementation is based on [130] where the projections are not computed at each iteration but the previous coefficients of the projection are iteratively updated with a simple updating formula. In the noiseless case and if the signal is S-sparse, OMP would find the exact solution in S iterations and the residual would be 0 after S iterations.

Concerning the computational cost, the matched filter (6.17) is cheaper than the OMP since the first iteration of the OMP algorithm is simply a normalised matched filter and OMP needs several iterations to find a sparse estimate of the scene reflectivity.

6.4.3.2 Stop criteria

One of the key parameter of an iterative procedure such as OMP is the stopping rule. The stop criterion selection depends on the *a priori* knowledge of the scene. One would stop after a maximum number of iterations is reached, e.g. S iterations if the scene is S-sparse. Another would continue until the energy in the residual signal falls below a threshold value related to the noise content in the SAR image. If no *a priori* knowledge of the scene is available, the required number of iterations or the residual signal energy can give information about the scene. Indeed, the required number of iterations can be seen as an estimate of the sparsity level of the scene and the residual energy as the noise content in the SAR image [132].

6.4.4 Limitations of compressive sensing

6.4.4.1 Resolution limitation

In the CS literature applied to SAR imaging [97, 99, 133, 134], sparse recovery methods may give the false impression of super-resolution since the SAR image is represented by the coefficients of the projection and not by the reconstructed signal. Figure 6.8 depicts the IRF along one isorange contour with one single scatterer. The sinc-shape of the conventional SAR method such as the MF can be recognised whereas the OMP method reconstructs the scene with only one coefficient. One could deduce that the OMP method is a super-resolution algorithm which can better resolve two closely-spaced targets than the MF and a finer grid would accentuate this false impression. In

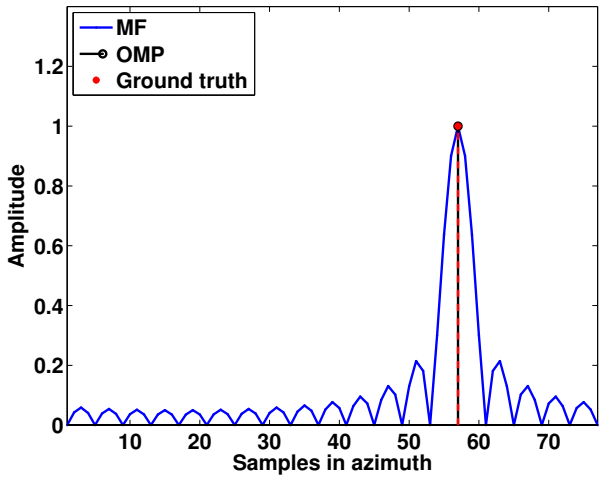

Figure 6.8: Azimuthal IRF of one single target.

fact, the resolution of sparse recovery methods is the same as the one of the conventional MF. Indeed, the projection of the measurement $\mathbf{y}$ on the dictionary, which is a step inherent to every CS algorithm, is equivalent to the application of the MF.

Let us illustrate the identical resolution limitation of both the OMP and the MF by an example. Two targets at different close distances along the same bistatic isorange contour are simulated and the azimuthal IRF is illustrated in Fig. 6.9. The left-hand target is fixed and the right-hand target changes position. The noiseless case and a uniform illumination ($\mathbf{W} = \mathbf{I}$) are considered. We consider a sampling grid made of

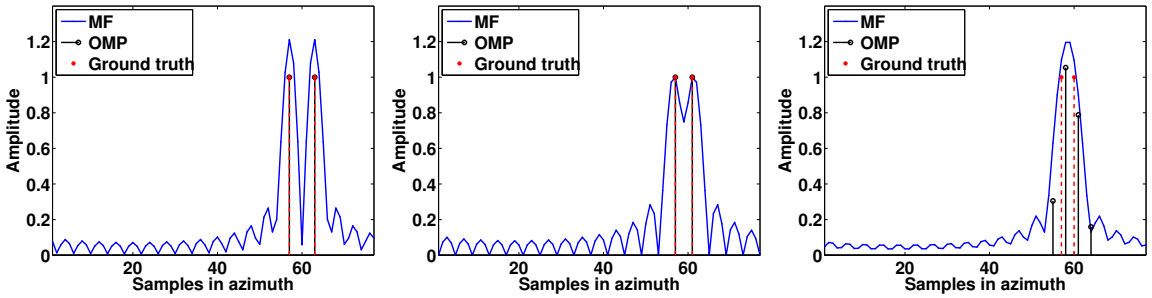

(a) 1.5 cell distance (b) 1 cell distance (c) 0.75 cell distance

Figure 6.9: IRF of two closely-spaced targets.

four samples per resolution cell as depicted in Fig. 6.10. The first iteration of the OMP algorithm, which is the projection of the measurement on the atoms of the dictionary, boils down to the normalised matched filter output, represented in blue in Fig. 6.9. The sidelobes of one target contributes to the value at the maximum of the other target, destructively or constructively, biasing the detection using the MF since the MF is optimal for targets in different resolution cells or for one target in the presence of white noise (6.17). When the distance is equal to or larger than one resolution cell, both the MF and OMP detect the correct number of targets as illustrated in Fig. 6.9 (a) and 6.9 (b). If the targets get closer than one resolution cell distance, the MF will detect only one target whereas OMP gets confused and detects four targets instead of two as depicted in Fig. 6.9 (c). Even if the simulated signal is the exact sum of two atoms of the dictionary, OMP cannot resolve two targets separated by less than one resolution cell. The reason is that the first predominant detected coefficient of the projection is biased by the presence of the second target leading to a residual signal which does not correspond to the second atom to detect.

6.4.4.2 Basis mismatch

The model (6.23) assumes that the targets on the scene are located on a discrete range and cross-range grid. A target not perfectly located on the sample grid is a phenomenon that occurs all the time since the sampling frequency is finite in range and in azimuth. It is thus important to investigate the performance of the proposed method when targets are at arbitrary location. Those targets are defined as off-grid targets and the problem as basis mismatch. Let us illustrate the off-grid effect on the same scenario as in previous

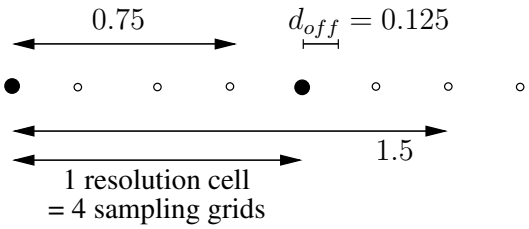

Figure 6.10: Illustration of the distances in the considered scenario.

section. Two targets with a decreasing distance are simulated with the right-hand target not on the grid with an off-grid distance equals to $d_{off} = 0.125$ as depicted in Fig. 6.10. Figure 6.11 shows the estimated reflectivity by the MF and OMP. The conclusions for the MF are similar to those of previous section whereas OMP introduces false targets even if the distance between the two simulated targets is larger than the resolution cell as illustrated in Fig. 6.11 (b).

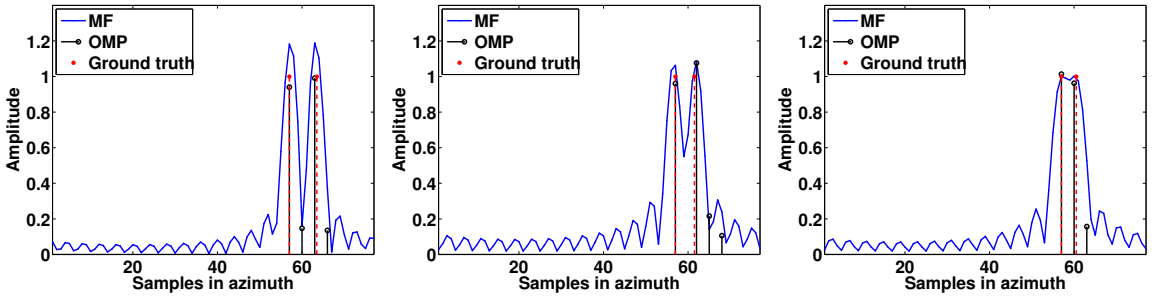

(a) $1.5 + d_{off}$ cell distance (b) $1 + d_{off}$ cell distance (c) $0.75 + d_{off}$ cell distance

Figure 6.11: IRF of two closely-spaced targets with the right-hand target not on the grid.

When conventional SAR algorithms are used such as the MF, off-grid targets do not degrade the SAR image. However, CS methods are typically not robust to off-grid

targets and a significant degradation of the reconstruction performance can be observed if the locations of the scatterers deviate from the imaging grid [133, 135]. Some additional non-zero coefficients appear for OMP which creates a non-sparse solution since the data cannot be represented with the dictionary columns corresponding to targets located on the grid. For additional iterations, more contributions can be expected, but on a level below that of those already included in the image. The phase of the simulated point scatterer will also deviate from the actual value.

To solve this problem, one would increase the density of the grid and thus increase the number of basis functions but it consequently increases the mutual coherence which must be small for good reconstruction. Furthermore, this also increases the computational complexity. Several solutions have already been proposed in the literature [133, 136–138].

6.5 Summary

In this chapter, a theoretical study of the burst-mode resolution enhancement method developed in this thesis and OMP has been done by simulating point-targets. As a conclusion, the performance of the method depends on the scene to be imaged and the exactitude of the prior knowledge injected in the method.

The performance of OMP essentially depends on the considered basis. This basis must respect the RIP condition to yield a perfect reconstruction of the scene. With the basis considered in this work, $\mathbf{H_w}$, the reconstruction performance will depend on the slow-time modulation $\mathbf{W}$ of the signal but also on the density of the sampling grid. A high density will increase the mutual coherence (6.24) which will degrade the reconstruction performance and a low density will give rise to off-grid targets. Secondly, the scene to be imaged must be sparse in the selected basis. With the basis considered in this work, $\mathbf{H_w}$, point-scatterers are sparse while distributed scatterers such as fields are not sparse. Therefore, the considered basis in this work will lead to a perfect reconstruction of point scatterers if RIP holds.

Concerning the burst-mode resolution enhancement method, if the scene reflectivity follows a Gaussian distribution and if $\mathbf{H}\mathbf{H}^\dagger$ is diagonal, the scene reconstruction will be optimum.

In the case of the GM mode of ENVISAT or when the SNR in the elevation side-

lobes is small, interruptions in the SAR phase history data collection occur. The burst-mode resolution enhancement method will give rise to grating lobes in the SAR image since the burst-mode resolution enhancement method minimises the MSE of the ground reflectivity and was not designed to maximise the PSLR. In that case, the OMP method could yield a SAR image with the same cross-range resolution as the burst-mode resolution enhancement method but without grating lobes if the considered dictionary fulfils the RIP condition (6.22) and if the scene to be imaged is sparse in the selected dictionary. Those conditions essentially depend on the slow-time modulation pattern and the chosen sampling grid.

Table 6.1 draws a parallel between the proposed method and the CS approach.

	Proposed method	CS
Prior knowledge	Gaussian model	sparsity
Condition	$\mathbf{H}\mathbf{H}^{\dagger}$ diagonal	$\mu \ll 1$
Drawback	noise amplification	not robust to off-grid scatterers

Table 6.1: Comparison of the burst-mode resolution enhancement method with the CS approach.

Chapter 7

Results

7.1 Introduction

In this chapter, we will demonstrate the crucial improvement in bistatic SAR imaging thanks to the burst-mode resolution enhancement method on a set of trial data. We will illustrate the trade-off the burst-mode resolution enhancement method strives to achieve between the grating lobes level and the noise amplification. In Section 7.2, signals acquired from several illuminators of opportunity operating in the frequency band of the receiver are shown.

The receiver described in detail in Appendix A.1 consists of four channels. During this work, the configuration of the receiver has changed by connecting different antennas or by using a reduced number of channels out of the four available. The antennas can be oriented either towards the scene or towards the illuminator of opportunity. Typically, in BSAR imaging, a channel called synchronisation channel is allocated for synchronisation purposes and oriented towards the transmitter to receive the direct pulses. In Section 7.3, we evaluate the error we make by using as reference the direct signal received in the backlobe of the channel oriented towards the scene to image, called the surveillance channel.

The innovative aspect of this thesis is that it is possible to produce images with high cross-range resolution from data obtained from a SAR system operating in wide-swath mode. The performance of the method are illustrated on signals obtained from burst-mode operating SAR systems such as RADARSAT-2 and Sentinel-1A in Section 7.4.

In contrast with monostatic SAR, not taking into account the topography of the

scene can lead to defocus in the bistatic SAR image [73]. This is evaluated in Section 7.5.

Finally, a bistatic SAR image of the bistatic active tranponder described in Appendix D is analysed and illustrates the bistatic SAR imaging algorithm developed in this thesis. The achieved cross-range resolution is better than the monostatic cross-range resolution of the SLC image in IW mode obtained by the SAR transmitter at the same time.

7.2 Received signals

The first signals acquired with the receiving system were the signals from the AMI instrument of ERS-2 and from the ASAR instrument of ENVISAT. Figures 7.1 (a) and (c) illustrate one IF direct signal pulse. Note the asymmetry of the signals resulting likely from a saturation of the RF amplifiers. The spectrograms in Fig. 7.1 (b) and (d) depict an up-chirp, the parameters of which correspond to those in Table 2.1.

Figure 7.2 (a) represents the four-beam IF signal acquired during an overpass of RADARSAT-2 operating in SWB mode. Figure 7.2 (b) represents the range compressed data of the surveillance channel signal. Note the presence of both the direct and the reflected signals since the antenna is directed towards the scene to image, receiving the direct signal through its backlobe. The typical slow-time modulation of the ScanSAR mode is clearly visible at null relative bistatic range, i.e. the position of the receiver. The parameters of the transmitted waveform of the four beams in SWB mode are given in Table 7.1. One IF direct-signal pulse and its spectrogram are represented

Table 7.1: Parameters of SWB mode of RADARSAT-2.

Parameter	W1	W2	S5	S6
Centre frequency, f_T, GHz		5.405		
Bandwidth, B, MHz		11.56		
Pulse duration, T_p, μs		42		
Chirp rate, α, GHz/s		-279.3		
PRF, Hz	1285	1328	1285	1343

in Fig. 7.2 (c) and (d). Note that RADARSAT-2 transmits down-chirp pulses, i.e. the

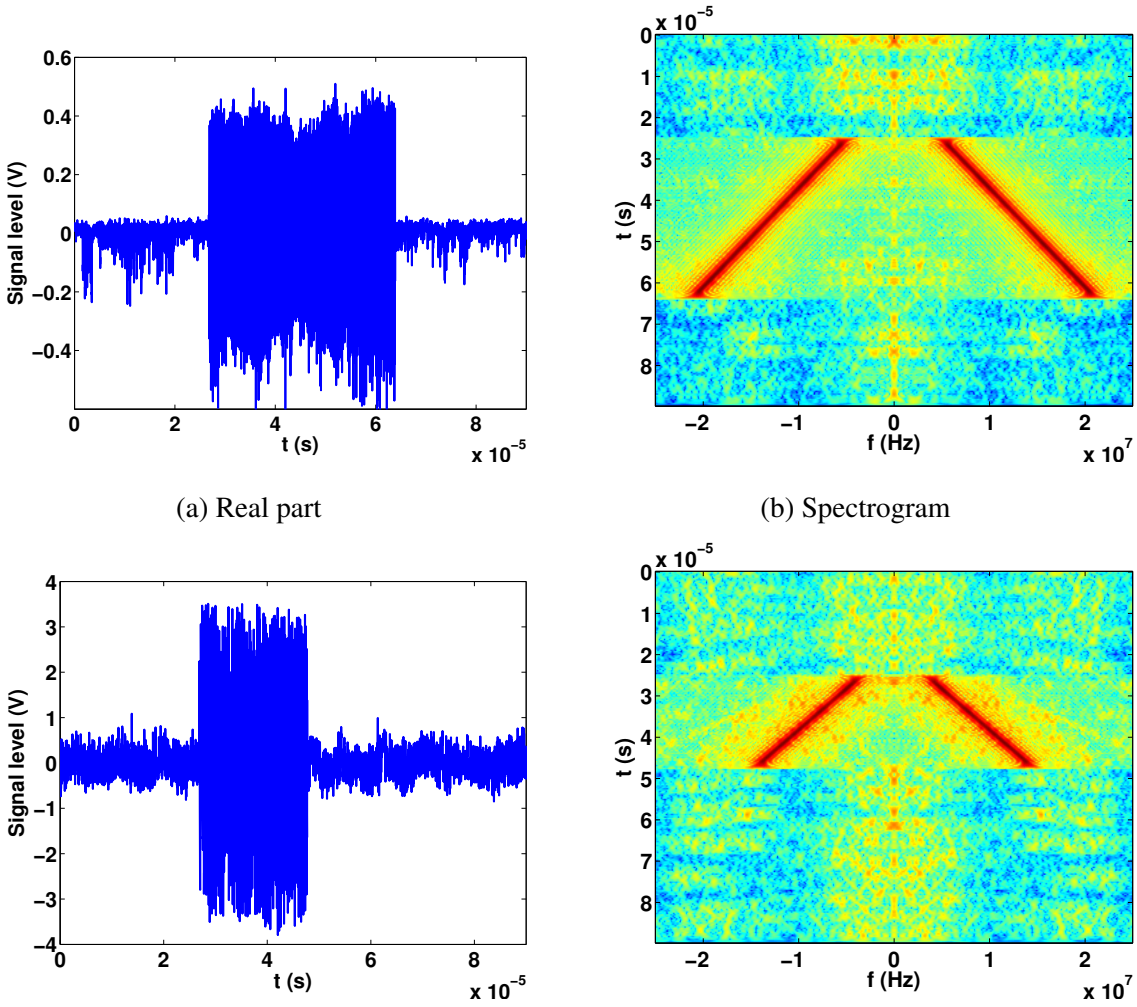

(a) Real part

(b) Spectrogram

(c) Real part

(d) Spectrogram

Figure 7.1: One IF direct signal pulse acquired (a) during a stripmap illumination of ERS-2 (29/10/2010 12:36:38 UTC) and (c) during a ScanSAR illumination of ENVISAT (16/03/2012 10:03:00 UTC) with a sampling frequency equal to 50 MHz.

chirp rate α is negative as stated in Table 7.1. The SNR of the direct signal is equal to 22 dB.

Figure 7.3 (a) represents the two-beam IF direct signal acquired during an overpass of Sentinel-1A operating in IW mode over the ground-based receiving system. During this acquisition, the receiver and the scene to be imaged are first illuminated by the elevation beam illuminating sub-swath 2, from 0 to 0.66 s (IW2) in Fig. 7.3 (a) followed by the elevation sidelobe of the elevation beam illuminating sub-swath 3, from 0.66 to 1 s (IW3) in Fig. 7.3 (a). A small gap of 0.01 s occurs between the two illuminations due to the steer time of the transmit antenna. Note that the parameters

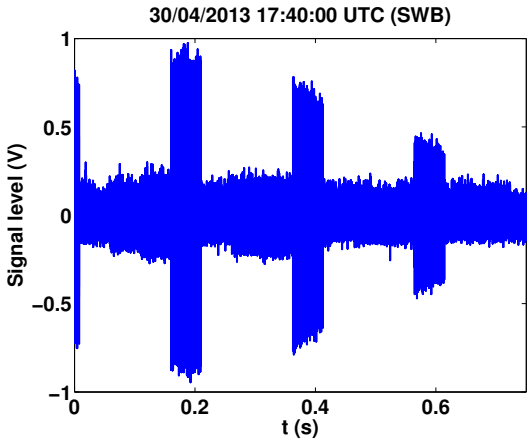

(a) ScanSAR signal

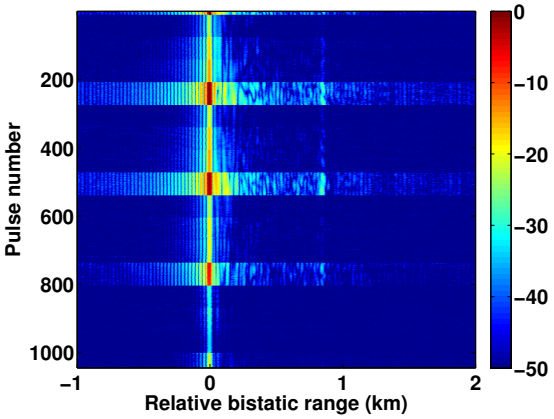

(b) Range-compressed ScanSAR signal

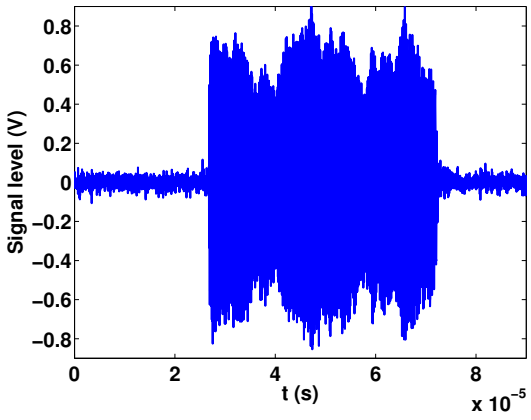

(c) Real part of one pulse

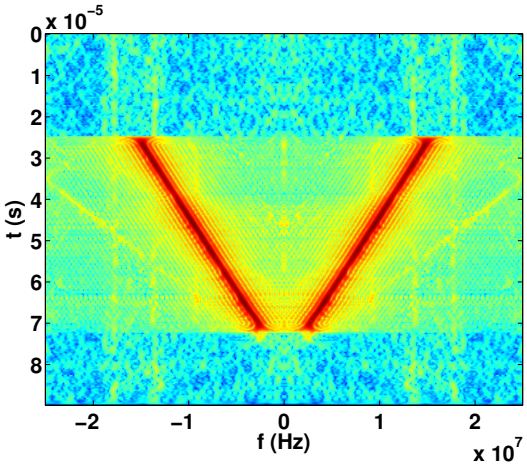

(d) Spectrogram of one pulse

Figure 7.2: (a) Signal acquired during an overpass of RADARSAT-2 operating in SWB mode, (b) the corresponding range compressed data (logarithmic scale), (c) one IF direct signal pulse with sampling frequency equal to 50 MHz and (d) its spectrogram.

of the transmitted signal are different in each sub-swath of the IW mode and are given in Table 7.2. Figure 7.3 (b) depicts the magnitude of the range-compressed data of the surveillance channel. One IF direct signal pulse and its spectrogram are respectively depicted in Fig. 7.3 (c) and (d). The SNR of the direct signal is equal to 26 dB. The measured chirp rate α, i.e. the slope of the spectrogram, the chirp duration T_p and the bandwidth B correspond to the specifications listed in Table 7.2.

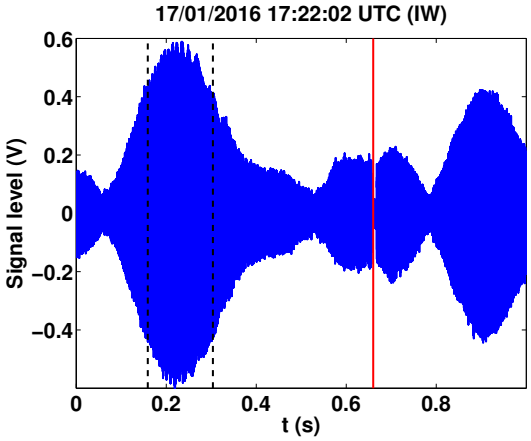

(a) TOPSAR signal

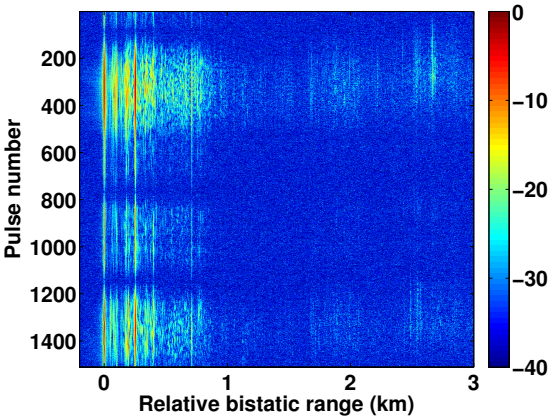

(b) Range-compressed TOPSAR signal

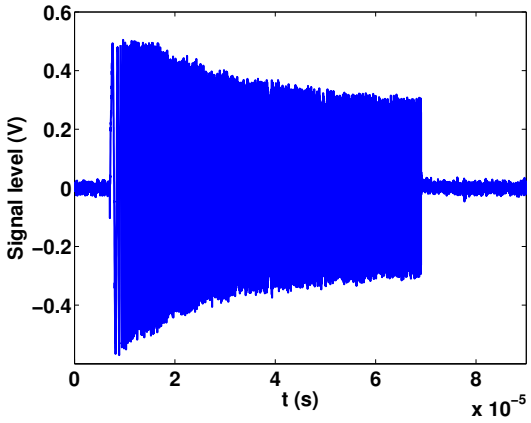

(c) Real part of one IW2 pulse

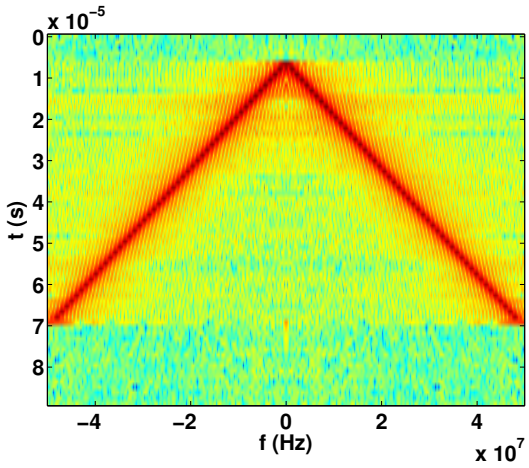

(d) Spectrogram of one IW2 pulse

Figure 7.3: (a) Direct signal acquired during an overpass of Sentinel-1A operating in IW mode (IW2 and IW3), (b) the range-compressed data of the surveillance channel (logarithmic scale), (c) one IF direct signal pulse (IW2) with sampling frequency equal to 100 MHz and (d) its spectrogram.

Table 7.2: Parameters of IW mode of Sentinel-1A.

Parameter	IW1	IW2	IW3
Centre frequency, f_T, GHz		5.405	
Bandwidth, B, MHz	56.5	48.3	42.8
Pulse duration, T_p, μs	52.4	61.9	53.4
Chirp rate, α, GHz/s	1078	779	801
PRF, Hz	1717	1451	1685

7.3 Receiver phase synchronisation

In this thesis, phase synchronisation is performed using the direct signal as the reference signal to derive the matched filter as described in Section 4.3. The question is whether the direct signal received in the backlobe of the surveillance channel pointing towards the scene can be used to perform the synchronisation. To answer this question, we will compare the reference phase recovered from the synchronisation channel pointing towards the transmitter and that recovered from the surveillance channel.

The analysed experiment was performed with the receiver sited on the roof of one of the buildings of the Military Hospital in Brussels, on 15^{th} February 2016, the corresponding signal is represented in Fig. 7.4. The imaging scenario is described in

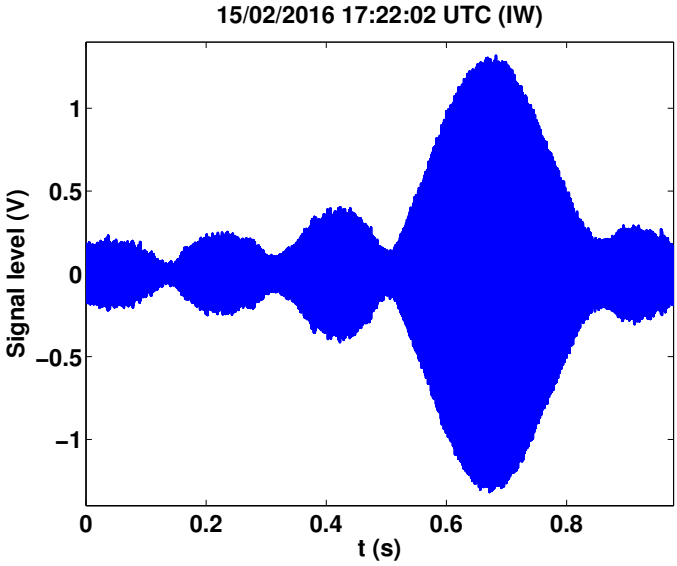

Figure 7.4: Acquired direct signal during a TOPSAR illumination (IW2) of Sentinel-1A (synchronisation channel).

detail in Appendix C.3. For this study, two channels of the receiver are used: one channel oriented towards the transmitter and one channel towards the scene to image. Figure 7.5 depicts one pulse and its echoes after range compression received by the synchronisation channel and by the surveillance channel. The SNR of the direct signal in the synchronisation channel is 17 dB higher than that in the surveillance channel.

The phase history of the direct signal is obtained as described in Section 4.3. The reference phase is extracted from the synchronisation channel on the one hand, and on the other hand, from the surveillance channel. For this analysis, the whole signal

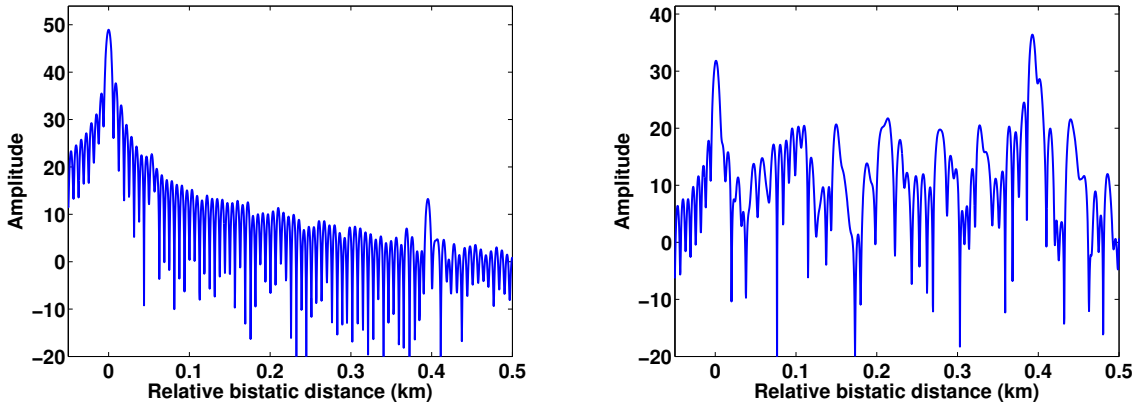

(a) Synchronisation channel (b) Surveillance channel

Figure 7.5: Pulse compression of one pulse acquired during a IW2 illumination of Sentinel-1A (logarithmic scale).

depicted in Fig. 7.4 is considered.

Figure 7.6 represents the distribution of the phase history error between the reference phase extracted from the synchronisation channel and the reference phase extracted from the surveillance channel. The standard deviation is 0.1122 rad. As the error is low, one concludes that the reference phase can be extracted from the surveillance channel. This has already been reported in [139].

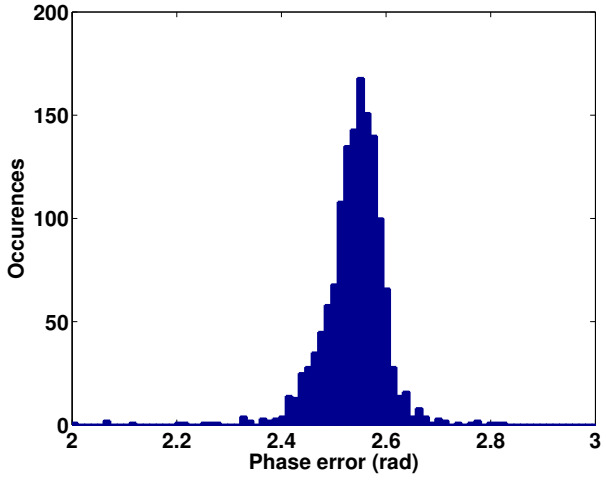

Figure 7.6: Histogram of the phase error on the reference signal.

7.4 Achieved performance in wide-swath illumination

7.4.1 ScanSAR illumination

The analysed signal was acquired in Scenario C.2 with the receiver sited on the roof of one of the buildings of the Royal Military Academy in Brussels, on 30^{th} April 2013. The satellite pass was ascending and the stationary receiver was in the centre of the swath of the Canadian satellite RADARSAT-2 operating in the ScanSAR Wide mode (SWB). The acquired signal is represented in Fig. 7.2 (a). The BSAR images are obtained using one channel directed towards the scene to image. The performance of the burst-mode resolution enhancement method can be better illustrated by analysing a patch in the SAR image with a high reflectivity represented by a blue dot in Fig. 7.7. A flat-earth model is used to image the area of interest. Figure 7.7 (a) shows the intensity of the SLC SAR image centred on the aforementioned patch obtained by the classical MF processing of a single burst, i.e. considering the signal from 0.16 s to 0.21 s in Fig. 7.2 (a). This yields a poor resolution of 100 m in the along-track direction which corresponds to the monostatic cross-range resolution of SWB mode reported in Table 2.1. The reflections of the analysed patch are visible at 805 m relative bistatic range from the receiver in Fig. 7.2 (b). If the N_L bursts of this same beam are coherently focussed, the along-track resolution is drastically improved to 20 m as illustrated in Fig. 7.7 (b). The expected grating lobes in azimuth along the isorange can be observed. Note that a second patch with a high reflectivity represented by a red dot is hidden in the grating lobes.

The white square in the upper right corner of Fig. 7.7 represents a region assumed free of scatterers. It is used to estimate the background noise level with respect to the single-beam MF case of Fig. 7.7 (b). The corresponding values are given in Table 7.3. If the burst-mode resolution enhancement method is applied with the true value ϑ_{true}, there is a trade-off between the amplification of the noise and the reduction of the grating lobes. The latter are reduced but still present in Fig. 7.7 (d). The second aforementioned patch is now visible. For $\vartheta < \vartheta_{true}$, the cross-range compensation function $\mathbf{c_w}$ becomes closer to the inverse of $\mathbf{w}$: a better compensation of the slow-time amplitude modulation is obtained at the expense of an increase of the noise content in the SAR image (Fig. 7.7 (c)). This illustrates that the compensation function $\mathbf{c_w}$ must be

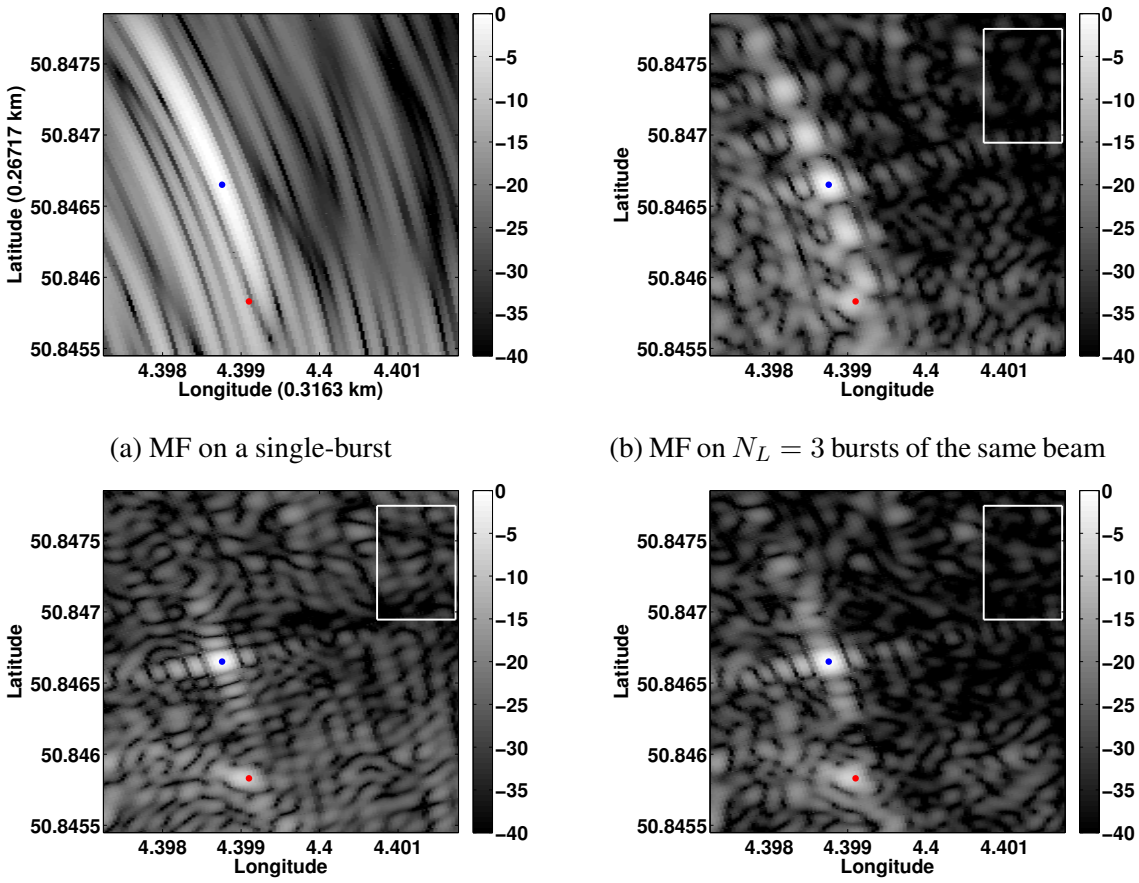

(a) MF on a single-burst

(b) MF on $N_L = 3$ bursts of the same beam

(c) Resolution enhancement method $\vartheta < \vartheta_{true}$

(d) Resolution enhancement method $\vartheta = \vartheta_{true}$

Figure 7.7: Zoom on a patch in the georeferenced bistatic SLC SAR image (logarithmic scale).

Table 7.3: Noise level estimation relative to the single-beam MF case.

SAR focussing method	Relative noise variance dB
Burst-mode resolution enhancement method for $\vartheta = \vartheta_{true}$ (Fig. 7.7 (d))	16
Burst-mode resolution enhancement method for $\vartheta < \vartheta_{true}$ (Fig. 7.7 (c))	33.5

calculated with the correct SNR, ϑ_{true}. This final result illustrates that the burst-mode resolution enhancement method provides high cross-range resolution SAR images relative to the classical single-burst ScanSAR imaging: the SAR image has reduced grating

lobes but an acceptable noise amplification.

Taking interferometry as a possible application, the noise amplification induced by the burst-mode resolution enhancement method can also be evaluated using the sample coherence (6.20) as it was performed on simulated data in Section 6.3.4.3. To concentrate on the study of the phase noise generated by the burst-mode resolution enhancement method, two channels during a single pass acquisition are considered as the phase noise due to temporal change of the scene vanishes. In addition, the baseline between both considered channels is small to avoid spatial decorrelation caused by a different look angle between the SAR images, which is also known as baseline decorrelation. The sample coherence between the images obtained from two adjacent channels using the different SAR processing are illustrated in Fig. 7.8. The loss in coherence in Fig. 7.8 (b) emphasises the decorrelation due to the amplification of the noise. This final result illustrates that the cross-range resolution enhancement method preserves phase coherence for sufficient SNRs, despite noise amplification.

The coefficients of the OMP method are depicted in Fig. 7.9 (a). For the sake of comparison, the SAR image resulting from the burst-mode resolution enhancement method is again represented in Fig. 7.9 (b). The OMP method is implemented isorange by isorange. The bistatic OMP SAR image highly depends on the sampling grid used. In Fig. 7.9 (a), both considered point scatterers are on the sampling grid.

7.4.2 TOPSAR illumination

In this section, TOPSAR data are used to demonstrate the achievable performance in terms of cross-range resolution of the burst-mode resolution enhancement method. According to Table 2.1, one can see that the TOPSAR imaging mode implemented on Sentinel-1A [140] is characterised by an imbalance between the monostatic range and the monostatic cross-range resolution which means that improving this coarse cross-range resolution thanks to a bistatic configuration is valuable. In TOPSAR acquisition, the sampling frequency of the receiver has been increased compared to ScanSAR acquisition since the transmitted bandwidth is larger. Due to hardware limitation, the acquisition duration of TOPSAR recording is limited to 1 second which limits the improvement of cross-range resolution by the burst-mode resolution enhancement method. A larger sampling time would result in even better cross-range resolution.

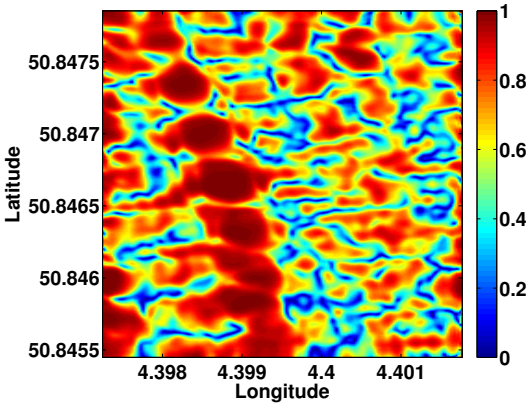

(a) MF

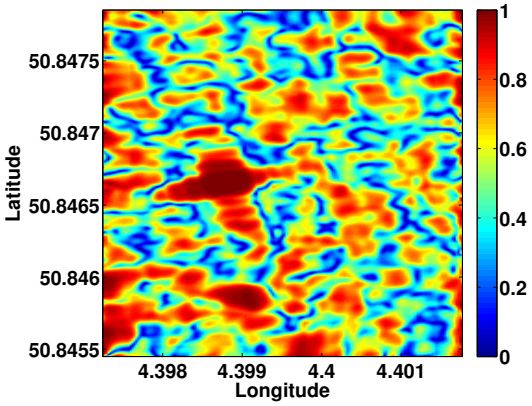

(b) Resolution enhancement method $\vartheta < \vartheta_{true}$

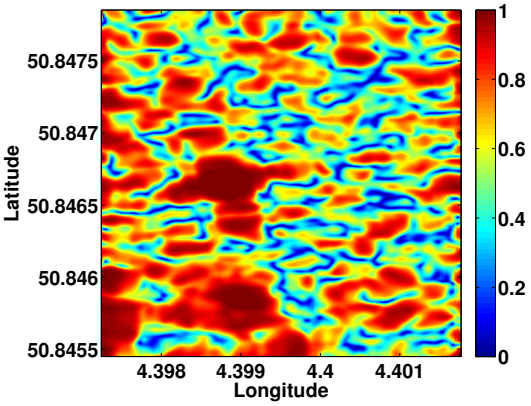

(c) Resolution enhancement method $\vartheta = \vartheta_{true}$

Figure 7.8: Sample coherence image between the SAR images obtained from two horizontally-spaced channels.

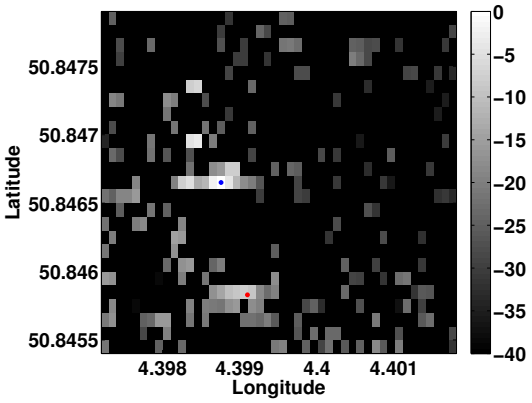

(a) OMP

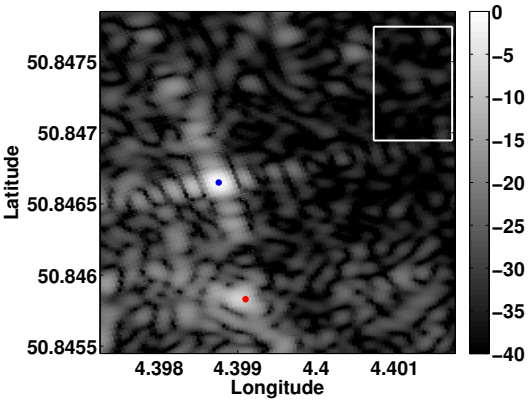

(b) Resolution enhancement method

Figure 7.9: Zoom on a patch in the georeferenced bistatic SLC SAR image (logarithmic scale).

The analysed signal was acquired with the receiver sited on the roof of one of the buildings of the Military Hospital in Brussels, on 17^{th} January 2016. The satellite pass was ascending and the stationary receiver was in the centre of the swath of Sentinel-1A operating in TOPSAR mode (IW). The imaging scenario is described in detail in Appendix C.3. The BSAR images are obtained using one channel directed towards the scene to image.

Figure 7.10 shows the intensity of the bistatic SAR SLC image for an area around the receiver using the burst-mode resolution enhancement method integrating all pulses depicted in Fig. 7.3 (a). The added benefit of the Back-Projection processing described

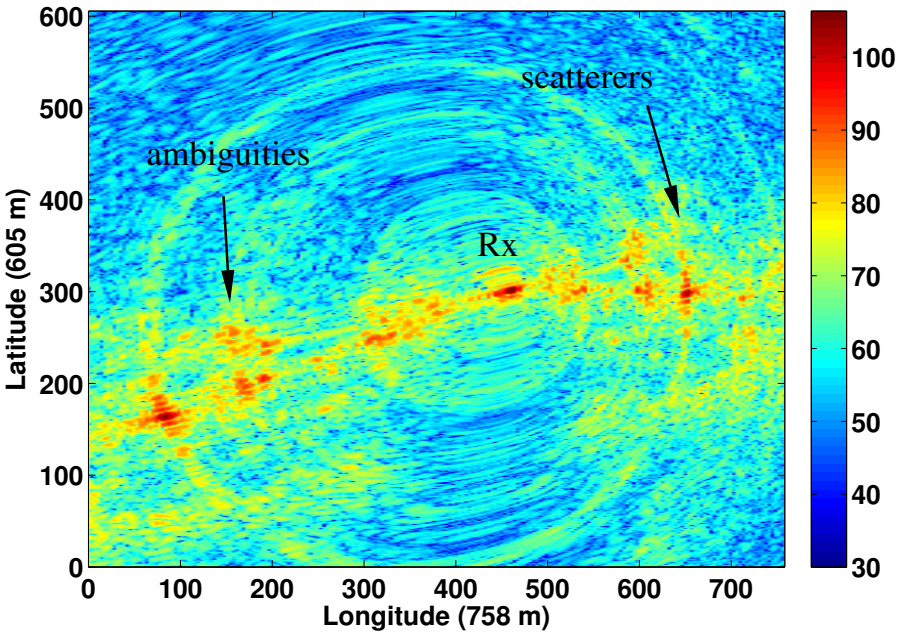

Figure 7.10: Bistatic SAR image using Sentinel-1A signal for the acquisition of 17/01/2016 at 17:14:02 UTC (logarithmic scale).

in Section 2.2.2 is that the image is directly obtained in ground range and no separate geocoding step needs to be performed. A flat-earth model around the receiver is assumed. The direct signal is focussed at the location of the receiver. The bistatic image shows ambiguities which appear at the intersection of the bistatic isorange contours with the bistatic constant azimuth lines represented respectively in solid blue and in dashed black in Fig. 7.11. The bistatic isorange contours are ellipses as they are the intersections of ellipsoids and a plane and the bistatic constant azimuth lines are straight lines parallel to the look direction of the satellite. The bistatic isorange con-

tours have a spacing of 100 m in relative bistatic range while the spacing between the constant azimuth lines is 200 m in Fig. 7.11. Patches at these intersections would generate identical phase histories. Since the returns from ambiguous scatterers are strongly attenuated by the AAP of the receive antenna and by some RAM material, it is assumed that no ambiguities will appear in the SAR image. The range sidelobes of the IRF of the patch corresponding to the receiver's location follow the constant azimuth line passing through the receiver and are barely visible in Fig. 7.10. This proves that the backlobe of the receive antenna and the RAM material attenuate the direct signal.

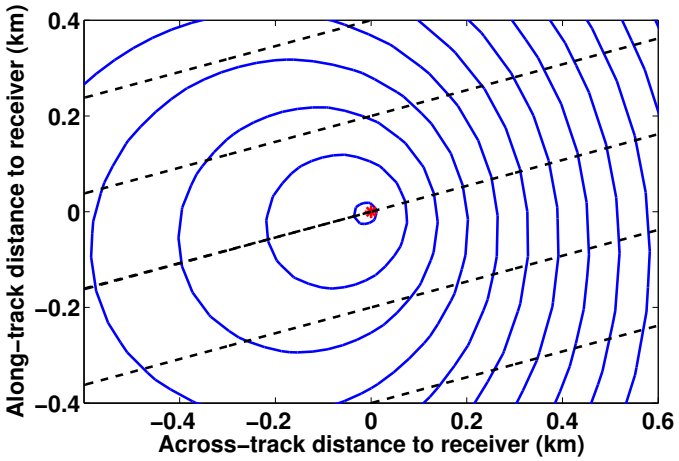

Figure 7.11: Bistatic isorange contours (solid blue) and bistatic constant azimuth lines (dashed black) for the acquisition of 17^{th} of January 2016. The receiver position is marked with a red star.

To illustrate the performance in terms of cross-range resolution achieved by the burst-mode resolution enhancement method, a SAR image has been computed with the traditional integration time of classical monostatic processing [76], i.e. 3 dB mainlobe width of the transmit antenna, and is illustrated in Fig. 7.12 (a): the pulses between the dashed black lines in Fig. 7.3 (a) are considered to build the SAR image. The measured cross-range resolution is equal to 22 m and corresponds to the theoretical monostatic value given in Table 2.1. This poor cross-range resolution can be enhanced by integrating the pulses transmitted in the azimuth sidelobes of beam IW2, i.e. from 0 to 0.66 s in Fig. 7.3 (a) using the MF. The resulting bistatic SAR image is represented in Fig. 7.12 (b). The cross-range resolution can be further enhanced if the elevation antenna diagram sidelobes of beam IW3 are also exploited, corresponding to the pulses

from 0.66 s to 1 s in Fig. 7.3 (a). The SAR focussed image represented in Fig. 7.12 (c) shows a high energy in the sidelobes which can be noticed around patches with a large reflectivity. This is due to the slow-time modulation of the signal corresponding to the entire envelope of Fig. 7.3 (a). Without the burst-mode resolution enhancement method, each patch has high sidelobes which could cause ghosts in the image. In Fig. 7.12 (d), the sidelobes are reduced after application of the burst-mode resolution enhancement method and the patches can be easily distinguished. The achieved cross-range resolution is now comparable to that of the stripmap mode of the considered satellite (Table 2.1). In other words, the cross-range resolution is five times better than that of the monostatic SAR image produced by the transmitter at the same time. A

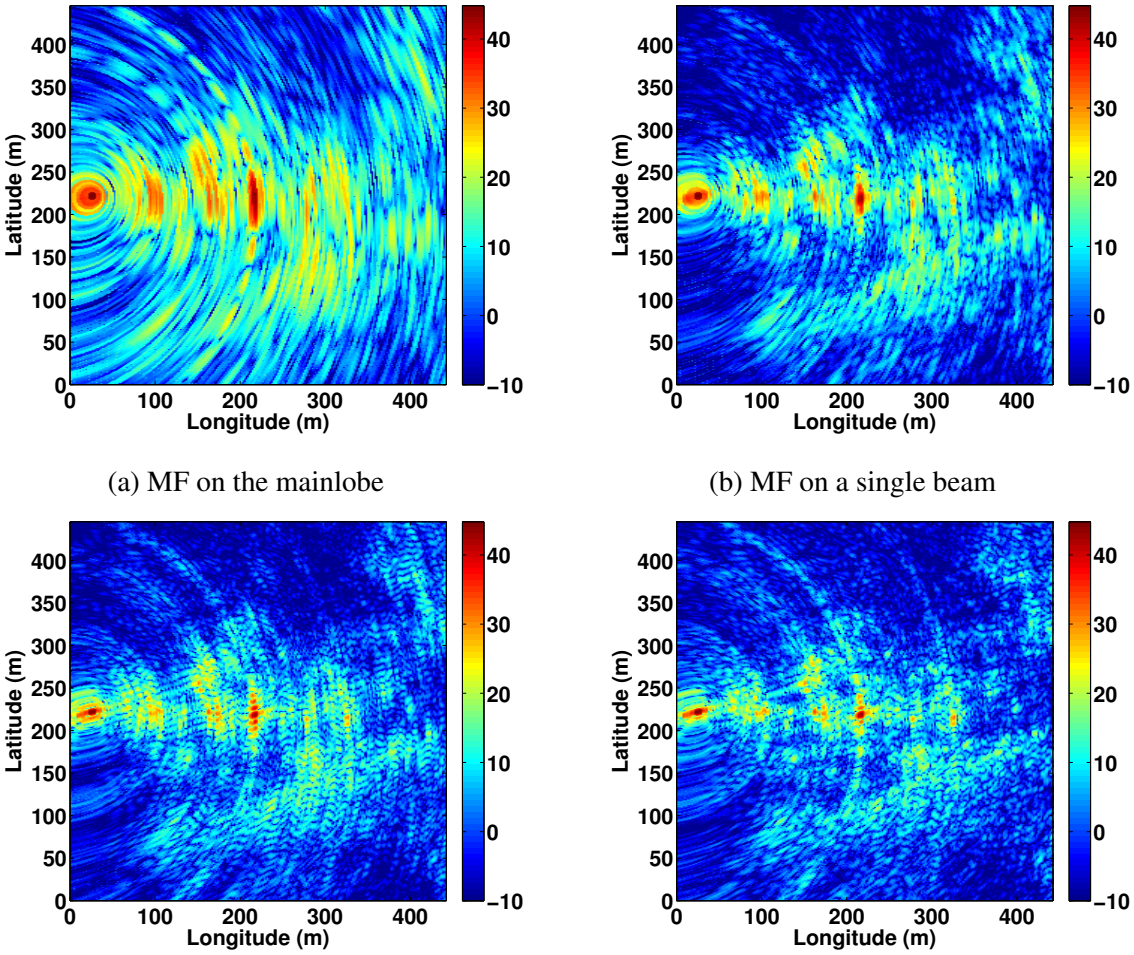

(a) MF on the mainlobe

(b) MF on a single beam

(c) MF on two adjacent beams

(d) Resolution enhancement method

Figure 7.12: Zoom near the receiver in the georeferenced bistatic SLC SAR image (logarithmic scale) (17/01/2016 at 17:14:02 UTC).

summary of the measured cross-range resolutions is given in Table 7.4.

Table 7.4: Performance of the different processing in the cross-range direction.

Parameter	Monostatic	IW2	IW2 and IW3
Processing gain (dB)	23.24	29.79	31.79
Cross-range resolution (m)	22	9	4.5

7.5 Effect of the topography

In this thesis, a flat-earth model is assumed to produce the BSAR images. In contrast to monostatic SAR, this assumption may affect the SAR focussing [73]. Indeed, according to (2.18), two patches on the same isorange and on the same constant azimuth line but at different altitudes will have different phase histories as their slant range of closest approach to the transmitter and their distance to the receiver will be different. By considering a flat-earth model instead of the actual DEM of the scene, a phase error results that we can quantify considering for instance the Scenario C.3.

From (2.18), the phase history error between two patches on the same isorange, at the same azimuth but at different altitudes can be written as

$$\varphi_1(u) - \varphi_2(u) = \frac{2\pi}{\lambda}\frac{V^2u^2}{2}\frac{R_{T,0,2} - R_{T,0,1}}{R_{T,0,1}R_{T,0,2}} \tag{7.1}$$

with $R_{T,0,1}$ and $R_{T,0,2}$ the slant range of closest approach to the transmitter of respectively patch 1 and 2. u is the slow-time interval during which the signal is acquired. We evaluate (7.1) with $u = 1$ s which corresponds to the maximal duration of the acquisition of the experimental system at a sampling frequency of 50 MHz. The patch is first considered at the same altitude as the receiver denoted as position 1. Then, its altitude is varied on the same isorange and on the same azimuth line till a maximal phase error of $\frac{\pi}{2}$ is achieved. Figure 7.13 represents the critical altitude difference at which the phase error can cause a defocus in the SAR image as a function of the distance from the receiving system. Close to the receiver, the maximal phase error is never exceeded and the critical altitude is infinite. The larger the distance to the receiver, the smaller the critical altitude, meaning that the altitude difference of distant patches is more limited than that of closer patches. As an example, the altitude of a patch at a distance of 1260 m to the receiver must not exceeds a difference of 730 m with the altitude of the processed image, otherwise its IRF will be defocussed. Note that, in Belgium where the signals have been acquired, the maximal altitude difference between two points is

much smaller than the critical altitudes in Fig. 7.13. A DEM is, in that case, not needed to focus bistatic SAR images but may be required in order to correctly georeference the patches.

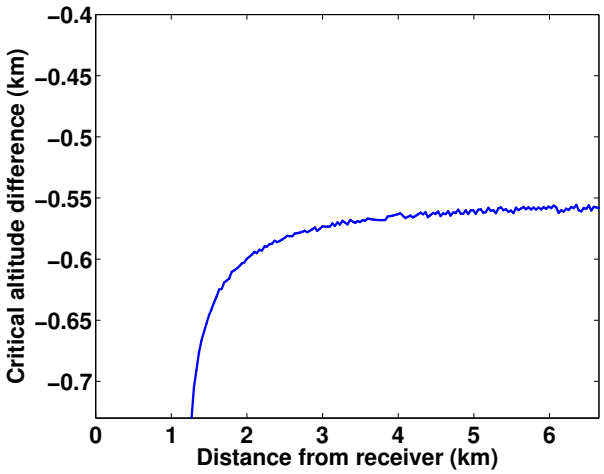

Figure 7.13: Evolution of the critical altitude difference (km) w.r.t the receiver.

7.6 Bistatic scattering

Figure 7.14 shows the bistatic SAR image obtained with the burst-mode resolution enhancement method and the corresponding optical image from Google Earth. The analysed signal depicted in Fig. 7.4 was acquired in Scenario C.3 with the receiver sited on the roof of one of the buildings of the Military Hospital in Brussels pointing East. The different motorways at a distance of 3 km are visible on the BSAR image despite the relatively low altitude of the receiver. Strong reflections on the buildings along the canal allow to distinguish the canal banks in the BSAR image. Finally, the metallic bridge ”Buda” depicted in Fig. 7.15 also leads to strong reflections.

This promising result is obtained assuming a flat-earth model and using the direct signal received in the backlobe of the surveillance channel.

7.7 Transponder bistatic image

Also deployed during this trial was the developed active bistatic transponder described in Appendix D located at 270 m from the receiver as illustrated in Fig. C.5. Figures 7.16 depict the BSAR image centred on the patch corresponding to the location of the transponder using the MF and the burst-mode resolution enhancement method.

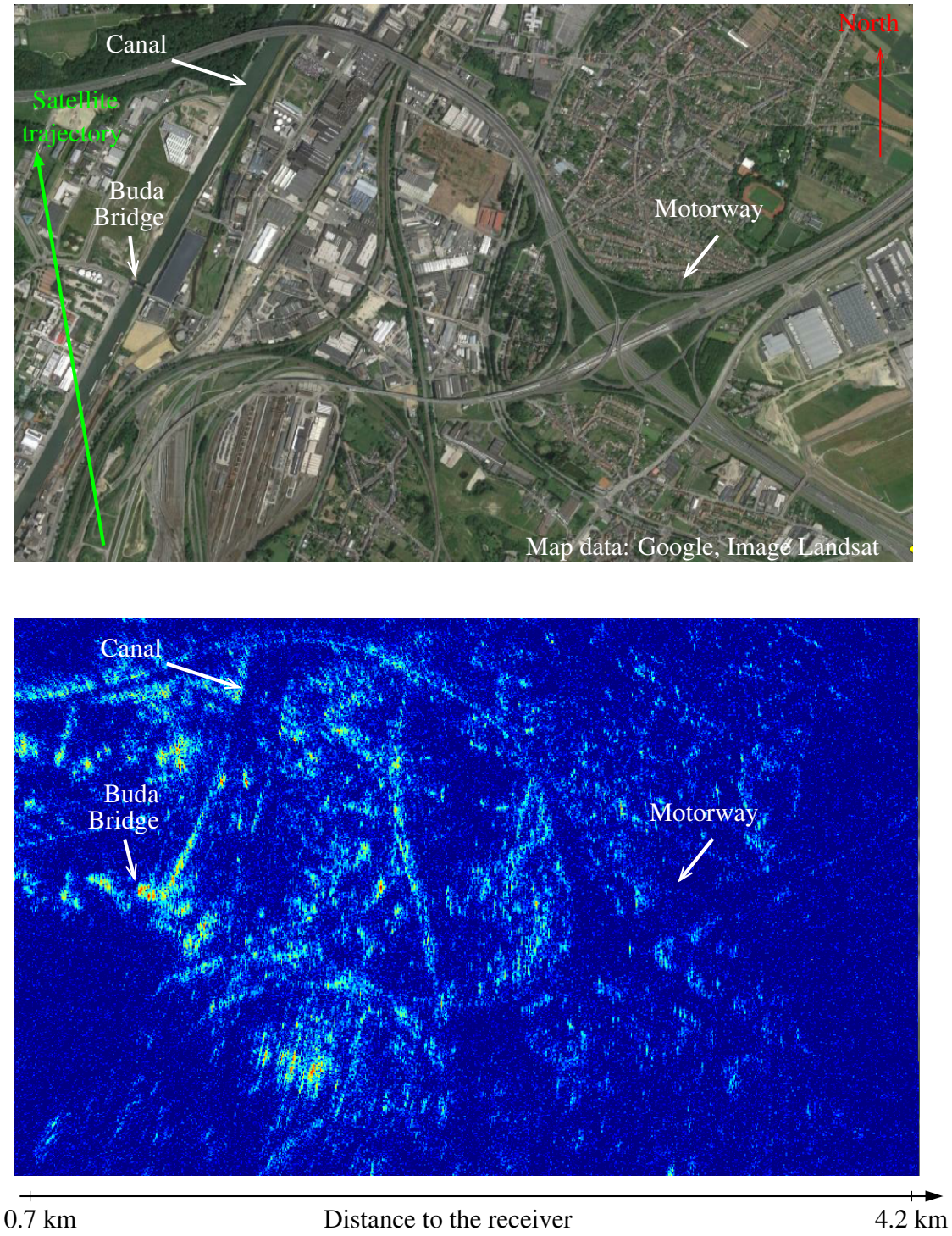

Figure 7.14: Bistatic SAR image (logarithmic scale) and the corresponding optical image (Google Earth) of the East area of the Military Hospital site on 15^{th} February 2016.

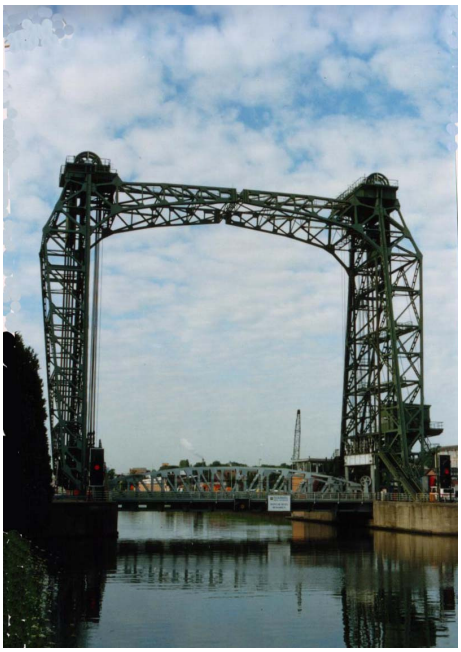

Figure 7.15: ”Buda” bridge on the Canal in Brussels.

This BSAR image has been obtained using the direct signal received in the backlobe of the surveillance channel. Cuts of the IRF along the bistatic isorange contour using the

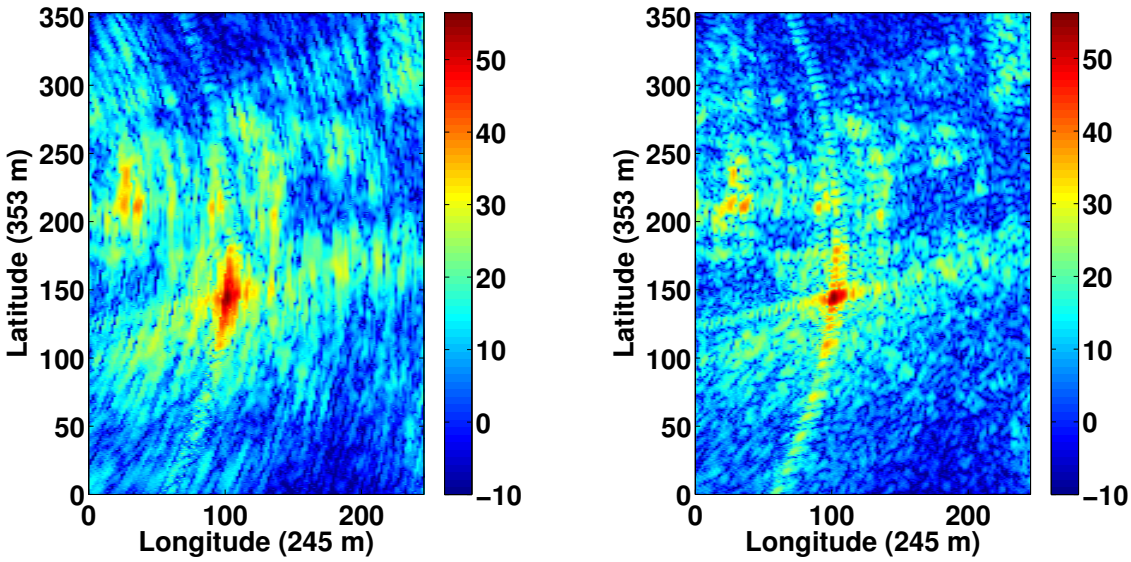

(a) MF

(b) Resolution enhancement method

Figure 7.16: Zoom on the patch at the location of the transponder in the georeferenced bistatic SLC SAR image (logarithmic scale) (15/02/2016 at 17:22:02 UTC).

MF (dashed line) and the burst-mode resolution enhancement method (solid line) are

illustrated in Fig. 7.17. The slow-time modulation of the amplitude of the transmitted signal results in a high level of sidelobe in the case of the MF. However, the burst-mode resolution enhancement method considerably decreases the level of azimuth sidelobes in the IRF. The peaks around the peak corresponding to the transponder are likely due to the presence of scatterers near the position of the transponder.

The resulting cross-range resolution obtained with the burst-mode resolution enhancement method is equal to 6.15 m which is better than the monostatic cross-range resolution of a SLC image in IW mode obtained by the SAR transmitter at the same time. The obtained bistatic cross-range resolution is also in the same order of magnitude as that of the monostatic stripmap mode as stated in Table 2.1.

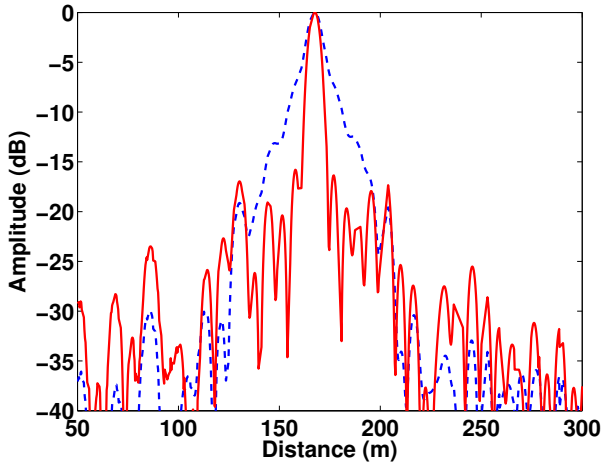

Figure 7.17: Cuts of the IRF along the transponder's isorange obtained using the MF (dashed line) and the burst-mode resolution enhancement method (solid line).

7.8 Conclusion

In this chapter, we have demonstrated that the proposed burst-mode resolution enhancement method provides a better cross-range resolution compared to the classical processing of a single burst and can even recover the stripmap cross-range resolution in ScanSAR and TOPSAR modes. This can be achieved in the case of a continuous illumination of the scene to be imaged. OMP imaging also gives good results since the considered dictionary fulfils the RIP condition (6.22) and the scene to be imaged is sparse in the selected dictionary. Note that those conditions essentially depend on the slow-time modulation pattern and the chosen sampling grid.

In addition, the flat-earth assumption has been verified for the Scenario C.3 and does not lead to defocus in the BSAR image. The phase synchronisation using the attenuated direct signal received in the backlobe of the surveillance channel also provided good results.

Chapter 8

Conclusions and future work

8.1 Summary of findings

The main aim of this thesis has been the analysis of high cross-range bistatic SAR imaging using data obtained from non-cooperative space-based SAR systems operating in wide-swath mode. For such systems, the cross-range resolution is typically obtained by processing of a single-burst data yielding a degraded cross-range resolution compared to the conventional stripmap mode. The novelty of this work arises from the exploitation of the sidelobe emissions of the elevation beams illuminating the adjacent sub-swath. We demonstrated that, if the SNR of the backscattered signals is sufficient, i.e. when the illumination is continuous, the performance of the stripmap mode can even be restored. We have also demonstrated that, based on the EAP of the transmitter, we are able to predict when the burst-mode resolution enhancement method achieves its targeted performance.

A CS-approach has also been proposed in the case of a non-continuous illumination in which the burst-mode resolution enhancement method's resulting image is impaired by high sidelobes of the IRF.

The generation of focussed BSAR images have highlighted the synchronisation challenge between the non-cooperative transmitter and the receiver. The synchronisation is here achieved using the direct-path signal to derive the matched filter. The requirement on the difference between the frequencies of the local oscillators in this geometry has been analysed and requires a less accurate precision compared to general bistatic configuration [107]. However, the precision of the available ephemerides, the precision of the orbit propagator and the stability of the local oscillator of the receiver

and of the transmitter may impose constraints on the maximal scene size to be imaged depending on the final application.

Applications to real data obtained in two different scenarios have demonstrated the effectiveness of the proposed method. In addition, an active bistatic transponder has been developed during this thesis to support the experimental validation of the bistatic SAR processing.

The burst-mode resolution enhancement method has a significant operational interest in the opportunistic space-ground geometry as it allows to image more frequently a specific area with a high cross-range resolution. Indeed, the imaging mode of space-borne SAR instruments is most often a wide-swath mode. As an example, ESA's satellite Sentinel-1A uses the IW mode as the pre-defined mode over land [141]. Making it possible to exploit those modes to produce images with high cross-range resolution dramatically increases the number of useful images that can be produced using emitters of opportunity. This benefit becomes even more important as several constellations of satellites can be exploited.

8.2 Future work

8.2.1 SNR of the BSAR image

The resulting bistatic SAR images produced some useful results, but there is plenty of scope for improvement. Although the results obtained with the receiving system are acceptable, it would be useful to improve the hardware in terms of SNR to obtain SAR images with a higher SNR, thus showing dimmer scatterers.

8.2.2 Georeferencing the BSAR image

In this work, a simplistic flat-earth model has been used to produce the BSAR images. The flat-earth assumption is only applicable to specific scenarios. As stated in [73], using a DEM of the scene to be imaged would improve the SAR focussing performance at the expense of an increased computational burden. The possible defocus of the SAR image due to the flat-earth assumption has been evaluated in Section 7.5 and we demonstrated that in the scenarios considered in this thesis, the phase error made by considering a flat-earth model will not lead to a defocus of the SAR image. A DEM is however needed to georeference the SAR image.

8.2.3 Calibration of the BSAR image

The developed active bistatic transponder allowed to validate the BSAR imaging in terms of geometry and performance of the method. Its characterisation in terms of RCS would be necessary for radiometric image calibration.

8.2.4 Direct-path interference

In this thesis, a wisely chosen pointing direction and the addition of RAM material provided attenuation of the direct path. In [83, 84], we also analysed the CLEAN algorithm. The CLEAN algorithm is applied separately for each range profile.

Using a CS method to perform SAR imaging is another way to mitigate the high sidelobes of the IRF of the direct signal since the CS method will image the point target corresponding to the direct signal with one strong coefficient without any sidelobes.

The multichannel configuration could be exploited to perform spatial beamforming to steer a null in the direction of the transmitter in order to attenuate or null the direct-path signal. This method requires a calibration of the array antenna. As discussed in [80], the anechoic chamber calibration procedure has the drawbacks of being time consuming and is not adapted for a changing electromagnetic environment. Calibration data can be estimated in the field directly from the impinging signals themselves, without the aid of any special calibration source. In addition, in SAR bistatic imaging, characterisation (calibration) at two angles of elevation are required: one corresponding to the elevation of the interference (illuminator of opportunity) and one corresponding to the elevation of the imaged area. The steering vectors at the latter elevation angle will be the most difficult to estimate due to the absence of dedicated calibration sources on the ground. This issue could be solved by using the available (point) scatterers in the SAR synthesised image as calibration sources.

8.2.5 Burst-mode interferometry

Interferometric SAR (InSAR) in burst-mode operation has been extensively studied in the monostatic case [78, 142]. Several experiments have demonstrated the feasibility such as DEM generation [31, 108, 143] or Moving Target Indicator (MTI) [144, 145]. However, bistatic InSAR using a transmitter operating in burst mode has not been demonstrated in open literature.

In monostatic SAR, repeat-pass interferogram formation from burst-mode data re-

quires the synchronisation of the burst patterns. This step is called azimuth scanning pattern synchronisation [78] meaning that the Doppler spectra of the two interferometric datasets must overlap: only the range lines that have counterparts in the other dataset are kept for further processing [146]. In the bistatic configuration studied in this thesis, this step is obviously not needed in the case of a continuous illumination of the scene.

The work so far gave encouraging 'proof of concept' results to perform bistatic burst-mode interferometry. In [147], the impact of the increase of the noise content in SAR images by the burst-mode resolution enhancement method has been studied leading to the conclusion that the phase error induced by the burst-mode resolution enhancement method has only a minor effect on the accuracy of height estimation at typical SNRs. Indeed, for the optimum implementation of the method, the decorrelation caused by the noise amplification is very limited as demonstrated in Section 7.4.

The developed receiver spent 5 years in the field making measurements of the considered area. Therefore, there is the possibility to perform multi-temporal analysis of the scene in a repeat-pass configuration. The incoherent averaging of the intensity images can reduce the speckle in the SAR image. If a deformation of the scene between two observations occurs, Differential Interferometric SAR (DInSAR) can be envisaged to monitor time-varying surface phenomena.

The multichannel configuration could also be exploited in a single-pass configuration. By horizontally aligning the antenna elements, the detection of moving targets can be envisaged using along-track interferometry. By vertically aligning the antenna elements, a DEM of the scene of interest could be obtained using across-track interferometry. The artificial point scatterer of known elevation generated by the bistatic transponder could play a key role in this regard.

Appendix A

Bistatic system description

A.1 Reception system

The passive receiver consists of four channels. During this work, the configuration of the receiver has evolved in terms of amplification gain, antennas and their orientation. Table A.2 lists the main characteristics of the used receive antennas. A detailed block diagram of the four-channel radar receiver is illustrated in Fig. A.1. The receiving system is a typical superheterodyne receiver with three main stages: RF reception and amplification, down-conversion to IF and sampling. As the C-band is occupied by other transmitters such as Wireless Fidelity (WiFi) or weather radar systems, a band-pass filter (BPF) is placed directly after the antenna. After amplification by a cascade of Low Noise Amplifiers (LNA), the signals are down-converted to an intermediate frequency and then low-pass filtered (LPF) to satisfy Nyquist-Shannon's sampling theorem. The local oscillator (LO) used in the down-conversion is programmable in order to be able to fit the signal of the different satellites in the bandwidth of the A/D card. They are then sampled at 100 MSamples/s using a 16-bit A/D card (AlazarTech ATS660) and finally digitally down-converted to baseband. The total measured gain of one chain is 70 dB. The acquisition system is depicted in Fig. A.3.

The details of all components are given in Table A.1.

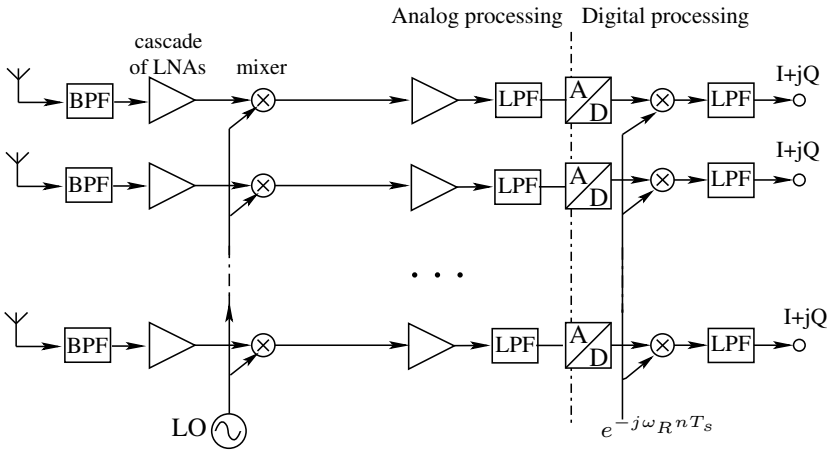

Figure A.1: Schematic block diagram of the receiver.

Component	Model	Manufacturer	Bandwidth (MHz)	Gain (dB)
Band-pass filter	TIC-5450B-110-01	Tech-Inter	5339 to 5470	-0.1
LNA 1,2	ZX60-542LN+	Minicircuit	4400 to 5400	24
LNA 3,4	ZX60-6013E	Minicircuit	20 to 6000	12
Mixer	ZMX-7GR	Minicircuit	3700 to 7000	-6
IF amplifier	ZHL-6A	Minicircuit	0.0025 to 500	24
Low-pass filter	SLP-50	Minicircuit	DC to 48	-1

Table A.1: Components used in one receiving channel.

Table A.2: Parameters of the receive antennas used in the experiments.

Parameters	Parabolic WiFi antenna	Patch WiFi antenna	Manufactured patch antenna
Model	TL-ANT5830B	PA-5000-12 / 18710.12	/
Manufacturer	TP-link	WiMo Antennen	Royal Military Academy
Gain, dBi	30	14	7.5
Polarisation	V	V	V
Beamwidth, degree	H:6 V:4	H:43 V:30	H:60 V:100
Front-back ratio, dB	> 30	> 20	15

Figure A.2 depicts the last version of the receiving system with one channel pointing to the satellite (channel 4) and three other channels pointing to the scene (channel 1 to 3). The antennas 3 and 4 are Commercial off-the-shelf (COTS) antennas (WiMo PA-5000-12) and antennas 1 and 2 are manufactured patch antennas which are described in Appendix A.2.

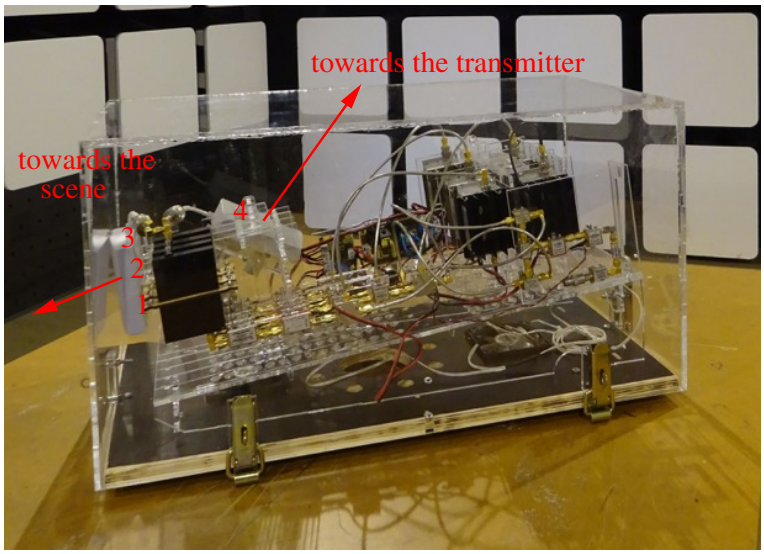

Figure A.2: Photograph of the latest version of the multichannel receiver.

A.2 Patch antenna element design

One of the configurations of the receiving system (Fig. A.4 (a)) consists of a microstrip-line feed patch antenna array (ULA) of four linear polarised elements separated by $\frac{\lambda}{2}$. This half-wavelength distance between the centres of the patch antennas was initially chosen to perform beamforming to mitigate the strong direct-path signal. Patch antennas (Fig. A.4 (b)) are attractive because of their ease of fabrication, small size and wide mainlobe. The manufactured patch antenna has a resonance frequency of approximately 5.4 GHz. Its large frequency bandwidth of 150 MHz is adequate to receive all illuminators of opportunity given in Table 2.1. Simulations using EMSS FEKO were performed in order to obtain the patch dimensions satisfying these requirements. As the impedance at the edge of the patch is much higher than 50Ω, quarter-wavelength transformers are used between patches and feeding transmission lines to match their impedances, avoiding power losses and reflections.

Figure A.3: Photograph of the transportable acquisition system.

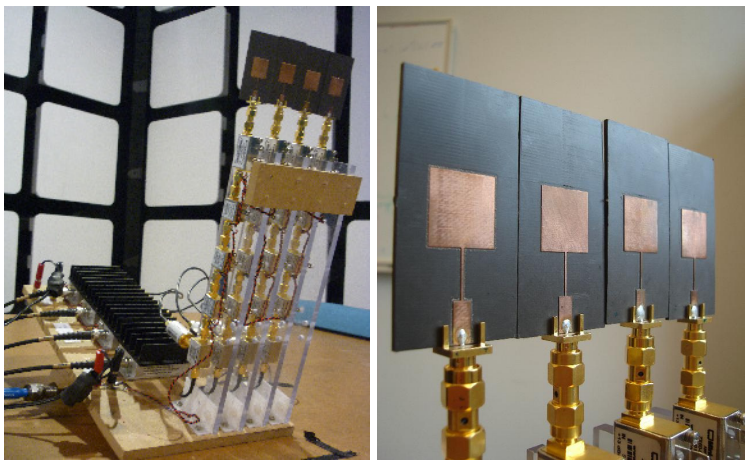

(a) (b)

Figure A.4: Receiver system with patch antenna array and RF amplifiers.

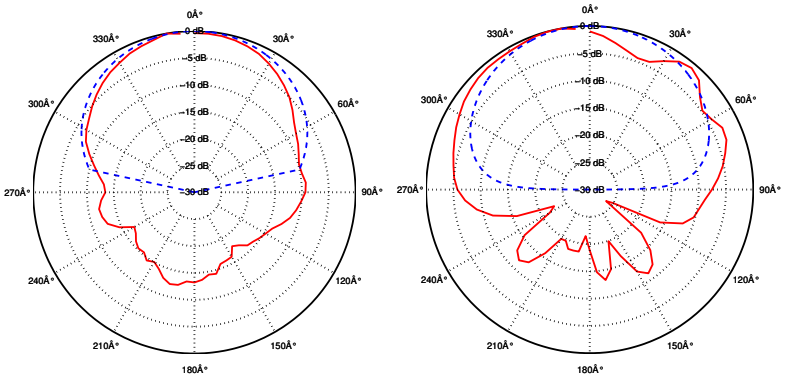

(a) (b)

Figure A.5: Measured (solid line) and theoretical (dashed line) (a) azimuth pattern and (b) elevation pattern of one patch antenna.

Figure A.5 illustrates the theoretical and the measured azimuth and elevation radiation patterns of a stand-alone patch antenna. The measurements were made in an anechoic chamber. The theoretical patterns, simulated under the assumption of infinite substrate, show wide mainlobes and no secondary lobes in both directions. Etching errors and finite-substrate effects can explain the radiation pattern perturbations [148]. The fact that one antenna element is placed in proximity to other elements will modify the antenna pattern and is not evaluated in this work.

It was decided to design each patch antenna on a different substrate to have the potential to increase the inter-element spacing. Furthermore, separated patch antennas offer the potential to orient the antennas in different directions. For instance, one antenna can point towards the illuminator of opportunity to retrieve the reference signal.

A.3 Performance prediction

A.3.1 Introduction

The starting point for prediction of PBR performance is the bistatic radar equation [1, Chapter 25]. For a single pulse, the received power at the antenna port is related to the transmitted power, P_T, by

$$P_R = \frac{P_T G_T}{4\pi R_T^2} \sigma_B \frac{1}{4\pi R_R^2} A_{eff} \frac{F_T^2 F_R^2}{L_T L_R} \tag{A.1}$$

where G_T is the transmit antenna gain, A_{eff} is the effective area of the receive antenna, σ_B is the target bistatic radar cross section, R_R is the target-to-receiver range,

R_T is the transmitter-to-target range. F_T and F_R are the pattern propagation factor for transmitter-to-target path and for target-to-receiver path, respectively. L_T and L_R denotes the transmit system and the receive system losses (> 1) respectively.

The thermal noise power, N_R, is given by

$$N_R = k_B T_0 B_n F \tag{A.2}$$

where $k_B = 1.38\ 10^{-23}$ Ws/K is Boltzmann's constant, $T_0 = 290$ K is the effective noise temperature, F is the noise factor of the receiver and B_n is the noise bandwidth of the receiver in Hertz. For a superheterodyne receiver, the noise bandwidth is approximately equal to the bandwidth of the intermediate frequency (IF) stages [1] and the overall noise figure of a receiver is primarily established by the noise figure of its first amplifying stage (LNA).

Consequently, the SNR at the receive antenna port before SAR processing, for a point target of radar cross section σ_B is given by

$$SNR_{point}^{raw} = \frac{P_R}{N_R} \tag{A.3}$$

and after SAR processing, by

$$SNR_{point}^{sar} = SNR_{point}^{raw} G_{processing} \tag{A.4}$$

with $G_{processing}$ the processing gain thanks to range and azimuth compression of SAR imaging.

In SAR imaging, a discussion on distributed targets is more appropriate. For distributed targets, the radar cross section can be expressed as

$$\sigma_B = \sigma_0 A_{cell} \tag{A.5}$$

with σ_0 the dimensionless scattering coefficient, or the clutter cross section per unit area of the illuminated surface and A_{cell} the raw data resolution cell, or clutter cell. Therefore, the SNR of distributed targets before SAR processing is given by

$$SNR_{dist} = \frac{P_T G_T A_{eff}}{(4\pi)^2 R_T^2 R_R^2} \sigma_0 A_{cell} \frac{F_T^2 F_R^2}{L_T L_R k_B T_0 B_n F} \tag{A.6}$$

Note that A_{cell} depends on the distance from the receiver. After SAR processing, the SNR improvement is counterbalanced by a shrinking of the resolution cell which is inversely proportional to $G_{processing}$. The SNR of distributed targets is thus unchanged after SAR synthesis.

A.3.2 Power calculations

To predict the performance of the receiving system, the strimap mode of the ENVISAT satellite (Image Mode 6) is considered. A summary of the fixed parameters used in the following calculations may be found in Table A.3. Before considering the signal levels of the direct-path and reflected signals (which are received on the same channel), it is useful to calculate a likely value for the thermal noise in the receiver. The thermal noise power is

$$N_R = k_B T_0 B_n F = 2.72\,10^{-13}\,W \equiv -95.65\,dBm \tag{A.7}$$

where the values are taken from Table A.3. The power density on the Earth's surface at the slant range distance R_T of $1010\,km$ is

$$P_d = \frac{P_T G_T}{4\pi R_T^2} = 2.35\,10^{-6}\,\frac{W}{m^2} \tag{A.8}$$

For a microstrip patch antenna, as the one described in Appendix A.2, the effective aperture can be taken in a first approximation 50% of the physical area of the patch, A_{phys}. The direct-signal received power is thus

$$P_{direct} = P_d\,A_{eff}\,\frac{F_T^2}{L_T} = 3.64\,10^{-10}\,W \equiv -64.39\,dBm \tag{A.9}$$

The surface of the resolution cell is computed with the parameters of the receive antenna as the area under the mainlobe of the receive antenna is smaller than that of the transmit antenna. The surface of the resolution cell, at a distance R_R of $500\,m$ from the receiver which is at a height of $30\,m$ above the ground and with a beamwidth θ_B of $30°$, is calculated as

$$A_{cell} = R_R\,\theta_B \frac{cT_p}{2\,sin(\theta_R)} = 1.0364\,10^6\,m^2 \tag{A.10}$$

with θ_R the angle between the reflected signal towards the receiver and the normal to the earth's surface and with T_p the duration of the transmitted pulse. This resolution cell is relatively large due to the large beamwidth of the current receive patch antenna. Assuming σ_0 equals to $-10\,dBm^2/m^2$, the reflected received power is given by

$$P_{reflected} = P_d\,\sigma_0\,A_{cell}\,\frac{1}{4\pi R_R^2}\,A_{eff}\,\frac{F_T^2 F_R^2}{L_T L_R} = 1.2\,10^{-11}\,W \equiv -79.2\,dBm \tag{A.11}$$

This reflected signal level is larger than the noise floor but lower than the direct-signal level which is $15\,dB$ larger. The front-back ratio of the receive antenna is $15\,dB$ and will partly reduce the strong direct-path signal.

This analysis is performed considering distributed targets at 500 m from the receiver. A typical measured reflected-to-direct signal ratio is $-50\ dB$ as measured by one surveillance channel. Note that this value depends on the geometry but also on the scene to be imaged. This would require a minimum dynamic range of the acquisition card of 10 bits[1].

Parameter	Value
P_T	$1365\ W$
G_T	$43.45\ dBi$
R_T	$1010\ km$
A_{phys}	$3.09\ cm^2$
σ_0	$-10\ dBm^2/m^2$
θ_B	$30°$
θ_R	$86.6°$
T_p	$26.3436\ \mu s$
B_n	$22\ MHz$ (LPF)
F	$1.9\ dB$ (LNA)
	+ $3\ dB$ (double-balanced mixer)
$G_{processing}$	$64\ dB$
F_T	$0\ dB$
F_R	$0\ dB$
L_T	$0.2\ dB$
L_R	$0\ dB$

Table A.3: Fixed-value parameters used in the power calculations.

A.3.3 Maximum detection range

The maximum detection range gives an idea to which range from the receiver a SAR image can be obtained and is given by

$$R_{R,max} = \sqrt{\frac{P_T G_T A_{eff} \sigma_0 A_{cell} F_T^2 F_R^2}{SNR_{dist,min}(4\pi)^2 R_T^2 L_T L_R k_B T_0 B_n F}} = 2353\ m \tag{A.12}$$

[1]This small dynamic range is partly due to the fact that the direct signal is received in the backlobe of the receive antenna.

A minimum value for the SNR after SAR processing of $10\ dB$ is assumed. This is calculated assuming F_T and F_R to be equal to 1, i.e. the target is illuminated by the peak of the antenna beam in each case. The transmitting system losses, L_T, may arise from atmospheric attenuation of the signal and the value of $0.2\ dB$ is assumed. The receiving system losses, L_R, are taken to be negligible. This distance can be increased by using a receive antenna with a higher gain such as the WiMo PA-5000-12.

Appendix B

Notable relations

B.1 Derivation of the shift in the azimuth direction

In BSAR, the instantaneous Doppler frequency is given by

$$\begin{aligned} f_{dop}(u) &= \frac{1}{2\pi}\frac{d\phi(u)}{du} \\ &= \frac{1}{2\pi}\frac{d}{du}(\frac{2\pi}{\lambda}R_{bi}(u)) \\ &= \frac{1}{\lambda}\frac{dR_{bi}(u)}{du} \\ &= \frac{1}{\lambda}\frac{d}{du}(R_T(u)+R_R) \end{aligned} \tag{B.1}$$

with u the (along track) azimuth time, $R_{bi}(u)$ the bistatic range history, R_T the range to the transmitter, R_R the range to the receiver and ϕ the phase history.

In the space-ground bistatic geometry considered in this thesis, the parabolic approximation (2.19) holds and one can expand $R_T(u)$ into a Taylor series expansion about the time of closest approach u_0. The bistatic range history of a patch located at the azimuth time u_0 can be written as

$$R_{bi}(u) \approx R_{T,0} + \frac{V^2(u-u_0)^2}{2R_{T,0}} + R_R \tag{B.2}$$

where $R_{T,0} = R_T(u_0)$. Therefore, the instantaneous Doppler frequency for a patch is

$$\begin{aligned} f_{dop}(u) &\approx \frac{V^2}{\lambda R_{T,0}}(u-u_0) \\ &\approx \frac{V^2}{\lambda R_{T,0}}u - \Delta f_{dop} \end{aligned} \tag{B.3}$$

with

$$\Delta f_{dop} = \frac{V^2}{\lambda R_{T,0}}u_0 \tag{B.4}$$

The second term, Δf_{dop}, is constant and can be interpreted as the shift in Doppler encountered by a patch at u_0 relative to a patch at $u = 0$. A shift in Doppler frequency

is thus equivalent to a linear phase term and causes a shift in the azimuth-slant range plane along the azimuth direction but makes no change to the waveform. The temporal shift along the azimuth direction is given by

$$u_0 = \frac{\Delta f_{dop} \lambda R_{T,0}}{V^2} \tag{B.5}$$

and corresponds to a spatial shift in azimuth equal to

$$\begin{aligned} \Delta y &= u_0 V \\ &= \frac{\Delta f_{dop} \lambda R_{T,0}}{V} \end{aligned} \tag{B.6}$$

B.2 Alternative expression of a non-baseband LFM signal

The output of the matched filtering of a baseband LFM signal gives one complex number, the phase of which is equal to the phase of this LFM signal. In this section, we want to relate a non-zero centre frequency of a LFM signal with the phase of the output of the matched filtering of the considered LFM signal.

A non-baseband LFM signal with a centre frequency equal to δf can be written

$$e^{j[\pi\alpha(t-\tau_x)^2+2\pi\delta f t+\phi_1]} \tag{B.7}$$

with τ_x the propagation delay and ϕ_1 the initial phase. According to the auto-ambiguity function of a LFM signal depicted in Fig. 2.5, a frequency shift of a LFM signal corresponds to a shift in time.

To emphasise the effect of a non-zero centre frequency, (B.7) can be rewritten under the following form

$$e^{j[\pi\alpha(t-\tau-\tau_x)^2+\phi_x]} \tag{B.8}$$

which, equating the phase terms of (B.7) and (B.8), yields

$$\begin{aligned} e^{j[\pi\alpha(t-\tau_x)^2+2\pi\delta f t+\phi_1]} &= e^{j[\pi\alpha(t-\tau-\tau_x)^2+\phi_x]} \\ \phi_1 + 2\pi\delta f t &= \phi_x + \pi\alpha\tau^2 + 2\pi\alpha\tau_x\tau - 2\pi\alpha\tau t \end{aligned} \tag{B.9}$$

$$\Longrightarrow \begin{cases} \phi_x &= \phi_1 - \pi\alpha\tau^2 - 2\pi\alpha\tau_x\tau \\ \delta f &= -\alpha\tau \end{cases} \tag{B.10}$$

Therefore,

$$e^{j[\pi\alpha(t-\tau_x)^2+2\pi\delta f t+\phi_1]} = e^{j[\pi\alpha(t+\frac{\delta f}{\alpha}-\tau_x)^2+\phi_1-\pi\frac{\delta f^2}{\alpha}+2\pi\tau_x\delta f]}. \tag{B.11}$$

From (B.11), it can be concluded that a shift in frequency δf corresponds to a shift $-\alpha\tau$ in time as illustrated in the auto-ambiguity function of a LFM signal depicted in Fig. 2.5 but also a phase term appears equal to $-\pi\alpha\tau^2 - 2\pi\alpha\tau_x\tau$ which is important in the synchronisation algorithm described in Section 4.3.3.

Appendix C

Scenario

C.1 Bistatic geometry

The locations of the experiment include two rooftops in Brussels: one in the Royal Military Academy and one in the Military Hospital. In both bistatic geometries, the transmitter and the receiver are pointing in the same direction (East), i.e. the bistatic angle is close to zero (quasi-monostatic geometry). Therefore, the bistatic slant-range resolution (2.20) is close to the monostatic slant-range resolution. This corresponds to the ascending pass of the satellite. Figure C.1 depicts the geometry of both scenarios.

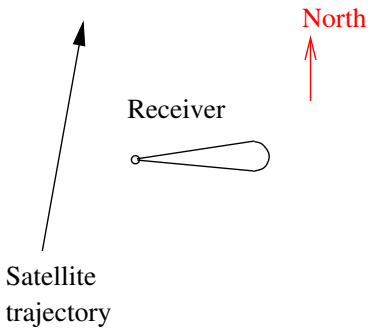

Figure C.1: Bistatic geometry of the experiments.

C.2 Royal Military Academy scenario

In this scenario, the receiving system is sited on the roof of one of the buildings of the Royal Military Academy in Brussels. Table C.1 lists the parameters of this scenario.

The photograph of the receiver's location is depicted in Fig. C.2 and Fig. C.3 illustrates the urban imaged scene.

Table C.1: Parameters of the Royal Military Academy scenario.

Parameters	Value
Antenna pointed to transmitter	PA-5000-12 / 18710.12
Antenna pointed to the scene	Manufactured patch antenna
Polarisation	VV
Receiver position	N 50° $50'$ $38.16''$
	E 4° $23'$ $34.2''$
Receiver altitude above sea level	101 m
Scene altitude above sea level	87 m

C.3 Military Hospital scenario

In this scenario, the receiving system is sited on the roof of one of the buildings of the Military Hospital in Brussels which is higher relative to the imaged area than that of the Royal Military Academy. Table C.2 lists the parameters of this scenario.

Table C.2: Parameters of the Military Hospital scenario.

Parameters	Value
Antenna pointed to transmitter	PA-5000-12 / 18710.12
Antenna pointed to the scene	PA-5000-12 / 18710.12
Polarisation	VV
Receiver position	N 50° $54'$ $22.74''$
	E 4° $23'$ $25.5''$
Receiver altitude above sea level	81 m
Scene altitude above sea level	49 m
Transponder position	N 50° $54'$ $20.94''$
	E 4° $23'$ $38.22''$

The photograph of the receiver's location is depicted in Fig. C.4 and Fig. C.5 illustrates the imaged scene. The position of the "Buda" bridge and the position of the transponder are also indicated.

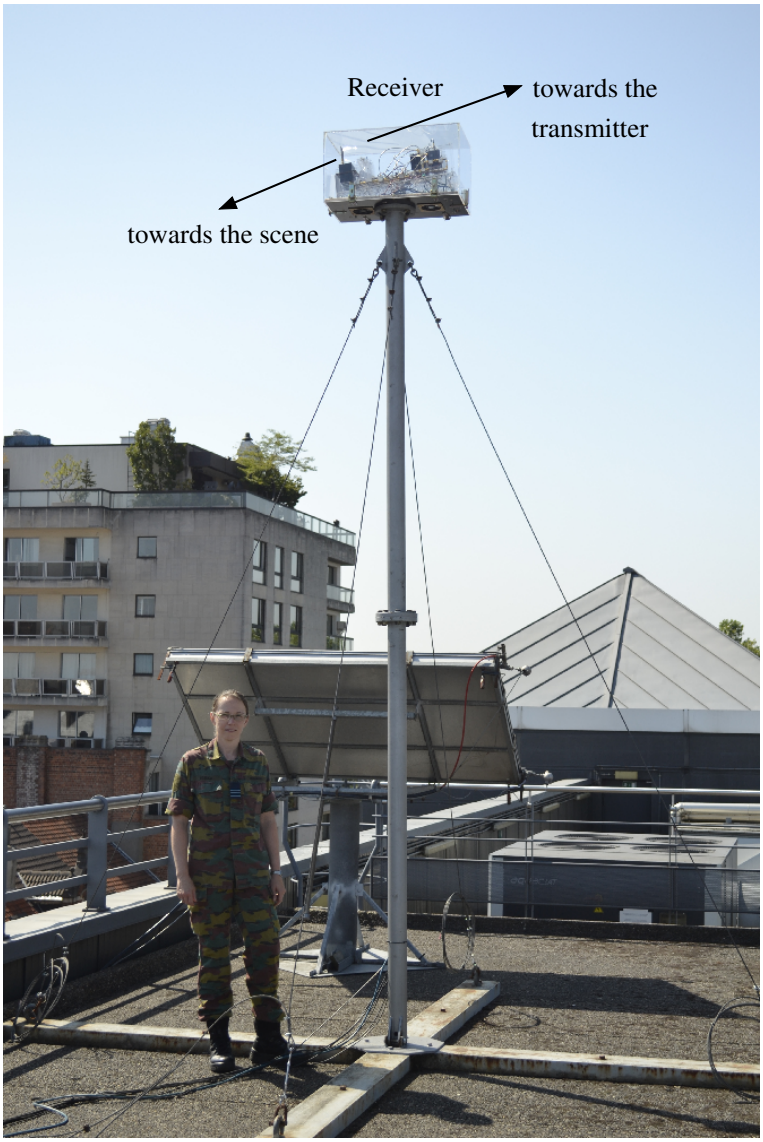

Figure C.2: Photograph of the receiver at the Royal Military Academy located on a mast having a height of 4 m.

Figure C.3: Photograph of the imaged area at the Royal Military Academy taken from the receiver position.

Figure C.4: Photograph of the receiver at the Military Hospital.

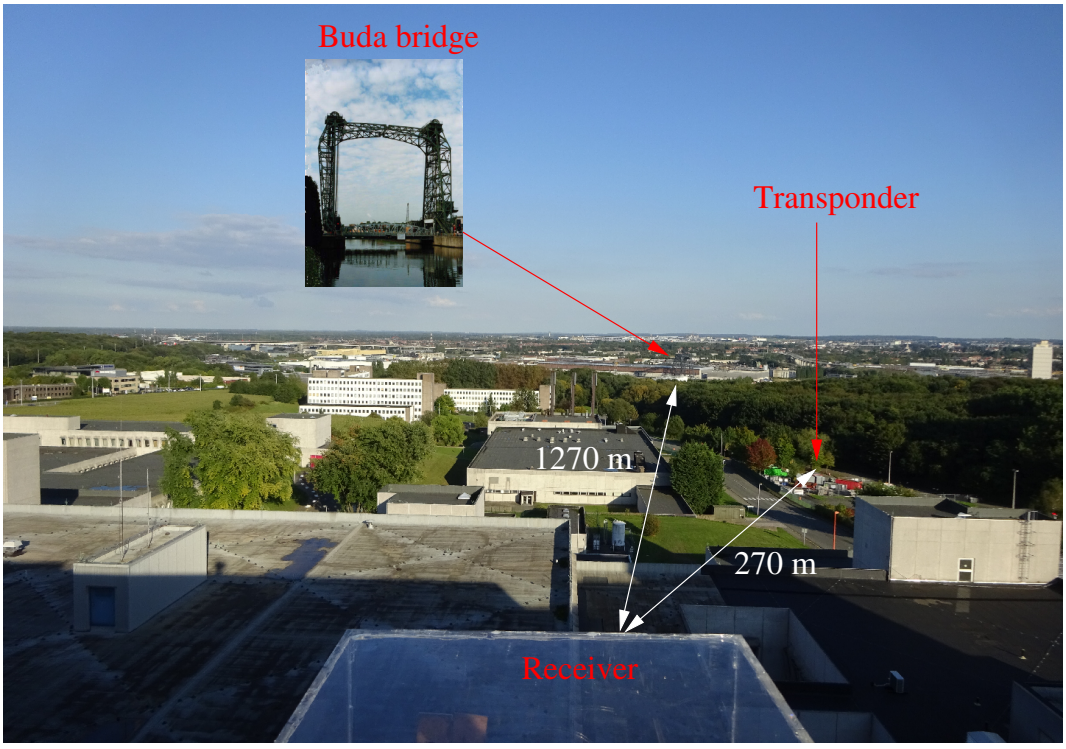

Figure C.5: Photograph of the imaged area at the Military Hospital.

Appendix D

Description of the bistatic transponder

Also deployed during these trials was an active bistatic transponder located at 270 m from the receiver. This transponder consists of two WiFi antennas separated by an amplification stage consisting of three ZX60-542LN+ followed by one ZX60-6013E which provide 77 dB gain. A block diagram of the transponder is illustrated in Fig. D.3. As depicted in Fig. D.1, one parabolic antenna (TL-ANT5830B) is directed towards the receiver and another antenna (PA-5000-12) towards the transmitter. The parameters of the antennas are listed in Table A.2.

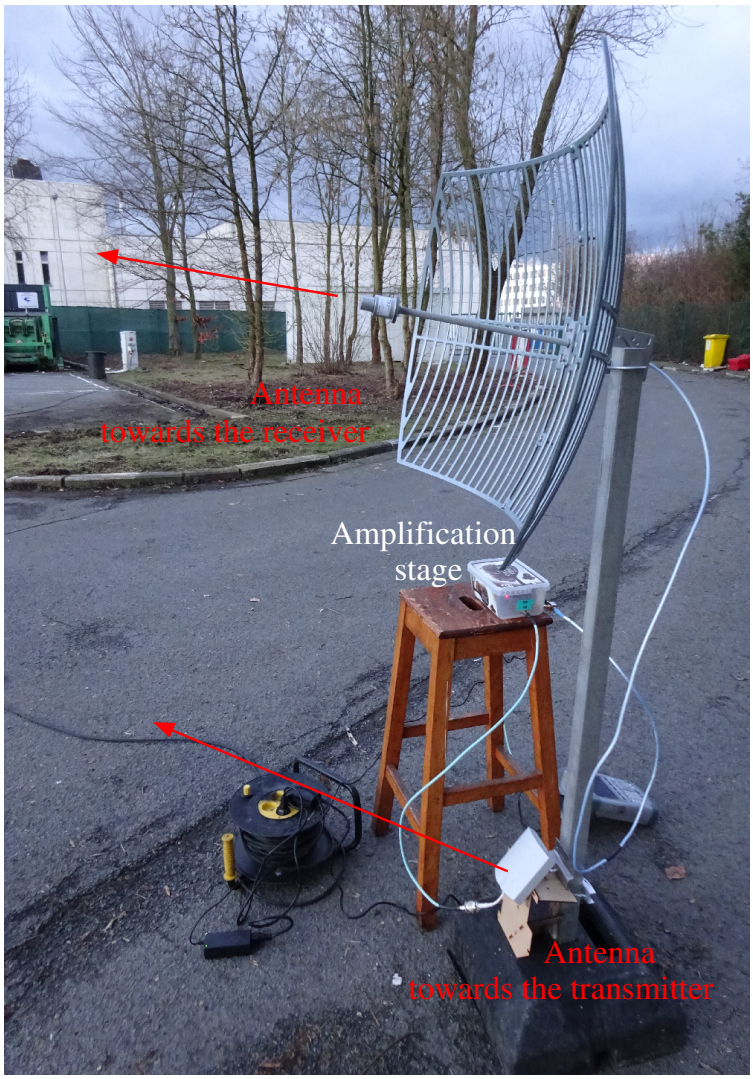

Figure D.1: Photograph of the developed active bistatic transponder.

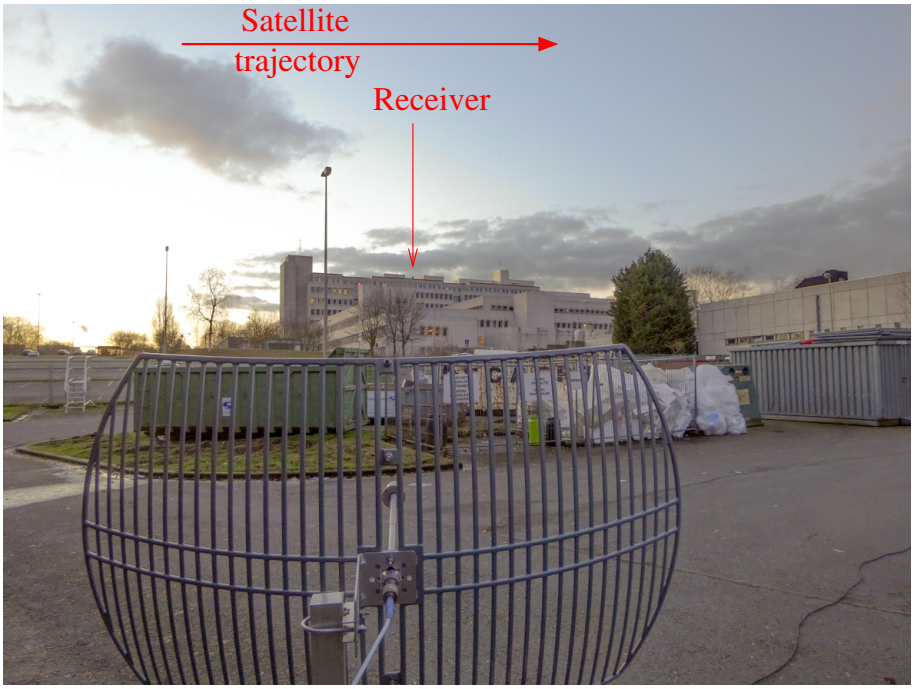

Figure D.2: Photograph of the receiver system taken from the transponder position.

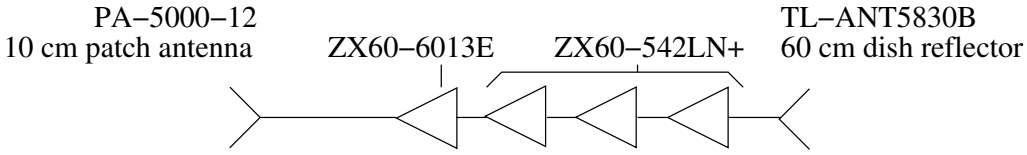

Figure D.3: Schematic block diagram of the transponder.

Bibliography

[1] M. Skolnik, *Radar Handbook*. NY: McGraw-Hill, 1970.

[2] J. Way, "The evolution of synthetic aperture radar systems and their progression to the EOS SAR," *IEEE Transactions on Geoscience and Remote Sensing*, vol. 29, no. 6, 1991.

[3] J. C. Curlander and R. N. McDonough, *Synthetic Aperture Radar, Systems and Signal Processing*. NY: John Wiley and Sons, 1991.

[4] "STO-TR-SET-102 - High resolution space-borne SAR systems for geospatial intelligence," tech. rep., Science and Technology Organization, 2012.

[5] E. Attema, P. Bargellini, P. Edwards, G. Levrini, S. Lokas, L. Moeller, B. Rosich-Tell, P. Secchi, R. Torres, M. Davidson, and P. Snoeij, "Sentinel-1: The radar mission for GMES operational land and sea services," *ESA Bulletin*, no. 131, 2007.

[6] N. J. Willis and H. D. Griffiths, *Advances in Bistatic Radar*. Raleigh, NC: SciTech Publishing, 2007.

[7] P. Howland, D. Maksmiuk, and G. Reitsma, "FM radio based bistatic radar," *IEE Proceedings – Radar, Sonar and Navigation*, vol. 152, no. 3, 2005.

[8] M. Kubica, V. Kubica, X. Neyt, J. Raout, S. Roques, and M. Acheroy, "Optimum target detection using illuminators of opportunity," in *Proceedings of IEEE Radar Conference*, (Verona, NY), pp. 417–424, Apr. 2006.

[9] D. W. O'Hagan, A. Capria, D. Petri, V. Kubica, M. Greco, F. Berizzi, and A. G. Stove, "Passive Bistatic Radar (PBR) for harbour protection applications," in *Proceedings of IEEE Radar Conference*, (Atlanta,GA), pp. 446–450, May 2012.

[10] H. Griffiths and N. Long, "Television-based bistatic radar," *IEE Proceedings*, vol. 133, no. 7, pp. 649–657, 1986.

[11] M. Cherniakov, D. Nezlin, and K. Kubik, "Air target detection via bistatic radar based on LEOs communication signals," *IEE Proceedings – Radar, Sonar and Navigation*, vol. 149, no. 1, pp. 33–38, 2002.

[12] M. Cherniakov, "Space-surface bistatic synthetic aperture radar - prospective and problems," in *Proceedings of RADAR 2002*, (Edinburgh, UK), pp. 22–26, IEE, Oct. 2002.

[13] J. Palmer, S. Palumbo, A. Summers, D. Merrett, and S. Howard, "DSTO's experimental geosynchronous satellite based PBR," in *IEEE International Radar Conference*, (Bordeaux, France), pp. 1–6, Oct. 2009.

[14] G. Yates, A. M. Horne, A. P. Blake, R. Middleton, and D. B. Andre, "Bistatic SAR image formation," in *EUSAR Conference*, vol. 2, (Ulm, Germany), pp. 581–584, 2004.

[15] P. Dubois-Fernandez, H. Cantalloube, O. Ruault du Plessis, M. Wendler, B. Vaizan, C. Coulombeix, D. Heuze, and G. Krieger, "Analysis of bistatic scattering behavior of natural surfaces," in *EUSAR Conference*, (Ulm, Germany), pp. 573–576, May 2004.

[16] P. Dubois-Fernandez, H. Cantalloube, B. Vaizan, G. Krieger, R. Horn, M. Wendler, and V. Giroux, "ONERA-DLR bistatic SAR campaign: planning, data acquisition, and first analysis of bistatic scattering behaviour of natural and urban targets," *IEE Proceedings – Radar, Sonar and Navigation*, vol. 153, pp. 214–223, June 2006.

[17] H. Cantalloube, M. Wendler, V. Giroux, P. Dubois-Fernandez, and R. Horn, "A first bistatic airborne SAR interferometry experiment-Preliminary results," in *IEEE Sensor Array and Multichannel Signal Processing Workshop*, 2004.

[18] M. Rodriguez-Cassola, S. V. Baumgartner, G. Krieger, and A. Moreira, "Bistatic TerraSAR-X/F-SAR spaceborne-airborne SAR experiment: description, data

processing, and results," *IEEE Transactions on Geoscience and Remote Sensing*, vol. 48, pp. 781–794, Feb. 2010.

[19] I. Walterscheid, T. Espeter, A. R. Brenner, J. Klare, J. Ender, H. Nies, R. Wang, and O. Loffeld, "Bistatic SAR experiments with PAMIR and TerraSAR-X-Setup, processing, and image results," *IEEE Transactions on Geoscience and Remote Sensing*, vol. 48, pp. 3268–3279, Aug. 2010.

[20] G. Krieger, I. Hajnsek, K. P. Papathanassiou, M. Younis, and A. Moreira, "Interferometric SAR missions employing formation flying," *Proceedings of the IEEE*, vol. 98, pp. 816–843, May 2010.

[21] N. Gebert, B. Carnicero Dominguez, M. Davidson, M. Diaz Martin, and P. Silvestrin, "SAOCOM-CS - A passive companion to SAOCOM for single-pass L-band SAR interferometry," in *Proc. EUSAR conference*, pp. 1–4, June 2014.

[22] A. Goh, M. Preiss, N. Stacy, and D. Gray, "The Ingara bistatic SAR upgrade: first results," in *IEEE International Radar conference*, pp. 329–334, Sept. 2008.

[23] H. D. Griffiths, C. J. Baker, J. Baubert, N. Kitchen, and M. Treagust, "Bistatic radar using satellite-borne illuminators," in *IEEE International Conference RADAR 02*, (Edinburgh, UK), pp. 1–5, Oct. 2002.

[24] A. P. Whitewood, C. J. Baker, and H. D. Griffiths, "Bistatic radar using space-borne illuminator," in *IET International Radar conference*, (Edinburgh, UK), Oct. 2007.

[25] J. Sanz-Marcos, P. Lopez-Decker, J. J. Mallorqui, A. Aguasca, and P. Prats, "SABRINA: A SAR bistatic receiver for interferometric applications," *IEEE Geoscience and Remote Sensing Letters*, vol. 4, pp. 307–311, Apr. 2007.

[26] P. Samczynski and K. Kulpa, "Passive SAR imaging using a satellite pulsed radar as an illuminator of opportunity," in *Radar Symposium (IRS)*, (Berlin, Germany), pp. 157–161, 2012.

[27] S. Buckreuss, "The missions TerraSAR-X and TanDEM-X: Status, challenges,

future perspectives," in *General Assembly and Scientific Symposium*, (Istanbul, Turkey), 2011.

[28] M. Antoniou and Z. Zeng, "Experimental demonstration of passive BSAR imaging using navigation satellites and a fixed receiver," *IEEE Geoscience and Remote Sensing Letters*, vol. 9, no. 3, pp. 477–481, 2012.

[29] L. Cazzani, C. Colesanti, D. Leva, G. Nesti, C. Prati, F. Rocca, and D. Tarchi, "A ground-based parasitic SAR experiment," in *Proceedings of the IEEE Geoscience and Remote Sensing Symposium*, vol. 38, (Hamburg, Germany), pp. 2132–2141, 1999.

[30] P. Sacco, M. Battagliere, and A. Coletta, "COSMO-SkyMed mission status: Results, lessons learnt and evolutions," in *IGARSS 2015. Geoscience and Remote Sensing Symposium*, pp. 207–210, 2015.

[31] H. Nies, F. Behner, S. Reuter, O. Loffeld, and R. Wang, "SAR Experiments in a bistatic hybrid configuration for generating PolInSAR data with TerraSAR-X illumination," in *EUSAR Conference*, (Aachen, Germany), pp. 994–997, 2010.

[32] A. Currie and M. A. Brown, "Wide-swath SAR," *Proc. Inst. Elec. Eng. F*, vol. 139, no. 2, pp. 123–135, 1992.

[33] R. Moore, J. Claassen, and Y. Lin, "Scanning spaceborne synthetic aperture radar with integrated radiometer," *IEEE Transactions on Aerospace and Electronic Systems*, vol. 17, pp. 410–421, May 1981.

[34] F. Li and W. Johnson, "Ambiguities in spaceborne synthetic aperture radar systems," *IEEE Transactions on Aerospace and Electronic Systems*, vol. 19, no. 3, pp. 389–397, 1983.

[35] I. Cumming and F. Wong, *Digital Processing of Synthetic Aperture Radar Data: Algorithms and Implementation*. Artech House, 2005.

[36] S. M. Kay, *Fundamentals of Statistical Signal Processing — Estimation Theory*. Englewood Cliffs, NJ: Prentice-Hall, 1993.

[37] R. Klemm, *Principles of Space-Time Adaptive Processing*. UK: The Institution of Electrical Engineers (IEE), 2002.

[38] J. R. Guerci, *Space-Time Adaptive Processing for Radar*. Norwood, MA: Artech House, 2003.

[39] H. L. Van Trees, *Detection, Estimation and Modulation theory — Part III: Radar-Sonar Signal Processing and Gaussian Signals in Noise*. NY: John Wiley and Sons, 1971.

[40] M. Y. Jin, "PRF ambiguity determination for RADARSAT ScanSAR system," in *IGARSS '94. Geoscience and Remote Sensing Symposium*, vol. 4, pp. 1964–1966, Aug. 1994.

[41] K. Tomiyasu, "Conceptual performance of a satellite borne, wide swath synthetic aperture radar," *IEEE Transactions on Geoscience and Remote Sensing*, vol. GE-19, pp. 108–116, Apr. 1981.

[42] C. Wilson and D. G. Corr, "SAR data processing techniques and operational considerations for ScanSAR systems," in *IGARSS '91. 1991 International Geoscience and Remote Sensing Symposium*, pp. 271–274, 1991.

[43] C. Oliver and S. Quegan, *Understanding Synthetic Aperture Radar Images*. Raleigh, NC: SciTech Publishing, 2004.

[44] European Space Agency, "ENVISAT ASAR Product Handbook," tech. rep., 2004.

[45] F. De Zan and A. Monti Guarnieri, "TOPSAR: Terrain Observation by Progressive Scans," *IEEE Transactions on Geoscience and Remote Sensing*, vol. 44, no. 9, pp. 2352–2360, 2006.

[46] D. D'Aria, D. Giudici, F. De Zan, A. M. Guarnieri, and F. Rocca, "Burst-mode SAR's for wide-swath surveys," *Canadian Journal of Remote Sensing*, vol. 33, pp. 27–38, 2007.

[47] G. Davidson, V. Mantle, R. Bernhard, D. Williams, and D. Geudtner, "Implementation Of Tops mode on RadarSAT-2 in support of the Sentinel-1 mission," in *ESA Living Planet Symposium*, (Edinburgh, UK), 2013.

[48] N. Miranda, B. Rosich, P. Meadows, K. Haria, D. Small, A. Schubert, M. Lavalle, F. Collard, H. Johnsen, A. M. Guarnieri, and . D. D'Aria, "The ENVISAT ASAR mission: a look back at 10 years of operation," in *ESA Living Planet Symposium*, (Edinburgh, UK), Sept. 2013.

[49] C. Livingstone, I. Sikaneta, C. Gierull, S. Chiu, and P. Beaulne, "RADARSAT-2 system and mode description," tech. rep., MDA, 2014.

[50] "Sentinel-1 Product Definition," tech. rep., MDA, 2011.

[51] N. J. Willis, *Bistatic Radar*. Norwood, MA: Artech House, 1991.

[52] F. R. Hoots and R. L. Roehrich, "Models for propagation of NORAD element sets," *Spacetrack Report 3*, 1980.

[53] J. Ender, "A step to bistatic SAR processing.," in *Proceedings of the EUSAR Conference*, (Ulm, Germany), pp. 359–363, 2004.

[54] T. Zeng, M. Cherniakov, and T. Long, "Generalized approach to resolution analysis in BSAR," *IEEE Trans. on Aerospace and Electronics Systems*, vol. 41, Apr. 2005.

[55] J. L. Auterman, "Phase stability requirements for a bistatic SAR," in *IEEE National Radar Conference*, (Atlanta,GA), pp. 48–52, 1984.

[56] W. Carrara, R. Majewski, and R. Goodman, *Spotlight Synthetic Aperture Radar: Signal Processing Algorithms*. Artech House, 1995.

[57] W.-Q. Wang, "GPS-based time & phase synchronization processing for distributed SAR," *IEEE Trans. on Aerospace and Electronics Systems*, vol. 45, no. 3, pp. 1040–1051, 2009.

[58] A. M. Horne and G. Yates, "Bistatic synthetic aperture radar," in *Proceedings of RADAR 02*, (Edinburgh, UK), pp. 6–10, 2002.

[59] E. Cristofani, V. Kubica, and X. Neyt, "A multibeam opportunistic SAR system," in *Proceedings of the IEEE SP Symposium on Information Theory and Signal Processing*, (Brussels, BE), May 2011.

[60] Y. Shao, R. Wang, Y. Deng, K. Liu, R. Chen, G. Liu, T. Balz, and O. Loffeld, "Error analysis of bistatic SAR imaging and stereoscopy bistatic SAR," *IEEE Trans. on Geoscience and Remote Sensing*, vol. 51, no. 8, pp. 4518–4543, 2013.

[61] R. Wang, Y. Deng, Z. Zhang, Y. Shao, J. Hou, G. Liu, and X. Wu, "Double-channel bistatic SAR system with spaceborne illuminator for 2-D and 3-D SAR remote sensing," *IEEE Transactions on Geoscience and Remote Sensing*, vol. 51, pp. 4496–4507, Aug. 2013.

[62] P. Lopez-Dekker, J. J. Mallorquí, P. Serra-Morales, and J. Sanz-Marcos, "Phase synchronization and doppler centroid estimation in fixed receiver bistatic SAR systems," *IEEE Transactions on Geoscience and Remote Sensing*, vol. 46, no. 11, pp. 3459–3471, 2008.

[63] K. Natroshvili and O. Loffeld, "Comparison of bistatic SAR focusing approaches," in *6th European Conference on Synthetic Aperture Radar*, (Dresden, Germany), 2006.

[64] V. Kubica, X. Neyt, and H. D. Griffiths, "Along-track resolution enhancement for bistatic SAR imaging in burst-mode operation," *IEEE Transactions on Aerospace and Electronic Systems*, 2016.

[65] D. D'Aria, A. M. Guarnieri, and F. Rocca, "Focusing bistatic synthetic aperture radar using dip move out," *IEEE Trans. on Geoscience and Remote Sensing*, vol. 42, pp. 1362–1376, July 2004.

[66] A. Monti Guarnieri and F. Rocca, "Reduction to monostatic focusing of bistatic or motion uncompensated SAR surveys," *IEE Proceedings – Radar, Sonar and Navigation*, vol. 153, no. 3, pp. 199–207, 2006.

[67] M. Soumekh, *Synthetic Aperture Radar Signal Processing with Matlab algorithms*. Wiley-Interscience, 1999.

[68] O. Loffeld, H. Nies, V. Peters, and S. Knedlik, "Models and useful relations for bistatic SAR processing," in *Proc. of the IEEE Int. Geoscience and Remote Sensing Symposium*, vol. 3, (Toulouse, France), pp. 1442–1445, July 2003.

[69] K. Natroshvili, O. Loffeld, H. Nies, and A. M. Ortiz, "First steps to bistatic focusing," in *Proc. of the IEEE Int. Geoscience and Remote Sensing Symposium*, vol. 2, pp. 1072–1076, July 2005.

[70] J. Sanz-Marcos, P. Prats, J. J. Mallorqui, and A. Aguasca, "A subaperture range-Doppler processor for bistatic fixed-receiver SAR," in *EUSAR Conference*, (Dresden, Germany), 2006.

[71] M. Antoniou, M. Cherniakov, and C. Hu, "Space-surface bistatic SAR image formation algorithms," *IEEE Transactions on Geoscience and Remote Sensing*, vol. 47, no. 6, pp. 1827–1843, 2009.

[72] F. Wong and T. Yeo, "New applications of nonlinear chirp scaling in SAR data processing," *IEEE Trans. on Geoscience and Remote Sensing*, vol. 39, no. 5, pp. 946–953, 2001.

[73] J. Sanz-Marcos, P. Prats, and J. J. Mallorqui, "Bistatic fixed-receiver parasitic SAR processor based on the back-propagation algorithm," in *Proceedings of the IEEE International Geoscience and Remote Sensing Symposium*, vol. 2, (Seoul, Korea), pp. 1056–1059, July 2005.

[74] D. Munson, J. O'brien, and W. K. Jenkins, "A tomographic formulation of spotlight-mode synthetic aperture radar," *IEEE Proceedings*, vol. 71, no. 8, pp. 917–925, 1983.

[75] Y. Ding and D. Munson, "A fast back-projection algorithm for bistatic SAR imaging," in *Image Processing*, vol. 2, pp. 449–452, 2002.

[76] A. Monti-Guarnieri and P. Guccione, "Optimal 'focusing' for low resolution ScanSAR," *IEEE Transactions on Geoscience and Remote Sensing*, vol. 39, no. 3, pp. 479–491, 2001.

[77] R. Bamler and M. Eineder, "ScanSAR processing using standard high precision SAR algorithms," *IEEE Transactions on Geoscience and Remote Sensing*, vol. 34, pp. 212–218, Jan. 1996.

[78] J. Holzner and R. Bamler, "Burst-mode and ScanSAR interferometry," *IEEE Transactions on Geoscience and Remote Sensing*, vol. 40, no. 9, pp. 1917–1934, 2002.

[79] A. P. Whitewood, *Bistatic Radar using a Spaceborne Illuminator*. PhD thesis, University College London, 2006.

[80] V. Kubica, R. Hock, E. Cristofani, and X. Neyt, "Strategies for the calibration of an array of patch antennas in passive bistatic SAR imaging," in *Proceedings of IEEE Radar Conference*, (Kansas City, MO), May 2011.

[81] D. G. Manolakis and J. G. Proakis, *Digital Signal Processing*. USA: Prentice Hall International, 1996.

[82] V. Kubica, E. Cristofani, and X. Neyt, "Strategies for mitigating the strong direct path signal in passive bistatic SAR imaging," in *Proceedings of the IEEE SP Symposium on Information Theory and Signal Processing*, (Brussels, BE), May 2011.

[83] K. Kulpa, P. Samczynski, M. Malanowski, L. Maslikowski, and V. Kubica, "The use of CLEAN processing for passive SAR image creation," in *Proceedings of IEEE Radar Conference*, (Ottawa, Ontario, Canada), May 2013.

[84] A. Tailliez, X. Neyt, and V. Kubica, "Removal of direct path interference with CLEAN Algorithm in passive SAR imaging," in *Proceedings of the URSI 2012 Benelux Forum*, (Brussels, BE), p. 43, Sept. 2012.

[85] G. Krieger, A. Moreira, H. Fiedler, I. Hajnsek, M. Werner, M. Younis, and M. Zink, "TanDEM-X: A satellite formation for high-resolution SAR interferometry," *IEEE Transactions on Geoscience and Remote Sensing*, vol. 45, no. 11, pp. 3317–3341, 2007.

[86] J. Salzman, D. Akamine, R. Lefevre, and J. Kirk, J.C., "Interrupted synthetic aperture radar (SAR)," in *IEEE Aerospace and Electronic Systems Magazine*, vol. 17, pp. 117–122, IEEE, 2002.

[87] I. Stojanovic, W. C. Karl, and L. Novak, "Reconstruction of interrupted SAR imagery for persistent surveillance change detection," *SPIE, Algorithms for Synthetic Aperture Radar Imagery*, vol. 8394, 2012.

[88] I. Stojanovic, W. C. Karl, and M. Cetin, "Compressed sensing of mono-static and multi-static SAR," in *Proceedings of SPIE*, vol. 7337, 2009.

[89] G. Rilling, C. Du, M. Davies, and B. Mulgrew, "Processing SAR data with gaps in the aperture: A compressed sensing perspective," in *International Conference, Synthetic aperture sonar and synthetic aperture radar*, (Italy), 2010.

[90] R. Tough, K. Ward, and P. Shepherd, "Modelling and enhancement of interrupted synthetic aperture radar imagery," *Radar, Sonar and Navigation, IET*, vol. 1, pp. 407–413, 2007.

[91] M. Pinheiro, M. Rodriguez-Cassola, and P. Prats-Iraola, "Reconstruction of coherent pairs of synthetic aperture radar data acquired in interrupted mode," *IEEE Transactions on Geoscience and Remote Sensing*, vol. 53, no. 4, pp. 1876–1893, 2015.

[92] S. M. Kay, *Modern Spectral Estimation: Theory and Application*. Prentice-Hall, 1988.

[93] E. Larsson and P. Stoica, "SAR image construction from gapped phase-history data," in *IEEE International Conference on Image Processing*, vol. 3, (Thessaloniki, Greece), pp. 608–611, Oct. 2001.

[94] E. Larsson, P. Stoica, and J. Li, "Amplitude spectrum estimation for two-dimensional gapped data," *IEEE Transactions on Signal Processing*, vol. 50, no. 6, pp. 1343–1354, 2002.

[95] P. J. S. G. Ferreira, "Digital spectral analysis with applications interpolation and

the discrete Papoulis-Gerchberg algorithm," *IEEE Transactions on Signal Processing*, vol. 42, no. 10, pp. 2596–2606, 1994.

[96] D. Donoho, "Compressed sensing," *IEEE Transactions on Information Theory*, vol. 52, pp. 1289–1306, Apr. 2006.

[97] M. Tello Alonso, P. López-Dekker, and J. J. Mallorquí, "A Novel Strategy for Radar Imaging Based on Compressive Sensing," *IEEE Trans. on Geoscience and Remote Sensing*, vol. 48, no. 12, pp. 4285–4295, 2010.

[98] S. Kelly, C. Du, G. Rilling, and M. Davies, "Advanced Image Formation and Processing of Partial SAR Data," *IET Signal Processing*, vol. 6, no. 5, pp. 511–520, 2012.

[99] R. Baraniuk and P. Steeghs, "Compressive radar imaging," in *IEEE Radar Conference*, pp. 128–133, Apr. 2007.

[100] M. Herman and T. Strohmer, "High-resolution radar via compressed sensing," *IEEE Transactions on Signal Processing*, vol. 57, no. 6, pp. 2275–2284, 2009.

[101] W. S. Li Jun, Xing Mengdao, "Application of compressed sensing in sparse aperture imaging of radar," in *2nd Asian-Pacific Conference on SAR*, pp. 651–655, 2009.

[102] W. W. Wang, G. S. Liao, and S. Q. Zhu, "A ScanSAR imaging method using compressive sensing," in *IET International Radar Conference*, 2012.

[103] D. Blacknell and H. Griffiths, *Radar Automatic Target Recognition (ATR) and Non-Cooperative Target Recognition (NCTR)*. IET Digital Library, 2013.

[104] E. Van den Berg and M. Friedlander, "SPGL1: A solver for large-scale sparse reconstruction," 2007.

[105] S. Mallat, *A Wavelet Tour of Signal Processing*. San Diego, CA, USA: Academic Press, 1998.

[106] G. Cui, J. Liu, H. Li, and B. Himed, "Signal detection with noisy reference for passive sensing," *Signal processing*, vol. 108, pp. 389–399, 2015.

[107] G. Krieger, M. R. Cassola, M. Younis, and R. Metzig, "Impact of oscillator noise in bistatic and multistatic SAR," in *Proceedings of the IEEE International Geoscience and Remote Sensing Symposium*, (Seoul, Korea), pp. 1043–1046, 2005.

[108] S. Duque, P. Lopez-Dekker, and J. J. Mallorqui, "Single-pass bistatic SAR interferometry using fixed-receiver configurations: theory and experimental validation," *IEEE Transactions on Geoscience and Remote Sensing*, vol. 48, pp. 2740–2749, June 2010.

[109] "ESA's radar observatory mission for GMES operational services," *ESA Special Publication*, no. 1322/1, 2012.

[110] V. Kubica and X. Neyt, "ScanSAR resolution enhancement in bistatic operation," in *IET International Radar Conference*, (Glasgow, UK), Oct. 2012.

[111] X. Neyt, P. Pettiaux, M. De Smet, and M. Acheroy, "Scatterometer Algorithm Review: Test Plan," tech. rep., Royal Military Academy, 2003.

[112] P. Petrov Yuri and V. S. Sizikov, *Well-posed, Ill-posed, and Intermediate Problems with Applications*. De Gruyter, 2005.

[113] A. K. Katsaggelos, *Digital Image Restoration*. Springer Series in Information Sciences, 1991.

[114] M. Zink, "Update on antenna elevation pattern estimation from rain forest data," in *Proceedings of the ENVISAT Validation Workshop (ESA SP-531)*, (Italy), Dec. 2002.

[115] H. Van Trees, *Detection, Estimation and Modulation theory — Part I*. Wiley, 1968.

[116] S. P. Luttrell, "Prior knowledge and object reconstruction using the Best Linear Estimate technique," *Optica Acta*, vol. 32, no. 6, pp. 703–716, 1985.

[117] R. Raney, A. Luscombe, E. Langham, and S. Ahmed, "RADARSAT," *Proceedings of the IEEE*, vol. 79, pp. 839–849, June 1991.

[118] V. Kubica, X. Neyt, and H. D. Griffiths, "Improved cross-range resolution in TOPSAR imaging using Sentinel-1A in bistatic operation," in *IEEE International Radar Conference*, (Arlington, VA), May 2015.

[119] R. Touzi, A. Lopes, J. Bruniquel, and P. Vachon, "Coherence estimation for SAR imagery," *IEEE Trans. on Geoscience and Remote Sensing*, vol. 37, no. 1, pp. 135–149, 1999.

[120] S. G. Mallat and Z. Zhang, "Matching pursuits with time-frequency dictionaries," *IEEE Transactions on Signal Processing*, vol. 41, no. 12, pp. 3397–3415, 1993.

[121] E. J. Candès and M. B. Wakin, "An introduction to compressive sampling," *IEEE Signal Processing Magazine*, vol. 25, pp. 21–30, Mar. 2008.

[122] E. J. Candes and T. Tao, "Near-optimal signal recovery from random projections: Universal encoding strategies?," *IEEE Transactions on Information Theory*, vol. 52, no. 12, pp. 5406–5425, 2006.

[123] E. J. Candès, J. Romberg, and T. Tao, "Robust uncertainty principles: exact signal reconstruction from highly incomplete frequency information," *IEEE Transactions on Information Theory*, vol. 52, no. 2, pp. 489–509, 2006.

[124] E. J. Candès, J. Romberg, and T. Tao, "Stable signal recovery from incomplete and inaccurate measurements," *Communications on Pure and Applied Mathematics*, vol. 59, no. 8, pp. 1207–1223, 2006.

[125] S. S. Chen, D. L. Donoho, and M. A. Saunders, "Atomic decomposition by basis pursuit," *Siam Journal on Scientific Computing*, vol. 20, no. 1, 1998.

[126] E. J. Candès and T. Tao, "Decoding by linear programming," *IEEE Transactions on Information Theory*, vol. 51, no. 12, pp. 4203–4215, 2005.

[127] J. A. Tropp, "Greed is good: Algorithmic results for sparse approximation," *IEEE Transactions on Information Theory*, vol. 50, no. 10, pp. 2231–2242, 2004.

[128] U. Benz, K. Strodl, and A. Moreira, "A comparison of several algorithms for SAR raw data compression,," *IEEE Transactions on Geoscience and Remote Sensing*, vol. 33, no. 5, pp. 1266–1276, 1995.

[129] E. J. Candès and J. Romberg, "Sparsity and incoherence in compressive sampling," *Inverse Problems*, vol. 23, no. 3, pp. 969–985, 2007.

[130] Y. C. Pati, R. Rezaiifar, and P. S. Krishnaprasad, "Orthogonal matching pursuit: recursive function approximation with applications to wavelet decomposition," in *Asilomar Conference on Signals, Systems & Computers*, vol. 1, pp. 40–44, 1993.

[131] B. L. Sturm and M. G. Christensen, "Comparison of orthogonal matching pursuit implementations," in *Proceedings of 20th European Signal Processing Conference*, (Bucharest, Romania), Aug. 2012.

[132] R. Davies, L. Mihaylova, N. Pavlidis, and I. Eckley, "The effect of recovery algorithms on compressive sensing background subtraction," in *Workshop on Sensor Data Fusion: Trends, Solutions, Applications (SDF)*, 2013.

[133] H. Yan, J. Xu, and X. Zhang, "Compressed sensing radar imaging of off-grid sparse targets," in *IEEE International Radar Conference*, pp. 690–693, 2015.

[134] S. Dutta and A. De, "Sparse ultra wideband radar imaging in a locally adapting matching pursuit (LAMP) framework," in *IEEE International Radar Conference*, (Arlington, VA), 2015.

[135] G. Tang, B. N. Bhaskar, P. Shah, and B. Recht, "Compressed sensing off the grid," *IEEE Transactions on Information Theory*, vol. 59, pp. 7465–7490, Nov. 2013.

[136] Y. Chi, L. L. Scharf, A. Pezeshki, and A. R. Calderbank, "Sensitivity to basis mismatch in compressed sensing," *IEEE Transactions on Signal Processing*, vol. 59, pp. 2182–2195, May 2011.

[137] F. Römer, R. Alieiev, M. Ibrahim, G. Del Galdo, and R. S. Thomä, "An analytical study of sparse recovery algorithms in presence of an off-grid source," in *2nd*

Intl. Workshop on Compr. Sensing applied to Radar, (Bonn, Germany), Sept. 2013.

[138] L. Prünte, "GMTI from multichannel SAR images using compressed sensing under off-grid conditions," in *Proceedings of the14th International Radar Symposium*, vol. 1, pp. 95–100, 2013.

[139] M. Baczyk, K. Kulpa, and M. Samczynski, P. Malanowski, "The impact of reference channel SNR on targets detection by passive radars using DVB-T signals," in *IEEE International Radar Conference*, (Arlington, VA), pp. 708–712, May 2015.

[140] C. Thain, R. Barstow, and T. Wong, "Sentinel-1 Product Specification," tech. rep., MDA, 2011.

[141] "Sentinels High Level Operations Plan," tech. rep., European Space Agency, 2015.

[142] A. Meta, P. Prats, U. Steinbrecher, J. Mittermayer, and R. Scheiber, "First TOPSAR image and interferometry results with TerraSAR-X," in *Fringe Workshop*, (ESRIN, Frascati, Italy), 2007.

[143] S. Duque, P. Lopez-Dekker, J. J. Mallorqui, and J. C. Merlano, "Back and Forward Bistatic Interferometry," in *Proceedings of the IEEE International Geoscience and Remote Sensing Symposium*, (Boston, MA), pp. III–601 – III–604, 2008.

[144] S. Duque, P. Lopez-Dekker, J. C. Merlano, and J. J. Mallorqui, "Bistatic SAR along track interferometry with multiple fixed receivers," in *Proceedings of the IEEE International Geoscience and Remote Sensing Symposium*, (Honolulu, Hawaii), pp. 4099–4102, July 2010.

[145] P. Lopez-Dekker, S. Duque, J. C. Merlano, J. C. Rodriguez-Silva, and J. J. Mallorqui, "Fixed-receiver bistatic SAR along-track interferometry: first results," in *Proceedings of the 8th European Conference on Synthetic Aperture Radar*, (Aachen, Germany), pp. 1–4, June 2010.

[146] R. Bamler, D. Geudtner, B. Schattler, P. Vachon, U. Steinbrecher, J. Holzner, J. Mittermayer, H. Breit, and A. Moreira, "RADARSAT ScanSAR interferometry," in *Proceedings of the IEEE International Geoscience and Remote Sensing Symposium*, vol. 3, pp. 1517–1521, IEEE, 1999.

[147] V. Kubica and X. Neyt, "Feasibility of resolution-enhanced burst-mode interferometry in bistatic SAR," in *Proceedings of IEEE Conference on Radar*, (Adelaide, South Australia), Sept. 2013.

[148] D. M. Pozar and D. Schaubert, *Microstrip Antennas: The Analysis and Design of Microstrip Antennas and Arrays*. Wiley, 1995.